Department of Biomedical Sciences
University of Sassari

PhD Course in Life Science and Biotechnologies

Coordinator: Prof. ssa Daria Sanna

XXXIX Cycle

Targeting Oxidative Stress and Glycolytic Dysfunction: Nicotinamide Mononucleotide as a Promising Strategy to Prevent Ionizing Radiation Induced Ovarian Failure

A Thesis Submitted for the Degree of Doctor of Philosophy

Supervisor

Prof. Giampiero Capobianco

Co-supervisor

Prof. ssa Marilena Formato

Prof. Antonio Cigliano

Doctoral Thesis

Dr. Qian Wang

Academic Year 2025/2026

Abstract

Objective

With advances in cancer diagnosis and therapy, survival rates of female patients have markedly improved. However, radiotherapy, a cornerstone in the treatment of colorectal and cervical cancers, poses a high risk of ovarian damage since the ovary is extremely sensitive to ionizing radiation (IR). Even low doses of IR may lead to infertility and endocrine dysfunction, even induce premature ovarian insufficiency (POI). Current protective strategies, such as ovarian transposition, gamete/ovarian tissue cryopreservation, hormone replacement therapy, or GnRH-a injections, are limited by technical, ethical, or clinical feasibility issues. Nicotinamide mononucleotide (NMN), a direct precursor of NAD^+ , has been validated to alleviate oxidative stress, restore energy metabolism, and protect ovarian function with high safety. In this study we aimed to systematically evaluate the protective role and mechanisms of NMN against IR induced ovarian dysfunction.

Methods and Results

This research integrated **in vivo mouse experiments, ovarian transcriptomics, and in vitro granulosa cell validation** to dissect the protective mechanisms of NMN.

Animal studies:

C57BL/6J female mice were subjected to 5Gy Cs-137 γ-irradiation to induce ovarian insufficiency. IR led to reduced ovarian size, follicular atresia, AMH↓/FSH↑, disrupted estrous cycles, NAD^+ depletion, increased oxidative stress (SOD↓, MDA↑), impaired glycolysis (HK2, PKM2, LDHA↓), and apoptosis activation (BAX, Cleaved-Casp3↑). Oral NMN (500 mg/kg/day) significantly reversed these phenotypes, restoring ovarian morphology, hormone levels, and metabolic balance, with no adverse effects in healthy mice.

Transcriptomic analysis:

RNA-seq revealed extensive DEGs in IR-exposed ovaries: upregulated genes enriched in DNA damage response, oxidative stress, and apoptosis pathways; downregulated

genes involved in glycolysis, energy metabolism, and ovarian maintenance. NMN supplementation exerted a bidirectional correction effect, suppressing stress/apoptosis-related genes while restoring glycolysis and mitochondrial energy genes. KEGG enrichment highlighted overlapping pathways (oxidative stress, glycolysis, apoptosis, PI3K/AKT/HIF-1α), confirming the role of NMN in metabolic reprogramming and ovarian protection.

Cellular validation:

An H_2O_2 induced oxidative stress model in KGN cells reproduced IR-associated phenotypes (NAD^+ depletion, ROS↑, Δψm loss, glycolysis inhibition, AMH/E2↓). NMN pretreatment improved antioxidant enzyme activity (SOD, CAT, T-GSH/GSSG), restored glycolytic flux (HK2, PKM2, LDHA, lactate/pyruvate), stabilized mitochondrial function, and enhanced hormone secretion. Inhibitors LY294002 and MK2206 abrogated NMN's effects, verifying that **PI3K/AKT/HIF-1α signaling is essential for NMN mediated ovarian protection**.

Conclusion

The study indicated that NMN effectively mitigates IR induced ovarian insufficiency by restoring NAD^+, reprogramming glycolysis, reducing oxidative stress, stabilizing mitochondrial function, and modulating the PI3K/AKT/HIF-1α axis. These findings highlight NMN is a safe and promising strategy for protecting female cancer patients' ovarian function undergoing radiotherapy.

Keywords: Ionizing radiation; Premature ovarian insufficiency; NMN; NAD^+; Oxidative stress; Glycolysis; PI3K/AKT/HIF-1α

Index

Chapter Ⅰ. Introduction

1. Ovarian Dysfunction Induced by Radiotherapy

Radiotherapy is a cornerstone in the management of malignancies, and remains one of the most effective treatment modalities for cancers with high incidence in women of reproductive age, such as cervical, breast, and rectal cancer. Recent global cancer statistics indicate that breast cancer continues to represent the predominant malignant disease affecting women across the world. Although its incidence has shown a slow but steady increase over the past decade, early screening has improved survival, particularly among women of childbearing age[1]. Colorectal cancer ranks second among women globally. While it primarily occurs in the elderly, a rising incidence has been observed in younger women in recent years, with approximately 10–15% of cases diagnosed in patients under 50 years old[2]. Cervical cancer is the fourth malignancy in women, with nearly 600,000 new cases annually, of which about 45% in women under 45 years old[3]. For cervical cancer, radiotherapy is generally combined with chemotherapy as either definitive treatment or postoperative adjuvant therapy[4]. The neoadjuvant chemoradiotherapy has become the standard treatment in rectal cancer[5]. In breast cancer, adjuvant radiotherapy after breast-conserving surgery significantly reduces local recurrence, and several follow-up studies have suggested that younger women derive greater benefit compared with older patients[6], [7].

Despite its wide application in female malignancies, radiotherapy exerts its antitumor effects by directly inducing DNA double-strand breaks (DSBs), protein oxidation, and lipid peroxidation, or indirectly through the radiolysis of water molecules that generate free radicals, leading to irreversible cellular damage[8]. While this mechanism is effective for tumor eradication, collateral damage to adjacent normal tissues is unavoidable[9]. In pelvic malignancies such as cervical and rectal cancer, pelvic radiotherapy is commonly employed. The ovaries, located within or near the

radiation field, are among the most radiosensitive organs. Even low radiation doses can induce ovarian injury[10]. As little as 0.2–0.4Gy may cause follicular depletion, reducing fertility, while exposure of 2.5–6.0Gy can result in permanent sterility and radiation-induced amenorrhea[11].

The radiation-induced ovarian injury mechanisms are multifaceted:

(1) **Direct DNA damage:** Radiotherapy can induce DSBs in oocytes. When DNA repair fails, apoptosis ensues. Reiser et al. (2022) demonstrated that even 1Gy significantly affected the number of primordial follicles in a murine model[12].

(2) **Oxidative stress:** The irradiation cause oxidative damage to both oocytes and granulosa cells[13].

(3) **Follicular pool depletion:** Radiotherapy accelerates the consumption of primordial follicles, leading to diminished ovarian reserve. Clinical evidence suggests that 2Gy is associated with a 1–5% risk of ovarian failure, whereas ≥24Gy confers ≥50% risk[14].

(4) **Vascular injury:** Radiotherapy damages ovarian vasculature, resulting in ischemia and fibrosis[10].

(5) **Inflammatory response:** Irradiation activates the inflammasome of NLRP3, promoting of inflammatory cytokines (IL-1β, IL-18), which further compromise ovarian function[15].

Ovarian reserve after radiotherapy can be assessed by several biomarkers, with anti-Müllerian hormone (AMH) and antral follicle count (AFC) being the widely used[16]. AMH, secreted by granulosa cells of growing follicles, is strongly correlated with the primordial follicle pool and is considered a reliable marker of ovarian reserve[17]. A meta-analysis of 92 studies involving 9,183 patients demonstrated a significant decline in AMH following radiotherapy, with reductions ranging from 42% to levels below the detection limit, and most studies reporting mean or median decreases ≥90%[18]. AFC, determined by transvaginal ultrasound of follicles 2–9 mm in diameter, is another important predictor of ovarian reserve[19].

Gracia et al. (2012) found a significant association between pelvic radiotherapy and reduced AFC[20].

The clinical consequences of radiation-induced ovarian dysfunction are manifold:
(1) **POI:** Radiotherapy is one of the main iatrogenic causes of POI, characterized by amenorrhea, induced FSH (FSH >25 IU/L), and decreased estradiol levels[21].
(2) **Infertility:** Loss of both oocyte quality and quantity compromises fertility[22].
(3) **Long-term health sequelae:** POI has been linked to cardiovascular disease, osteoporosis, cognitive decline, and mood disorders[23].

Several strategies have been developed to mitigate ovarian damage:
(1) **Ovarian transposition (OT):** Surgically relocating the ovaries outside the radiation field prior to treatment can preserve ovarian function, with reported success rates ranging from 33% to 100%. However, OT carries risks of ovarian cysts, pelvic pain, and exposure to scattered radiation[24]. Furthermore, surgical manipulation may damage ovarian vasculature, resulting in reduced blood supply and impaired function post-transposition[25].
(2) **Oocyte or embryo cryopreservation:** Mature oocyte and embryo freezing are the main fertility preservation techniques nowadays. However, they require controlled ovarian stimulation and may delay cancer therapy. In addition, in many regions, embryo cryopreservation is legally restricted to married couples[26], [27].
(3) **Ovarian tissue cryopreservation:** This method involves harvesting, freezing, and later autotransplanting ovarian tissue. While technically complex and associated with the risk of malignant cell reimplantation, it has led to restoration of endocrine function and even live births in multiple reported cases[28], [29].
(4) **Hormone replacement therapy (HRT):** HRT alleviates hypoestrogenic symptoms but cannot restore ovarian function or fertility. It improves vasomotor symptoms with efficacy rates of 70–90%, ameliorates urogenital atrophy[30], and reduces the risk of osteoporosis[31]. The ‘timing hypothesis’ posits that starting treatment in women younger no more than 60 years old, and within 10 years

following menopause, may yield favorable cardiovascular outcomes[32]. However, HRT carries risks, including increased breast cancer incidence after > 5 years of combined estrogen-progestin therapy[33] and elevated venous thromboembolism risk with oral preparations, which can be mitigated with transdermal formulations[34]. Individualized regimens and the principle of 'the lowest effective dose' are essential[35].

(5) **Gonadotropin-releasing hormone agonists (GnRH-a):** By suppressing FSH and LH secretion, GnRH-a induces temporary ovarian suppression and may reduce gonadotoxic damage. Meta-analyses have confirmed its efficacy in reducing premature ovarian insufficiency after cancer therapy[36]. Studies in breast cancer, lymphoma, and gynecologic malignancies support its protective role in preserving ovarian function and improving reproductive results[37], [38]. However, prolonged administration may result in hypoestrogenic adverse effects, such as bone demineralization and vasomotor disturbances[39]. Moreover, the protective efficacy of GnRH-a is not consistent across tumor types, and its benefit for fertility outcomes remains debated[40].

In summary, while radiotherapy plays an important role in the treatment of malignancies in women of reproductive age, it inevitably compromises ovarian reserve and fertility potential. Consequently, many young survivors face endocrine insufficiency and infertility after achieving remission[18], [41]. Thus, developing novel therapeutic strategies, including natural agents or interventions that modulate endogenous protective mechanisms, represents a critical unmet clinical need.

2. Mechanisms of Ionizing Radiation-Induced Injury in Ovarian Granulosa Cells

Granulosa cells (GCs) play a pivotal role in the female reproductive system, contributing to ovarian development, providing support for oocytes, and regulating hormone secretion.

2.1. The Role of Ovarian GCs in Oocyte Development

Follicles are the fundamental structural and functional units of the ovary, consisting of an oocyte surrounded by GCs. The development of oocytes does not occur in isolation but relies on the close support and regulation of granulosa cells[42], [43]. Through hormone secretion, provision of metabolic substrates, and bidirectional signaling, granulosa cells create the essential conditions for oocyte growth, maturation, and functional competence.

2.1.1. GCs in the Synthesis and Secretion of Sex Steroids

Estrogen synthesis: Granulosa cells convert androgens derived from theca cells into estrogens (e.g., estradiol) via aromatase, thereby promoting oocyte development and modulating the follicular microenvironment[44], [45].

Progesterone synthesis: Following ovulation, granulosa cells undergo luteinization and differentiate into luteal cells, producing progesterone to support fertilization and early embryonic development after oocyte release.

2.1.2. Nutritional and Metabolic Support from GCs to Oocytes

Oocytes have limited intrinsic metabolic capacity, particularly in glucose utilization, and thus depend on granulosa cells for nutrients. Glucose in granulosa cells is metabolized through glycolysis to produce pyruvate and lactate, which are subsequently shuttled to the oocyte via gap junctions. These metabolites fuel the tricarboxylic acid (TCA) cycle, sustain meiotic progression, nuclear and cytoplasmic maturation, and maintain fertilization potential[46], [47].

2.1.3. Signaling Interactions Between GCs and Oocytes

Cellular junctions: Granulosa cells and oocytes are connected by gap junctions and transzonal projections, enabling the transfer of small molecules and signals, which ensures synchronized oocyte development.

Cytokines and paracrine factors: Granulosa cells secrete multiple cytokines and growth factors (e.g., GDF9, BMP15) that regulate oocyte growth rate and developmental competence[48], [49].

2.1.4. GCs in Oocyte Quality and Female Fertility

Granulosa cell function is tightly correlated with oocyte quality. By maintaining nutrient supply and stabilizing the microenvironment, by regulating the oocyte microenvironment, granulosa cells directly shape its competence for fertilization and early development of embryos[50], [51]. Thus, the health and function of granulosa cells are critical determinants of female fertility.

2.1.5. GCs Responses to Damage and Pathological Conditions

Stress and injury responses: Under conditions such as radiation, chemotherapy, or environmental stress, granulosa cells may undergo oxidative stress, DNA damage, or apoptosis, depriving oocytes of essential support and impairing their developmental potential[52].

Disease-associated alterations: Granulosa cell dysfunction is closely linked to polycystic ovary syndrome (PCOS), diminished ovarian reserve, and certain ovarian tumors[42], [53]. Investigating granulosa cell alterations in these contexts not only enhances understanding of normal ovarian physiology but also provides insights into early diagnosis and therapeutic strategies.

In summary: granulosa cells play indispensable supportive roles in oocyte development, and their health and functional status directly determine oocyte quality and female reproductive capacity.

2.2. Ionizing Radiation-Induced Damage to Ovarian GCs

GCs are the key effector cells within the ovarian follicular microenvironment. They participate in follicular recruitment and selection, steroidogenesis, and provide nutritional and paracrine support to oocytes. The structural and functional integrity of

GCs directly determines ovarian reserve and endocrine homeostasis[54]. Clinically, AMH, secreted primarily by growing follicles in GCs, is widely used as a sensitive biomarker of gonadotoxicity induced by radiotherapy and chemotherapy, highlighting GC injury as a central mediator of radiation-related ovarian dysfunction[55].

Under physiological conditions, oocytes and GCs maintain bidirectional communication through gap junctions. Connexin-43 (Cx43), encoded by GJA1 and highly expressed in GCs, represents an indispensable molecular hub for folliculogenesis[56]. Cx43-mediated transzonal projections enable the transfer of metabolic substrates, second messengers, and small RNAs, and are finely regulated by gonadotropins and oocyte-derived factors. Impairment of Cx43 expression or function leads to follicular arrest, atresia, and decline in oocyte quality, resulting in endocrine disruption[48].

Ionizing radiation induces GC apoptosis, accelerates follicular atresia, and causes ovarian failure, leading to infertility, sex hormone disorders, and long-term health problems such as osteoporosis and cardiovascular disease[57]. Clinical studies have reported that after pelvic radiotherapy, up to 90% of adult women and nearly all prepubertal girls experience a precipitous decline in ovarian reserve[58]. Although fertility preservation treatments such as oocyte cryopreservation and ovarian tissue transplantation have achieved some progress, limitations remain, including surgical risks, low success rates, and inability to fully prevent radiation-induced damage. Thus, elucidating the molecular mechanisms of GC injury by radiation and developing protective strategies are of great importance for improving reproductive health in female cancer patients.

Current evidence indicates that ionizing radiation induces GC injury primarily by directly causing DNA double-strand breaks (DSBs) and indirectly accumulating reactive oxygen species (ROS). These activate the ATM/ATR–p53 DNA damage response (DDR) pathway, resulting in cell-cycle arrest (G1/S and G2/M),

mitochondrial apoptosis (BAX/BCL-2 imbalance, caspase-3 activation), and cellular senescence[59], [60]. ROS mediated oxidative stress amplifies p53 signaling and disrupts lipid membranes and mitochondrial function, forming a 'damage–response–apoptosis' positive feedback loop. The in vivo and in vitro studies tell us that actively dividing GCs undergo marked cell death and gap junction disruption within hours after irradiation, triggering premature follicular atresia[61]. Similar DSB phenotypes have been observed in chemotherapy models, suggesting that DNA damage is a convergent mechanism across different insults.

At the organ level, GC loss accelerates global follicular apoptosis and depletion, suppresses AMH and estradiol synthesis, and results in luteal insufficiency and menstrual irregularities, thereby increasing the risk of POI and infertility[62], [63]. The ovarian radisoensitivity is both age- and dose-dependent. Predictive models and population studies have demonstrated that ovarian reserve decline and earlier menopause can be quantitatively estimated following abdomino pelvic or total body irradiation[11], [64]. Furthermore, experimental and clinical evidence suggests that follicular loss can occur even in the absence of overt stromal fibrosis, highlighting follicles, particularly the GC oocyte complex as the primary targets of radiation[65].

Therefore, along the causal chain of 'radiation → GC damage → follicular dysfunction,' urgent priorities include: (1) defining the spatiotemporal dynamics of DSB sensing/repair (ATM/ATR–CHK–p53 axis), oxidative stress–mitochondrial signaling, and GC metabolic pathways (e.g., PI3K/AKT); (2) elucidating structural–functional uncoupling of Cx43-mediated gap junctions under irradiation; (3) identifying vulnerable nodes and reversibility of GC steroidogenesis and AMH production/secretion; (4) linking these alterations to ovarian reserve phenotypes

(AMH levels, antral follicle counts) and clinical outcomes (POI, infertility)[66], [67]. These insights will provide mechanistic targets and evaluation frameworks for radioprotective and fertility preservation strategies (e.g., dose optimization, ovarian transposition, pharmacological ovarian protection, biomaterial shielding). Moreover, systematic comparisons of GC injury patterns across different radiation doses and fractionation schemes remain lacking and warrant further investigation.

3. The Role of NMN in Healthy and Diseased Populations

NMN is a key precursor of NAD^+ . NAD^+ is an essential coenzyme, primarily localized in mitochondria, that plays central roles in energy metabolism, DNA repair, cellular signaling, and epigenetic regulation[68]. As a critical intermediate in the NAD^+ salvage pathway, NMN can be efficiently converted within cells[69].

NMN is widely available in dietary sources such as grains, meat and vegetables, and exhibits a high safety profile[70]. In recent years, microbial engineering approaches employing bacteria and yeast have enabled efficient and stable NMN production, thereby improving its feasibility for broader application[71], [72].

Recent studies increasingly highlight the pharmacological benefits of NMN in cardiovascular, metabolic, and neurodegenerative pathologies[73]. The primary mechanism is through enhancing NAD^+ biosynthesis, thereby reversing a spectrum of pathological processes associated with NAD^+ deficiency, including mitochondrial dysfunction, excessive ROS generation, impaired DNA repair, and reduced cellular viability[74], [75]. In addition, NMN regulates metabolic pathways, with reported effects on insulin resistance[76], [77] and glycolysis[78], [79], [80], [81].

With advancing age and progression of chronic diseases, systemic NAD^+ levels decline, which is closely associated with mitochondrial dysfunction, metabolic imbalance, and aberrant inflammatory responses[82]. Evidence from recent randomized controlled trials indicates that oral NMN supplementation is safe and effectively enhances systemic NAD^+ metabolite levels in a dose-dependent manner. [83]. Moreover, preliminary findings suggest improvements in muscle insulin sensitivity[77], physical performance, and vascular elasticity; however, robust evidence on major clinical endpoints remains limited.

Importantly, ovarian NAD^+ levels also decline markedly with aging or reduced ovarian reserve[84]. Proteomic analyses further suggest that ovarian tissue may preferentially utilize NMN compared with other NAD^+ precursors[85]. Therefore, NMN is considered one of the most promising, safe, and convenient nutritional supplements to counteract NAD^+ decline associated with aging and disease.

3.1. Physiological Effects of NAD^+

NAD^+ functions as both a central redox coenzyme and an essential substrate for a wide array of NAD^+ consuming enzymes, including poly (ADP-ribose) polymerases (PARPs), sirtuins, and NADases such as CD38. Through these actions, NAD^+ regulates tricarboxylic acid (TCA) cycle activity, fatty acid oxidation, epigenetic programs, DNA repair, and immune signaling, thereby exerting multilayered control over human physiology[86], [87].

3.1.1. Cell Metabolism and Redox Homeostasis

NAD^+ /NADH couples regulate flux through glycolysis (e.g., GAPDH), the TCA cycle (e.g., malate dehydrogenase), β-oxidation of fatty acids, and the mitochondrial electron transport chain, thereby shaping both metabolic throughput and redox balance. Intracellular NAD^+ pools are compartmentalized across the nucleus, cytoplasm, and mitochondria, where local NAD^+ concentrations are comparable to the Km values of NAD^+ -dependent enzymes, thus directly influencing sirtuin and PARP activity [88]. Mitochondrial NAD^+ uptake depends on the carrier SLC25A51, which ensures efficient oxidative phosphorylation and dehydrogenase reactions[89].

3.1.2. NAD^+ as a Signaling Substrate for Consumer Enzymes

3.1.2.1. Sirtuins（SIRT1-7）

Sirtuins utilize NAD^+ as a cosubstrate to catalyze deacylation and deamidation reactions, thereby remodeling chromatin and metabolic programs. These activities promote mitochondrial biogenesis, stress resistance, inflammation control, and circadian rhythm regulation[90]. Circadian oscillations of NAD^+ are tightly coupled

with the SIRT1/CLOCK–BMAL1 axis, forming a 'metabolism–clock' synchronizer[91].

3.1.2.2. PARPs (Exemplified by PARP1)

Upon DNA damage, PARP1 activation rapidly consumes NAD^+ to synthesize poly (ADP-ribose), which recruits repair proteins and remodels chromatin[92]. Declines in NAD^+ availability reprogram cellular metabolic dependencies, thereby influencing DNA repair capacity and survival[93].

3.1.2.3. CD38/CD157 and Calcium Signaling

CD38 hydrolyzes NAD^+ to produce ADPR and cADPR, and can also generate NAADP from $NADP^+$, regulating Ca^{2+} release from the endoplasmic reticulum and endo-lysosomal stores[94], [95]. As increase with age, major driver of systemic NAD^+ decline and mitochondrial dysfunction, the CD38 expression increases[96].

3.1.2.4. SARM1 and Axonal Degeneration

In neurons, sterile α and TIR motif-containing protein 1 (SARM1) functions as a potent NADase. Upon injury or stress, SARM1 triggers rapid NAD^+ depletion, leading to axonal degeneration while intersecting with innate immune signaling[97].

3.1.3. NAD^+ Synthesis, Turnover, and Compartmentalization

NAD^+ homeostasis is maintained through three primary pathways:

De novo pathway: tryptophan catabolism via the kynurenine pathway.

Preiss–Handler pathway: nicotinic acid (NA) conversion via NAPRT.

Salvage pathway: recycling of nicotinamide (NAM) to NMN by the rate-limiting enzyme NAMPT, followed by NMNAT-mediated NAD^+ synthesis.

Additionally, NRKs (NRK1/2) mediate utilization of nicotinamide riboside (NR) and NMN, providing key nodes for boosting NAD^+ upon precursor supplementation [98]. Mitochondrial NAD^+ is imported via SLC25A51, while nuclear/cytoplasmic and mitochondrial pools are subject to relatively independent regulation[99].

Conversely, sirtuins, PARPs, CD38, and SARM1, collectively determines turnover rates[100]. Inhibition of CD38 or supplementation with NAD^+ precursors has been shown in animal models and early clinical studies to elevate tissue NAD^+ levels, restore mitochondrial function, and ameliorate select metabolic and inflammatory phenotypes[101].

3.2. Metabolic Biology of NAD^+ and NMN

In mammals, NAM is primarily converted into NMN through the NAMPT pathway, which is then transformed into NAD^+ via the NMNAT enzyme. Additionally, NMN can be indirectly synthesized when nicotinamide ribosyl (NR) is phosphorylated by nicotinamide reductase (NRK). With age and chronic inflammation, the imbalance between NAD^+ synthesis and consumption lead to decreased tissue NAD^+ levels, a condition recognized as a common metabolic hallmark of multi-organ aging.

After oral administration, NMN is converted into NR by exoenzymes such as CD73 dephosphorylation in the intestinal lumen, then transported into cells via SLC29A family nucleoside transporters[102]. Some studies suggest that SLC12A8 in the small intestinal epithelium may directly transport NMN, though this remains controversial [103]. Tracer studies indicate that oral precursors are often first converted into NAM in multiple tissues before entering the salvage pathway. These differing mechanisms may explain the varying magnitudes and temporal patterns of NAD^+ elevation observed across different tissues[104].

3.3. Physiological Effects of NMN in Healthy People

NMN represents a central metabolite in NAD^+ production, primarily formed via NAMPT-mediated catalysis[105]. Given the pivotal roles of in cellular energy metabolism, DNA repair, epigenetic regulation, and immune homeostasis, NMN has emerged as a direct precursor for enhancing NAD^+ levels[106]. This makes it a hot research topic in healthy populations, focusing on metabolic stabilization and anti-aging interventions.

3.3.1. Improvement of NAD^+ Level and Energy Metabolism

Multiple randomized, double-blind, placebo-controlled clinical trials have confirmed that daily oral NMN administration (250-900 mg) over 6-12 weeks markedly elevates peripheral NAD^+ and associated metabolite levels while maintaining a favorable safety profile. A 2023 multicenter randomized controlled dose-escalation study of 80 individuals demonstrated a progressive, dose-dependent increase in NAD^+ levels over 60 days, suggesting favorable trends in physical performance and metabolic outcomes[107]. A 2024 RCT in older adults (n=60) showed that 12-week NMN supplementation (250 mg/day) elevated NAD^+, preserved mobility, and improved sleep quality[108]. Oral NMN is rapidly absorbed and converted into NAD^+ in blood and tissues, thereby increasing systemic NAD^+ stores[70]. In healthy subjects, single-dose or short-term ($\leq$ 12 weeks) NMN intake significantly elevated peripheral NAD^+ levels while improving indicators related to glucose-lipid metabolism and insulin sensitivity[109], [110].

3.3.2. Improvement of Motor Performance and Skeletal Muscle Function

NMN enhances skeletal muscle NAD^+ levels, improves mitochondrial oxidative phosphorylation capacity, and increases capillary density. A randomized controlled trial demonstrated that healthy middle-aged and elderly individuals who took NMN orally for six consecutive weeks showed improved aerobic metabolic efficiency and endurance performance in skeletal muscles, suggesting its potential value in delaying physical decline and promoting healthy aging , a 12-week daily dose of 250 mg NMN significantly increased total blood NAD^+ levels and led to nominal improvements in indicators such as walking speed and grip strength (requiring large-scale validation) [111].

3.3.3. Cardiovascular and Metabolic Homeostasis

NMN enhances vascular endothelial function and insulin sensitivity by activating the SIRT1/PGC-1 α pathway. Small-scale clinical trials in healthy and sub-healthy

populations have demonstrated that NMN supplementation correlates with improved arterial compliance and reduced inflammatory markers, suggesting potential interventions for primary cardiovascular disease prevention[112]. Additionally, a 12-week randomized controlled trial (RCT) administered at 250 mg/day showed a downward trend in arterial pulse wave velocity (baPWV), indicating possible vascular benefits, though the inter-group differences were not statistically significant[113].

3.3.4. Safety and Tolerance of NMN

Preclinical studies have demonstrated favorable safety profile of NMN. Multiple human trials have confirmed that both single high-dose administration (500-900 mg) and long-term supplementation (12 weeks at 250-600 mg daily) have shown no serious adverse events, with mild gastrointestinal discomfort being the primary side effect[83], [112], [114]. These findings provide preliminary safety evidence for its widespread application in healthy populations.

3.4. Effects of NMN on Disease Populations

The most well-established effect of NMN is its ability to elevate NAD^+ levels and related metabolites in vivo. The improvement of functional or disease outcomes is mostly signaling level changes, which are affected by population, dose, time course and endpoint evaluation. Many basic research results still need to be verified by phase III clinical trials or more powerful research results.

3.4.1. Diabetes and Insulin Resistance

The prediabetes and type 2 diabetes patients, NAD^+ levels are generally reduced. A randomized controlled trial found that NMN significantly improved skeletal muscle insulin-mediated glucose clearance and enhanced AKT/mTOR pathway phosphorylation, thereby improving the insulin sensitivity of skeletal muscle. Notably, it showed no significant side effects on weight or blood glucose control, suggesting its potential application value in metabolic diseases[77].

3.4.2. Cardiovascular Diseases

Patients with cardiovascular diseases commonly exhibit mitochondrial dysfunction and endothelial dysfunction. In vivo studies suggest that NMN promotes endothelium-dependent vasodilation and protects against myocardial ischemia, reperfusion injury by stimulating the SIRT1/PGC-1α axis[115].

3.4.3. Neurodegenerative Diseases

Patients with Alzheimer and Parkinson exhibit NAD^+ depletion and neuronal energy metabolism disorders. Preclinical studies indicate that NMN can delay cognitive decline by enhancing NAD^+ levels, improving mitochondrial function, and inhibiting neuroinflammation and apoptosis[116]. Although clinical data from humans remains limited, preliminary observations suggest NMN holds potential in delaying cognitive deterioration.

3.4.4. Age-Related Diseases

Aging-related disorders (such as sarcopenia and frailty syndrome) are closely associated with decreased NAD^+ levels. Clinical trials have demonstrated that NMN can improve skeletal muscle aerobic metabolism and exercise endurance in elderly patients, suggesting its role in healthy aging and delaying frailty[117]. Systematic reviews and meta-analyses indicate that supplementation regimens containing NMN/NR show inconsistent aggregate effects on endpoints such as skeletal muscle mass, grip strength, and walking speed, indicating the need for larger sample sizes, longer follow-up periods, and standardized endpoint criteria[118].

3.4.5. Acute Illnesses and Organ Damage

An RCT of hospitalized COVID-19 patients with AKI (MIB-626, NMN patented formulation, 1 g bid for 14 days) demonstrated that peripheral blood NAD^+ levels and methylation metabolites increased significantly compared to placebo. However, renal injury biomarkers and inflammatory markers showed no significant differences, suggesting that increasing NAD^+ does not provide short-term clinical benefits in the severe hospitalized population[119].

4. Effects of NMN on Ovarian Function

With age, ovarian tissue and oocyte NAD^+ levels progressively decline, accompanied by mitochondrial dysfunction, elevated oxidative stress, chromosomal separation, spindle assembly abnormalities, and impaired endocrine and support functions of GCs. These combined changes drive the decline in ovarian function and oocyte quality. Within the framework of ovarian aging, exogenous NAD^+ precursors (represented by NMN) are believed to improve the ovarian microenvironment and fertility by restoring mitochondrial metabolism, alleviating inflammation and oxidative stress, stabilizing epigenetics, and enhancing meiotic quality control[84].

4.1. The Lab Research of the NMN's Effectiveness on Ovarian Function

4.1.1. NMN Improves Age-related Ovarian Function and Oocyte Quality Decline

In naturally aging mice, oocyte NAD(P)H signaling declines with age, accompanied by spindle and chromosome separation defects, reduced mitochondrial membrane potential, and increased ROS[120]. Systemic supplementation with NMN restores ovarian and oocyte NAD^+ levels, increases the number of ovulating oocytes, improves meiotic quality control and embryo development potential (enhanced blastocyst formation rate), partially reversing age-related infertility phenotypes. Ultrastructural observations and functional assays suggest these benefits are associated with mitochondrial function improvement and reduced inflammatory and stress signaling[121].

4.1.2. NMN Improves Ovarian Granulosa Cells and Ovarian Microenvironment

GCs play an important role in the oocyte microenvironment and possess steroid-producing capabilities. In vitro studies demonstrate that oxidative stress (H_2O_2) induced cycle arrest and apoptosis in GCs are significantly alleviated by

NMN treatment, with mechanisms involving enhanced cellular NAD^+ levels, reduced oxidative stress, and disrupted transcriptional processes[122]. In large animals, such as sheep, NMN activates the AMPK pathway to reduce oxidative stress and enhance steroid production in GCs, providing cross-species support for the pathway from improved follicular endocrine support to enhanced oocyte quality[123].

4.1.3. NMN Protection of Ovarian in Disease and Injury Models

In chemotherapy-associated ovarian dysfunction models, NMN enhances ovarian NAD^+ levels, alleviates follicular depletion and oocyte quality impairment. This mechanism is associated with inhibiting NLRP3-mediated pyroptosis, reducing inflammatory microenvironment, and addressing mitochondrial dysfunction, while also improving early embryonic development milestones[124]. NMN intervention shows restorative trends in oocyte actin network disorders, meiotic defects, and mitochondrial damage caused by environmental toxins (e.g., BDE-209) and metabolic comorbidities (Diabetes)[125]. These findings collectively indicate that NMN protects ovarian reserve and oocyte developmental potential through a multi-pathway synergy involving mitochondrial function, oxidative stress, inflammation, pyroptosis, cytoskeleton and meiotic quality control.

4.1.4. NMN Addition Improves Embryonic Culture System

In addition to intracellular supplementation, the incorporation of NMN into in vitro embryo culture systems has been demonstrated to enhance the developmental efficiency from fertilized eggs to blastocysts[126]. This suggests that NAD^+ metabolic support may become an exploitable direction for optimizing embryo culture media in Assisted Reproductive Technology (ART) protocols. However, the dosage window and safety profile of this strategy in different species and age groups of oocytes still require systematic evaluation.

4.2. Clinical Trials of NMN on Ovarian Function

To date, evidence from randomized controlled trials (RCTs) directly targeting ovarian function remains limited and is still accumulating. Two registered clinical trials are

currently underway: the first evaluates the effects of NMN on endocrine profiles, immune homeostasis, and reproductive outcomes in women with diminished ovarian reserve (DOR) (NCT05485610); the second investigates whether NMN can improve IVF/ICSI-ET pregnancy outcomes in DOR patients (NCT06426355). The primary endpoints of these studies include AMH, AFC, the number of retrieved oocytes and proportion of high-quality oocytes, embryo development and implantation outcomes, as well as safety indicators. With completion of recruitment and follow-up, these results are expected to provide direct evidence for the efficacy and population-specific positioning of NMN in infertility and ovarian insufficiency.

Although no completed RCTs with ovarian function as the primary endpoint have yet been reported, safety and pharmacodynamic data from other populations provide a feasible translational basis. In healthy subjects, short-term oral NMN supplementation (250 mg/day for 12 weeks or higher short-term doses) significantly increased circulating NAD^+ metabolites and was well tolerated[127]. In postmenopausal women with metabolic dysfunction, NMN supplementation improved skeletal muscle insulin sensitivity[128]. Based on these findings, rigorously designed RCTs in reproductive-age populations, particularly among women preparing for pregnancy or experiencing infertility, are warranted, with strengthened risk monitoring and standardized clinical endpoints.

5. Hypothesis and Objectives

With advancements in early cancer screening and the deterioration of living environments and food safety, women are increasingly developing tumors at younger ages. However, after clinical cure, patients must confront the critical challenge of maintaining reproductive endocrine functions and fertility, making this an urgent issue requiring attention. Conventional modalities for cancer management encompass surgical intervention, radiation and chemotherapy, biological immunotherapy, as well as targeted molecular and gene-based therapies. Notably, both radiation therapy and chemotherapy drugs can significantly impair female reproductive system functions. Particularly, ovarian function in women often declines markedly post-treatment, potentially leading to premature ovarian failure or permanent loss of reproductive endocrine capacity. While numerous studies have explored the prevention and treatment of chemotherapy-induced ovarian damage, there remains a lack of research

specifically addressing the impact of radiation therapy on fertility in women of childbearing age, especially regarding ovarian function. This gap highlights the need to develop preventive strategies against iatrogenic ovarian dysfunction. Pre-radiation therapy.

Research of radiation therapy on ovarian function remains limited, and this scarcity stems from fundamental differences between the two treatment approaches. Unlike chemotherapy, which employs standardized drug regimens for specific tumor types, radiation therapy requires customized treatment plans. The extent of radiation exposure, target areas, and dosage levels vary depending on tumor size, location, and the patient's overall health (including age and comorbidities). Furthermore, even with identical radiation doses, individual variations in patients can lead to inconsistent treatment outcomes. Consequently, the effects on ovarian function within treatment targets often prove difficult to quantify precisely.

In modern clinical practice, when radiotherapy is prioritized for early-stage cervical and rectal cancer patients, gynecologists typically consult patients about fertility preservation needs before initiating treatment. Patients may have options for ovarian transplantation, GnRH-a prophylactic therapy, or cryopreservation of embryos, eggs, or ovarian tissue, followed by hormone replacement therapy post-treatment to compensate for reproductive and endocrine impacts caused by ovarian dysfunction. While these methods demonstrate some efficacy, they remain suboptimal due to surgical intervention, low treatment success rates, limited long-term medication adherence, and ethical concerns. The most widely adopted approach involves suspending healthy ovaries outside the radiation target area to preserve ovarian function. However, radiation-induced scarring persists even with prolonged treatment cycles, posing significant risks to ovarian health. Our research aims to identify safe strategies or therapeutic agents that activate the body's natural protective mechanisms against radiation-induced ovarian damage, thereby enhancing fertility preservation.

We conducted targeted research on radiation-induced tissue damage mechanisms, revealing that ionizing radiation primarily causes direct DNA damage and indirect oxidative stress. Our study identified ovarian dysfunction, particularly oocyte apoptosis, follicular atresia, and disrupted energy supply to surrounding granulosa cells, which as key contributors. To address this, we aim to develop strategies or therapeutic agents that mitigate oxidative stress in radiation-damaged ovarian tissues while enhancing energy metabolism in granulosa cells. This dual approach of

regulating energy balance and mitigating oxidative stress provides a comprehensive strategy for protecting ovarian function.

NMN is a safe therapeutic agent that enhances cellular oxidative stress regulation and modulates energy metabolism. This natural substance also functions by boosting the body's natural enzyme NAD^+ , demonstrating efficacy in managing age-related organ degeneration and other age-related disorders. Given these properties, we investigated whether NMN could serve as both an early preventive measure for radiation-induced ovarian dysfunction and a potential therapeutic intervention for subsequent recovery processes.

Since ionizing radiation (including radiotherapy) damages ovarian function, and NMN improves NAD^+ content, plays an antioxidant role, improves metabolism, and adjusts mitochondrial function, we set the hypothesis of this study as follows:

(1) IR will damage ovarian function, especially ovarian granulosa cell function, resulting in ovarian hypofunction and even loss of reproductive and endocrine function.

(2) IR damage to ovarian function mainly affects the glucose metabolism and mitochondrial function of ovarian granulosa cells, thus playing a role in the energy supply and metabolism of oocytes, leading to ovarian hypofunction or even failure.

(3) NMN can effectively improve the content of NAD^+ in ovaries, and play a role in preventing, repairing and improving ovarian function caused by ionizing damage.

(4) NMN is proposed to preserve ovarian function by regulating granulosa cell glucose metabolism and mitochondrial dynamics through activation of the PI3K/AKT signaling pathway.

The objectives of this thesis are:

(1) An animal model of ovarian dysfunction caused by ionizing radiation (simulated radiotherapy) was established. In vivo experiments were performed to detect the changes in ovarian function-related phenotypes after radiation damage and the protective effect of NMN on ovarian function in model mice after prevention and treatment.

(2) Through the analysis of ovarian tissue transcriptomics, explored the possible roles and targets of ionizing radiation damage to ovarian function were explored, as well as the effects and targets of NMN on ovarian function changes after prevention and treatment.

(3) In vitro experiments using ovarian granulosa cell lines (KGN) were conducted to investigate the protective mechanisms of NMN against oxidative stress-induced damage. The study explored specific pathways and targets of NMN for protecting granulosa cells and improving ovarian function through three key approaches: regulating oxidative stress, optimizing glucose metabolism, and enhancing mitochondrial function.

Chapter II. Establishment of IR-Induced POI Model in Mice, and NMN Intervention on Phenotype

To evaluate the NMN’s effects on follicular development in radiation- damaged mice, we established an ionizing radiation (IR) ovarian injury model using C57BL/6J mice. The experimental group received daily oral NMN supplementation. We monitored body weight and estrous cycles dynamically, calculated ovarian weight ratios after tissue sampling, and observed follicular morphology using HE staining. Quantitative analysis of primordial, growing, antral, and atrophic follicles was performed to assess ovarian reserve function. Serum AMH and FSH levels were measured by to systematically evaluate the effects of NMN on improving ovarian reserve in radiation-exposed mice.

1. Materials and Methods

1.1. Animals and Materials

Animal models were constructed using female C57BL/6J inbred mice with an average age of 7 weeks. SPF-grade mice were purchased from SLECK JINGDA Laboratory Animal Co., Ltd. (Hunan, China). The animals were housed in SPF-grade animal facilities, the temperature range of 20-25℃ and humidity around 50%, with free access to drinking water and pelleted feed. Lighting was maintained at alternating 12 hours light-dark cycles. All mice were acclimated in the SPF animal facility for one week prior to the start of experiments. The breeding and all experimental animals were approved by the Animal Management Institution (SYXK XIANG 2022-0008) and the Ethics Committee of the University of SouthChina (No. USC2023XS120) and conducted in accordance with the animal management guidelines published by the National Institutes of Health. All animal handling procedures complied with humanitarian standards.

The experimental materials in this study were the main reagents and instruments listed in Table 1-2.

Table 1. Main reagents for the experiment

Name of reagent	manufacturer
β-Nicotinamide mononucleotide	Shenzhen Hija Biotechnology Co., LTD. (China)
Wright′ s stain solution	Thermo Fisher Scientific (USA)
Dimethylbenzene	Sigma-Aldrich (Merck KGaA, Germany)
4% polyformaldehyde	Electron Microscopy Sciences (USA)
Eosin stain	Thermo Fisher Scientific (USA)
Sudomus dye	Sigma-Aldrich (Merck KGaA, Germany)

Table 2. Main experimental equipment and instruments

Instrument name	model	manufacturer
light microscope	SY100	NIKON(Japan)
Organize automatic embedding machine	HD-310	Hubei Huida Instrument Co., LTD. (China)
micropipet	10 μL	Eppendorf (Germany)
Paraffin sectioning machine	HI 1210	Leica (Germany)
Biological irradiator	HXFS-IA	China Nuclear Power Research Institute (China)

1.2. Experimental Methods

1.2.1. Preparation of Animal Experiment Reagents

Preparation of NMN solution (animal experiment)

Prepare NMN powder, sterile saline solution, a precision balance, and a magnetic stirrer before the experiment. 500 mg of NMN powder dissolved in 5 mL sterile saline solution (100 mg/mL). Transfer the solution to a magnetic stirrer and set the stirring speed to 850 rpm for continuous mixing. Monitor the dissolution process of NMN

powder in real time until all solid particles are completely dissolved, resulting in a colorless solution. Strictly follow the 'use-by date' principle and any unused portion must be discarded immediately.

Preparation of 20% Uralan solution

Prepare Uralan powder, an electronic microbalance, sterile saline solution, and a magnetic stirrer. Accurately weigh 5 g of Uralan powder and dissolve it in 25 mL sterile saline solution in a glass bottle. Place the mixed solution on the magnetic stirrer and set the stirring speed to 850 rpm until completely dissolved. The final Uralan anesthesia working solution with a concentration of 20% is obtained and stored at room temperature.

1.2.2. Animal Model Construction, Grouping and NMN Intervention

This experiment utilized 40 SPF-grade female C57BL/6J inbred mice around 7 weeks old with an average body weight of (18.0±2.0) g. The mice were housed in temperature maintained between 20-25°C and humidity around 50%, maintaining a standard circadian rhythm of 12:12 hour cycles. Free access to pellet feed and drinking water was provided.

After one week of acclimatization feeding, the mice were divided into four groups: Ctrl group (control group), 5Gy group (radiation group), 5Gy+NMN group (treatment group), and NMN group (drug control group), n=10.

First, both the 5Gy+NMN group and NMN group received NMN (500 mg/kg based on each mouse's body weight) for 28 consecutive days, while the remaining two groups received equal volumes of normal saline for the same duration. After 28 days of medication, cesium-137 γ irradiation was administered to both 5Gy and 5Gy+NMN groups using SouthChina University's HXFS-Ⅰ A biological irradiator (radiation dose rate: 120.8 cGy/min, irradiation time: 219 seconds, total dose: 5 Gy). Following irradiation, the 5Gy+NMN and NMN groups continued receiving NMN (500 mg/kg based on each mouse's body weight), while the other two groups received equal volumes of normal saline for another 28 consecutive days. Vaginal smears were performed ten days before the ending of the experiment, we continuously observe the changes of the estrous cycle in each group of mice. It was found that most of the mice after radiation were in the estrous period, and it was preliminarily judged that the ionizing radiation mouse model was successfully constructed.

1.2.3. Collection of Specimens for Experiments

After completing the experiment, mice were anesthetized via intraperitoneal injection of a 20% urethane solution (3 mL/kg). The final body weight was measured post-anesthesia. When achieving deep anesthesia, the mice were positioned in a supine position and secured. The chest skin was disinfected with alcohol. Using a prepared 1ml syringe, the needle was inserted slightly left or right of the xiphoid process at an angle of 20°-30° toward the left thoracic cavity near the heart. A 0.5-1cm depth was slowly penetrated into the ventricle, followed by aspiration to collect approximately 1ml of whole blood. The blood was transferred to a non-anticoagulant test tube and centrifuged at 4°C, 3000 rpm for 10 minutes. The serum layer was collected and transferred to new EP tubes for -80°C preservation for ELISA testing. Sex hormones AMH and FSH were also analyzed.

The mice were dissected under sterile conditions, with bilateral ovarian tissues isolated and immediately placed on ice to remove surrounding structures, including fallopian tubes, fat, and capsules. Wet weight measurements were taken using a micrometer and recorded. The ovarian tissues were washed three times with pre-cooled PBS solution to remove blood and oils, followed by surface moisture absorption on filter paper. Left ovarian tissue samples from each group were immediately immersed in 4% paraformaldehyde fixative, fixed at room temperature for 24 hours, and subsequently processed through graded ethanol concentration for paraffin embedding. The specimens underwent HE staining for histopathological examination of ovarian changes and follicle counts. Right ovarian tissues from each group were rapidly frozen in liquid nitrogen within storage tubes and preserved at -80°C freezers for subsequent molecular biology and omics analyses.

1.2.4. General Observation of Mice

Observe the eating, drinking, hair, activity and excrement of each group of mice every day. The condition was described, and the body weight of each group of mice was weighed and recorded to monitor for adverse reactions the general growth and development status of each group of mice.

1.2.5. Vaginal Smear and Estrous Cycle Detection

Ten days prior to model completion, vaginal smear collection was performed daily from 11:00 AM to 12:00 PM. Preparations required one day in advance, marking the frosted surface of slides with pencil labels for grouping and numbering, preparing 0.9% sterile saline solution, sterilized medical cotton swabs, and a 10 μL pipette (with matching sterilized tip). During sampling, the mouse was restrained with the left hand to lie supine and expose the vaginal opening. Sterile cotton swabs were gently wiped on the vulvar area 2-3 times, followed by precise aspiration of 10 μL saline using a high-pressure sterilized pipette. The saline solution was slowly injected into the vaginal fornix, then gently aspirated and rinsed three times. Collected fluid was piped onto slides and spread evenly using a Tip head to ensure uniform cell distribution. The prepared slides were dried in a 37°C oven for 1-2 hours, then stained with Wright's stain solution. After drying, microscopic observation and photography of typical field images were performed.

The estrous cycle of normal C57BL/6J mice typically lasts 4-5 days. By analyzing changes in cellular types within vaginal smears and combining morphological characteristics, researchers can accurately identify specific estrous stages: nucleated epithelial cells (preestrus), keratinized cells (estrus), leukocytes (interestrus), and mixed cells (postestrus). Post-exposure studies revealed that most irradiated mice remained in the estrus phase, indicating successful establishment of the IR mouse model.

1.2.6. Mouse Gavage or Equal Volume of Saline

This study employed SPF-grade female C57BL/6J inbred mice administered via oral gavage. The treatment was administered daily from 9:00 AM to 10:00 AM for a total duration of 56 days (28+28 days), corresponding to one month before radiation exposure and one month after. Following pre-approval of animal ethics guidelines (No. USC2023XS120), mice were divided into four groups randomly (n=10 per group). Two researchers independently performed both administration and endpoint evaluations. The dosage was determined by each mouse's body weight on the day of

administration (500 mg/kg, dissolved in sterile saline, freshly prepared and used). Control group mice received the same amount of saline as the 5Gy+NMN group. If a control or 5Gy group mouse exhibited low body weight (<10 g) or abnormal conditionality, the procedure was paused once, if suspended three consecutive times, the animal was removed from the study. No fasting or water restriction was required prior to administration. The injection was administered using a 24 G × 25 mm stainless steel bulb connected to a 1 mL sterile syringe (minimum reading 0.01 mL). All equipment included an electronic balance, disposable gloves, an isoflurane induction chamber (for brief sedation when necessary), and lubricant (sterile saline solution).

Specific operational steps

Animal preparation and measurements

（1）Weigh, calculate individual dose volume and print/fill in the dosage sheet.

（2）Check the animal's health condition: mental, respiratory, fur and body surface integrity. If dyspnea, obvious emaciation or hemolytic diarrhea exists, postpone the administration and record it.

Feeding tube length determination

Measure the feeding tube along the corner of the mouth to the root of the ear to the last rib and mark it on the tube (i.e., the expected length into the stomach). Prevent too deep or too short.

Fixation and catheterization

Scraping Neck Fixation Technique: Hold the neck skin between thumb and index finger to lift it, positioning the head and neck in a straight line with upper and lower incisors exposed. Gently elevate the palate to align the oral axis with the esophagus. Insert the feeding tube along the midline of the palate slowly. Avoid forceful pushing when encountering resistance. Once the tube reaches the target mark, allow it to slide freely into the esophagus.

An Error in the trachea indicates

When coughing, violent struggling, or altered breath sounds occur, immediately withdraw the animal. Allow it to calm down before attempting again or terminate the procedure. Administer the medication smoothly (10-20 seconds/0.2-0.3 mL) to prevent high-pressure reflux. Remove the feeding tube and gently return the animal to the observation cage for 30 minutes.

Sedation/anesthesia

Low concentrations of isoflurane were used only for a short time to induce extreme distress or a special model, and were removed when the operation was completed.

Safety and complications management

(1) Aspiration/pneumonia: Stop immediately. Stop the administration of drugs in case of bronchial aspiration, remove the gastric needle, and give humane treatment if necessary.

(2) Esophageal/gastric perforation: manifested as drooling, dyspnea, abdominal distension, bloody discharge; seek medical attention immediately and record the case.

(3) Stomach distension/reflux: control volume and injection speed, optimize formula viscosity; give drugs in several times when necessary (≥30 min).

(4) Reactive response: shorten the operation time, fix the technique and be consistent, reduce unnecessary fasting.

Dosing records and quality control (QC)

(1) Individual records: date, time, animal ID, weight, calculated volume, actual volume, formula/batch number, operator, success of one catheter placement, abnormalities and treatment.

(2) Operational consistency: The same study should be performed by the same or a small number of skilled operators; cross-calibration should be performed at the beginning of a new batch.

(3) Exposure consistency verification (optional): Randomly select a number of mice and take blood after the first dose (e.g., 0.5-2 h) to detect blood drug concentration and verify the inter-group/small mouse consistency of bioavailability.

Criteria for human endpoints and exclusion

Weight loss>15-20% or less than 10 g for a week, inability to eat and drink, persistent dyspnea, no response, severe abdominal distension/bloody stool, etc.; if the criteria are met, please leave the group immediately, and humane treatment is necessary if needed.

1.2.7. Detection of Serum Sex Hormone AMH and FSH Levels

Anesthetize mice intraperitoneally with a 20% urethane solution. After cardiac puncture for blood collection, euthanize the mice post-collection. Centrifuge the blood at 4°C, 3000 rpm and 10 minutes, then aspirate the serum layer and transfer it to fresh EP tubes. Samples were stored at −80°C and then analysis, with repeated freeze−thaw cycles strictly avoided. Before testing, retrieve the serum from the refrigerator, allow it to stand at room temperature for 30 minutes, then vortex-shake the mixture to ensure thorough mixing.

The levels of AMH and FSH were determined by a mouse-specific ELISA kit (R&D Systems, MN, USA) as per manufacturer instructions, with absorbance at 450 nm for concentration determination. The sandwich ELISA method was employed for AMH and FSH assays, with each plate containing blanks, zero standards, 6-8point calibration curves, and dual-level internal controls. Samples were initially diluted according to protocol specifications (AMH/FSH 1:2–1:10), with duplicate wells for each standard, sample, and control. Incubation, plate washing, color development, and termination, with readings taken at 450 nm and reference calibration using wavelengths between 570 and 630 nm. Sample concentrations were calculated from logistic model based standard curves, with only results falling between the lower and upper limits of quantification included in the analysis. The samples that exceeded these limits were diluted and retested. The intra-well coefficient of variation (CV) was ≤10%, the inter-well CV was ≤15%, and spiked recovery and dilution linear controls were maintained within 80-120%. Batch switching was validated through Passing-Bablok regression. Statistical analysis was conducted using R or Prism software, with group comparisons selected based on distribution characteristics, reporting effect sizes and 95% confidence intervals (CIs). Multivariate models incorporated the estrous cycle, age, body weight, and plate number as covariates.

Specific test steps

Plate pretreatment

The purchased pre-wrapped plate can be used directly.

Sample dilution

AMH/FSH: Initial recommendation 1:2-1:10;

The optimal dilution ratio was determined by a small-scale "range exploration plate" to ensure that the reading fell in the middle of the standard curve (OD≈0.3-2.0).

Assay and incubation, sandwich method (AMH/FSH)

Each well was filled with 100 μL standard/control/sample.

Incubate at 37 °C for 60-90 min or at room temperature for 1-2 h (according to instructions; slight shaking is allowed).

Wash plate: 300 μL/cell, ≥3-5 times, and dry.

Add the secondary antibody (HRP conjugate) 100 μL / hole and incubate at room temperature for 30-60 min.

Wash the plate again for more than 5 times and dry it.

Add 100 μL of TMB substrate per well and color under light for 10-20 min (monitor blue development).

Add 100 μL of terminal solution per well (yellow).

Reading: Main wavelength 450 nm, reference 570-630 nm. Record the original OD and corrected OD (450-630 nm).

Layout of the panels

Standards for each first/last plate, interspersed with low/high quality control and repeated samples.

Avoid edge effects: leave the edge holes blank/balanced holes, or randomly arrange the samples and include the ‘board/row/column’ effect test in the statistics.

1.2.8. Preparation of Paraffin Sections

Fixation and washing

The ovary was placed in an appropriate amount of 4% polyformaldehyde and fixed for 24 h. The fixative should be applied 2-3 times over the tissue block, and then the fixative was replaced with water and soaked for 12 h.

Gradient dehydration

（1）The ovarian tissue was labeled and placed in an embedding box.

（2）Put it into the dehydrator cylinder and operate according to the gradient dehydration method:

70% alcohol (40 min), 80% alcohol (40 min), 90% ethanol (40 min), 95% ethanol (40 min), 95% ethanol (40 min), anhydrous ethanol I (40 min), anhydrous ethanol II (40 min)

（3）Replacement ethanol: alcohol: xylene = 1:1 (15 min).

（4）Xylene is transparent: Xylene I (60 min), Xylene II (60 min).

（5）Infiltration wax: hot wax I (55°C,15 min), hot wax II (65°C, 20 min).

Embedding

Before embedding, ensure sufficient paraffin stock in the wax bath and pre-set the paraffin melting temperature. Pour preheated liquid paraffin into the mold base, then align tissues vertically using forceps at the center to maintain uniform orientation across samples. For ovarian tissue, specifically orient the genitalia side toward the same mold side to maximize cross-sectional area during subsequent sectioning. Slowly fill the wax bath until fully submerged, then lay coded label sheets flat on the tissue surface with corresponding information matching each sample. After complete room-temperature solidification, open the mold and cut the wax block along labeled boundaries to obtain individual sample blocks. Transfer the prepared ovarian tissue blocks to 4°C or -20°C refrigerators for storage.

Cut into slices

Secure the freeze-treated wax block firmly on the paraffin sectioning machine's stage and adjust the thickness to 25 μm using a precision knob. Begin by trimming excess wax with a coarse blade to expose the maximum tissue cross-section, then set the cutting depth to 5 μm for continuous sectioning. Immediately transfer the prepared sections to a 46-48 °C constant-temperature stretcher for expansion. Once fully flattened, select either standard or adhesive slides as required for mounting. After labeling sample information, place the slides in a 37 °C drying oven for overnight exposure to air.

1.2.9. HE Staining

Wax chip dewaxing treatment

The procedure follows standard histological protocols with the following steps: First, after drying, sequentially immerse the paraffin sections in xylene I (10 minutes), xylene II (10 minutes), and a xylene-anhydrous ethanol mixture (volume ratio 1:1, 10 minutes). Subsequently, perform gradient alcohol dehydration as described in Section 1.2.8 above. Before changing solutions at each step, ensure complete removal of residual liquid from the section surface.

The HE staining procedure is as follows

After decolorization, sections were stained with hematoxylin solution for 8 minutes, followed by 3-minute rinsing under running water to remove surface coloration.Following staining, tissue sections were immersed in a 1% hydrochloric acid−alcohol differentiation solution for approximately 3 to 5 seconds, immediately rinsed with distilled water to terminate the differentiation process, and rinsed continuously for 20-30 minutes to complete the counterstaining. The sections were subsequently stained with eosin for 1-3 minutes. Subsequent treatments included deiodination using anhydrous ethanol I (30 seconds) and anhydrous ethanol II (30 seconds), followed by transparency treatment with xylene I (10 minutes) and xylene II (10 minutes). After mounting with neutral resin, the sections were dried in a 37°C incubator for 24 hours, and finally observed and photographed under an optical microscope.

1.2.10. Follicle Count at All Levels

The follicles were classified and counted using the Kalich-Philosoph method[129], with minor modifications. All counts were performed by two independent researchers who were unaware of the experimental group's identity. Specifically, ovarian sections were prepared with a thickness of 5 μm through serial sectioning, with HE staining applied every five sections. Follicles were enumerated only when the oocyte nucleus was distinctly visible. The number of follicles at each developmental stage was obtained by averaging counts from every fifth section and multiplying by a correction factor of 5 to estimate the total ovarian follicle count[130]. Data were presented as follicle counts per developmental stage (n = 10 ovaries per group).

The grading criteria for follicles[131], [132]

(1) The primordial follicle is defined as containing a complete oocyte and surrounded by a single layer of flat squamous granular cells the egg follicle.

(2) Primary follicles are defined as oocytes surrounded by a single layer of cuboidal granular cells.

(3) Secondary follicles are defined as those with two or more layers of visible cuboidal granular cells, but without sinuses Cavity follicles.

(4) A sinus follicle is defined as an oocyte containing several layers of granulosa cells with a clear nucleus. The oocyte is located in an eccentric position and surrounded by the cumulus complex. The granulosa cell layer is highly differentiated. The follicular cavity is significantly expanded and filled with follicular fluid.

(5) The arrested follicle oocytes showed characteristic degenerative morphological changes, with nuclear condensation, highly condensed and deeply stained chromatin, and disordered and destroyed granular cell layers.

1.3. Statistical Analysis

All data were analyzed with at least three replicates. Shapiro-Wilk tests were first conducted to assess normality. Normally distributed variables were compared among groups using one-way analysis of variance (ANOVA), and post hoc multiple comparisons were performed with Tukey’s test. Results are presented as the mean ± standard deviation (M ± SD). For non-normal distributions, Kruskal-Wallis H tests were used for inter-group comparisons, with results expressed as median and interquartile range. All statistical analyses were performed using GraphPad Prism 9.0 software, with statistical significance defined as $P < 0.05$.

2. Results

2.1. Effects of Ionizing Radiation on Body Weight in Mice and Changes in Body Weight after NMN Intervention

To establish mouse models, cesium-137 γ radiation (simulating radiotherapy) was administered systemically. From the initial entry into SPF animal facilities until 28 days after radiation modeling completion, daily weight measurements and records were taken at 8:00 AM to monitor survival status and evaluate the effects of radiation and the intervention drug NMN on body weight. Results showed no significant difference in average body weight among groups before radiation intervention (4 weeks prior to formal trials, 28 days). Following radiation modeling, the 5Gy group exhibited a gradual weight decline with marked reduction observed by the 6th week of formal trials (Figure 1). This demonstrated statistically significant differences compared to control groups and the 5Gy+NMN group.

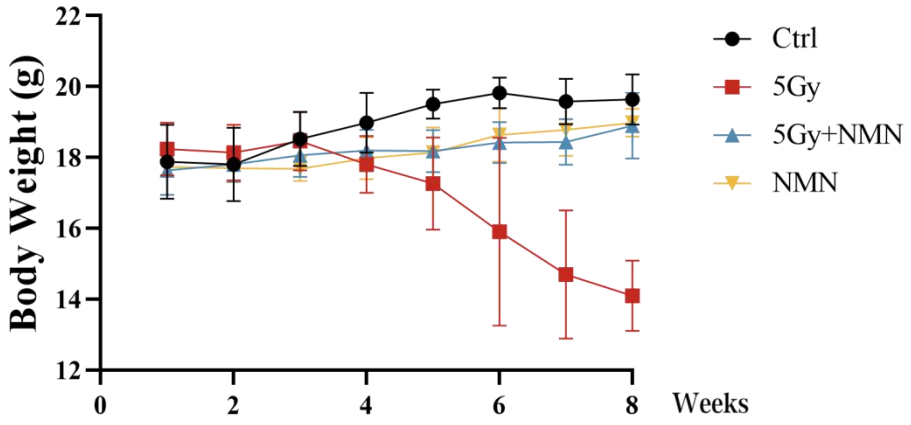

Figure 1. Changes in body weight of mice after ionizing radiation and NMN intervention
The 5Gy group showed a significant weight difference compared to the Ctrl group starting from week 5 ($P < 0.05$), with the disparity becoming more pronounced from week 6. The 5Gy group experienced a marked weight loss ($P < 0.001$). When comparing the 5Gy group with the 5Gy+NMN group, the 5Gy group initially showed a weight decrease compared to the 5Gy+NMN group starting from week 5 ($P < 0.05$). From week 6 onward, the weight difference became more apparent, with the 5Gy group again demonstrating a significant weight loss ($P < 0.001$). n=10.

2.2. Effects of IR on Estrous Cycle in Mice and Changes after NMN Intervention

Ten days before the end of the experiment, we began collecting vaginal secretions from each group of mice daily between 10:00 AM and 11:00 AM to perform progressive smear examinations, dynamically monitoring changes in estrous cycle patterns across groups. Our findings revealed that radiation-induced modeling significantly disrupted estrous cycle regularity, with most mice remaining in the estrous phase. Notably, NMN intervention demonstrated a restorative effect on these disrupted cycles (Figures 2 and 3).

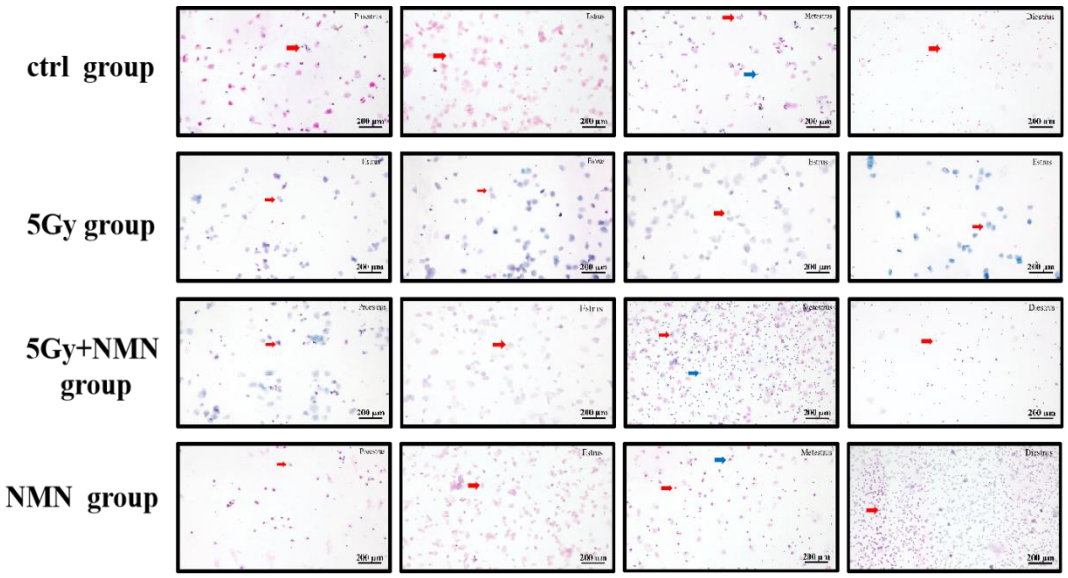

Figure 2. Vaginal smears of mice in each group

The vaginal cytological smears from mice were stained using the Rigi composite staining method. P: Proestrus (pre-luteal phase); E: Estrus (luteal phase); M: Metestrus (post-luteal phase); D: Diestrus (interluteal phase). The red arrows indicate nucleated epithelial cells, blue arrows represent squamous epithelial cells, and scattered small dots denote white blood cells. n=5

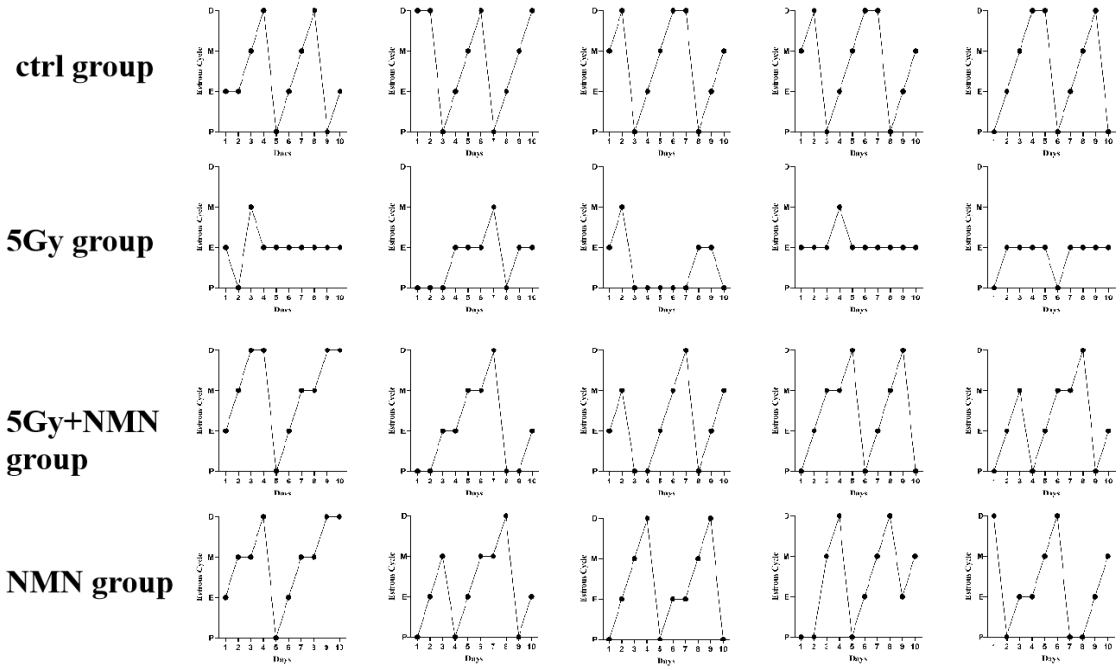

Figure 3. Line graph of vaginal smear of each group showing changes in the estrous cycle

Five mice were randomly selected from each group and the line graph of image results analysis was analyzed for 10 consecutive days. The 5Gy group showed obvious cycle disorder of estrus, and most of the smear results suggested that it was in the estrus period. However, the other three groups showed obvious periodic changes of the estrous cycle.

2.3. Changes in ovarian volume, morphology and follicle count of mice after radiation and changes after NMN intervention

After cleaning the bilateral ovarian tissues of each group of mice on ice, the wet weight (g) of both ovaries was measured on a microbalance and recorded. The corresponding ovarian index (the ratio of the average weight of both ovaries to the final body weight of the mouse, measured in g) was calculated for quantitative analysis. Morphological changes in the ovaries were observed and photographed. Macroscopic examination revealed that the 5Gy group exhibited significantly smaller bilateral ovarian volumes compared to the other three groups, with smoother ovarian surfaces and no obvious post-ovulation scarring observed.

Ovarian index analysis showed a significantly lower level in the 5Gy group compared to the Ctrl group. The 5Gy+NMN group exhibited ovarian indices similar to both the Ctrl and NMN groups, while showing a significant difference compared to the 5Gy

group. This indicates that NMN intervention in vitro reversed the radiation-induced decline in ovarian index (Figure 4B).

Figure 4. Changes of ovarian volume, morphology and ovarian index (ovarian weight ratio) in groups after radiation and the effect of NMN intervention

(A) Anatomical gross appearance of ovaries in each group of mice; (B) Changes in ovarian index (ovarian weight ratio) in each group of mice; n=10, *** P <0.001

After performing HE staining on ovarian tissues from each group of mice, morphological analysis and follicle count at various stages revealed significant abnormalities under optical microscopy. In the 5Gy irradiation group, HE-stained sections showed collapsed and fragmented granulosa cell layers with no detectable oocytes in most follicles, while primordial follicles were notably reduced. The central medulla of the ovaries also exhibited marked collapse and disorganization. All other groups maintained well-developed follicular-like structures with multilayered granulosa cells arranged orderly, visible oocytes, distinct follicular cavities, and a moderate proportion of primordial follicles (Figure 5). These findings indicate that NMN demonstrates protective effects against radiation-induced ovarian damage.

The histological section analysis revealed quantitative changes in follicular counts across different developmental stages. Compared to the control group, the 5Gy treatment significantly reduced primordial and growing follicles (including primary and secondary follicles), while also showing a marked increase in atretic follicles and a moderate decrease in antral follicles. Both the 5Gy+NMN and NMN treatment groups exhibited follicular characteristics comparable to those in the control group.

The 5Gy+NMN group showed statistically significant increases in both primordial and growing follicles compared to the 5Gy group, with a marked reduction in antralized follicles. This suggests NMN exerts protective effects on maintaining

normal ovarian follicular hierarchy in radiation-damaged ovaries. Notably, control mice receiving NMN treatment demonstrated no significant adverse effects on follicular quantity or developmental progression across all follicular stages (Figure 6).

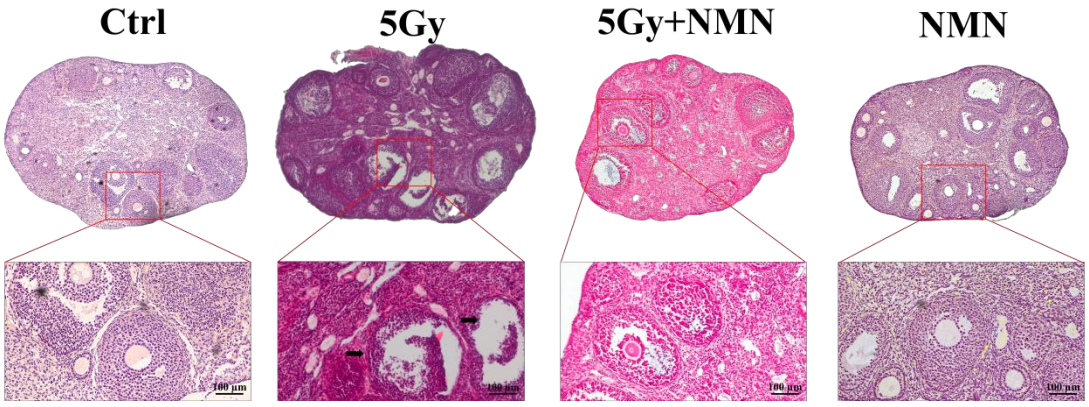

Figure 5. Morphological and structural changes of follicles at all levels in ovarian tissues of mice after radiation and the effect of NMN intervention

HE stained sections of ovaries from each group of mice and magnified 100 times, n=10, the red arrow indicates occluded follicles

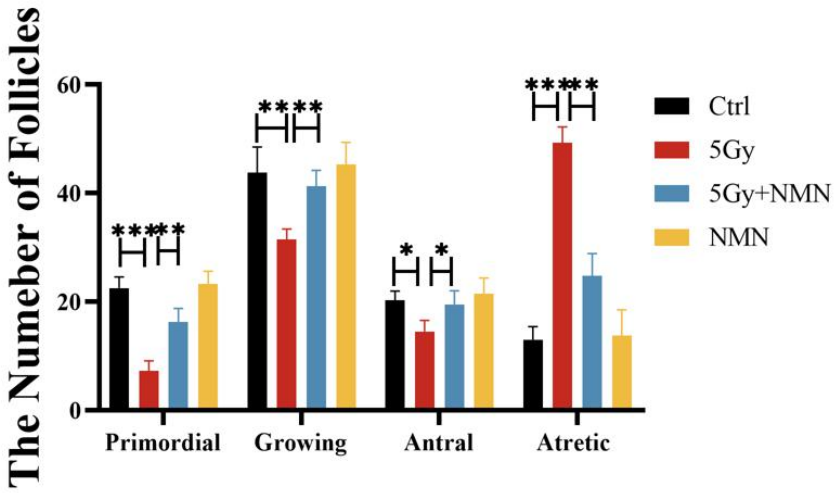

Figure 6. Changes in the number of follicles at all levels in the ovaries of mice after radiation and effects of NMN intervention

Number and comparison of primordial follicles, growing follicles (primary follicles and secondary follicles), antral follicles and closed follicles in each group; n=10, *** P <0.001

2.4. Changes of Serum Sex Hormones in Mice after Radiation and Effects of NMN Intervention

Serum samples from each group of mice were analyzed using radioimmunoassay to detect serum AMH and FSH levels. Experimental data showed that the levels of

serum AMH in the 5Gy group significantly decreased compared to other groups, while FSH levels showed a marked increase. After NMN intervention, these hormone levels returned to control group levels with no significant difference between NMN and control groups (Figures 7A, B). This indicates successful radiation modeling that indeed affected sex hormone levels representing ovarian function and reserve capacity. NMN intervention reversed these hormone levels, aligning sex hormone levels related to ovarian reserve with those of the control group. However, when normal mice received routine NMN doses, no significant impact was observed on normal sex hormone secretion fluctuations. This suggests NMN only affects ovarian function damaged by radiation, without influencing normal ovarian function.

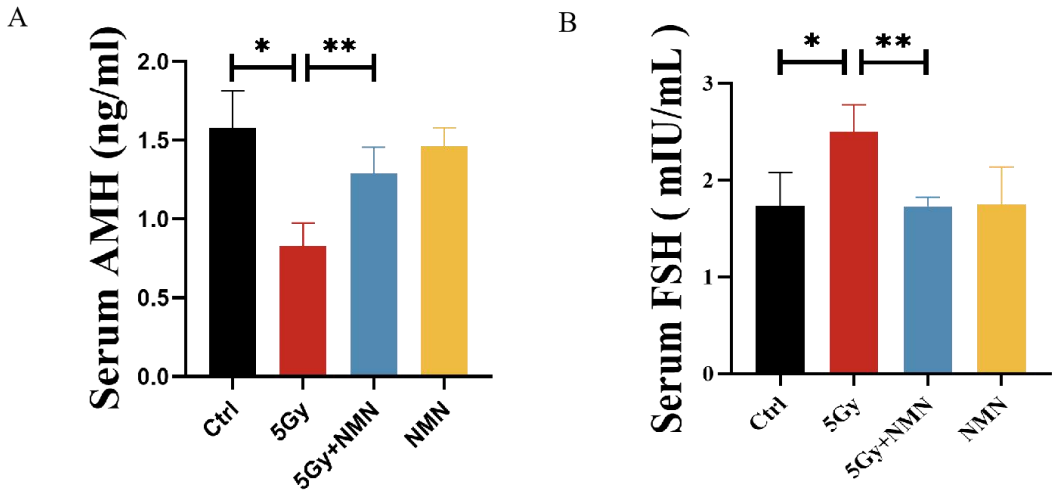

Figure 7. Sex hormone changes in groups of mice after radiation and the effect of NMN intervention

(A) serum sex hormone AMH content of each groups; (B) serum sex hormone FSH content of each groups. n=5, *P < 0.05, **P < 0.01

3. Discussion

This study successfully established an ionizing radiation-induced ovarian failure model in mice through cesium-137 γ ray exposure. Compared with the control group, irradiated mice exhibited significant weight loss and marked reductions in ovarian parameters (volume, weight, and follicular cell counts), indicating diminished reproductive potential. Additionally, the irradiated mice showed disrupted estrous cycles and serum changes in ovarian reserve hormones (AMH and FSH), which closely correspond to clinical manifestations of ovarian reserve decline. These

findings demonstrate that cesium-137 γ ray effectively simulate human radiotherapy-induced ovarian damage, establishing a reliable model for research.

Previous studies have demonstrated that ionizing radiation causes ovarian damage through two primary mechanisms: direct DNA double-strand breaks leading to oocyte death, and indirect disruption of the ovarian microenvironment via excessive reactive oxygen species (ROS) production, which induces follicular atresia[134], [135] . Given the limited regenerative capacity of mammalian follicles, any depletion of follicular reserve in a culture bank results in irreversible ovarian dysfunction[136]. Therefore, developing animal models to simulate radiation-induced premature ovarian failure holds significant clinical translational value.

This study represents the first evaluation of NMN in an IR model. Results demonstrated that NMN significantly improved ovarian morphology and function across the entire radiation cycle (pre-radiation, during irradiation and post-radiation) whether administered as preventive treatment or therapeutic intervention. Key improvements included partial recovery of ovarian weight and volume, increased follicular count at all stages, reduced antral atresia, alleviated estrous cycle irregularities, elevated serum AMH levels, and decreased FSH concentrations. These findings suggest NMN may mitigate radiation-induced ovarian cell apoptosis by restoring NAD^+ levels, improving oxidative stress, and regulating energy metabolism. Notably, administration of safe NMN doses in normal mice showed no adverse effects on ovarian function, indicating its clinical applicability and safety profile.

In conclusion, this study has not only successfully established a cesium-137 γ ray-induced premature ovarian failure model in mice, but also preliminarily demonstrated the protective effective potential of NMN to radiation-induced ovarian damage. These findings give new insights for the prevention and therapy of radiation-induced ovarian dysfunction. However, the precise mechanisms of the effects of NMN require further elucidation through multi-omics approaches such as transcriptomics, metabolomics, spatial omics, and high-throughput technologies like single-cell sequencing. Additionally, its long-term safety profile, optimal administration timing, and dosage requirements need to be validated through expanded animal models and clinical trials.

4. Summary

In summary, we successfully established an IR induced premature ovarian failure (POF) model in mice. Exposure to cesium-137 γ radiation caused significant impairment of ovarian function, ultimately leading to POF. The radiation treatment resulted in reduced body weight, decreased ovarian volume and weight, along with marked reductions in primordial, primary and secondary follicles, accompanied by a substantial increase in atretic follicles. Additionally, the radiation disrupted estrous cycles, manifested by decreased serum AMH levels and elevated FSH levels, indicating diminished ovarian reserve. These findings confirm the successful creation of a POF model using cesium-137 γ radiation to simulate human radiotherapy. Notably, preventive administration of NMN four weeks prior to radiation and therapeutic NMN supplementation four weeks post-radiation demonstrated effective ovarian protection. In contrast, normal mice receiving safe NMN doses showed no observable impact on ovarian function.

Chapter III. Mechanism of the Protective Effect of NMN on Ovarian Function in Mice Radiation Injury Model

Radiation therapy serves as a cornerstone of comprehensive treatment for gynecological tumors, colorectal cancers, and pediatric malignancies, particularly in Italy where cervical and rectal cancers predominantly affect women of reproductive age. However, pelvic radiation exposure causes irreversible ovarian damage, leading to prolonged quality of life decline and infertility in survivors. Human oocytes exhibit exceptional sensitivity to IR, with approximately 2 Gy depleting about 50% of primordial follicle reserves. When ovarian radiation doses exceed 20 Gy on average, acute ovarian failure (AOF) and POI become unavoidable risks, which vary with individual ovarian reserve and age[137] . Clinical guidelines recommend maintaining uniform radiation exposure below 2-4 Gy during radiotherapy plans. Yet this goal proves challenging for young patients undergoing full pelvic or whole-body irradiation[138]. Current fertility preservation strategies including ovarian transplantation, shielding techniques, GnRH-a injections, and cryopreservation of oocytes/embryos/ovarian tissue which focus on addressing anatomical changes or supporting assisted reproductive technologies[139] while lacking pharmacological radiation protection targeting ovarian cell ecology. Therefore, developing drugs that preserve ovarian reserve and endocrine function without compromising anti-tumor efficacy remains a critical clinical imperative.

IR plays a role by inducing DNA double strand break, increasing ROS, loss of mitochondrial membrane potential, ovarian microvascular damage, and triggering programmed death of oocytes and follicular granulosa cells[140].

Multiple preclinical studies in reproductive biology demonstrate the protective potential of NMN for ovarian function. In female aging models, NMN restores ovarian and oocyte NAD^+ levels, improves meiotic spindle and chromosome separation defects, and enhances early embryonic development with favorable fertility outcomes[141]. In chemotherapy-induced ovarian toxicity models, NMN upregulates NAD^+ /SIRT2 and inhibits Granulosa cell pyroptosis, thereby maintaining ovarian reserve and endocrine function[142]. Under metabolic stress conditions like diabetes, NMN improves mitochondrial function, reduces ROS, and mitigates DNA damage to enhance oocyte maturation and quality[143]. Comprehensive metabolic studies

further indicate that enhancing the NAD^+ metabolite profile significantly reduces chemotherapy-induced ovarian toxicity and preserves fertility[144]. Although most of these studies focus on non-radiotherapy scenarios, they collectively highlight the core concept that upregulating NAD^+ provides multi-pathway protection for ovarian cells and organs.

However, there remains a research gap regarding the effect of NMN in improving ovarian dysfunction or even regression following radiotherapy or IR. Current studies lack definitive dosage-response relationships and causal mechanisms linking its specific effects. To address these gaps, this study investigates the Protective Effects of NMN on Radiation-Damaged Ovarian Function and Its Mechanisms. Through systematic evaluation in animal models of radiotherapy, we aim to elucidate NMN's protective actions by clarifying its role in reconstructing a multi-layered protective network: enhancing NAD^+ levels, improving energy metabolism (glycolysis), reducing oxidative stress, maintaining mitochondrial homeostasis, and mitigating apoptosis. The research also proposes feasible intervention strategies and methods focusing on dosing timing, safety, effectiveness, and translatability and complementarity with existing fertility preservation approaches.

1. Materials and Methods

1.1. Experimental Materials

The experimental materials in this part mainly consist of antibodies (Table 3), main reagents for qRT-PCR experiment (Table 4), and main reagents for Western Blot and immunohistochemistry (Table 5). The main instruments and equipment are shown in Table 6.

Table 3. Experimental antibodies

Antibody/Reagent	Catalog No.	Manufacturer
PKM2	D78A4	Cell Signaling Technology
β-Tubulin	AC008	ABclonal Technology Co.,Ltd.
HK2	C64G5	Cell Signaling Technology
LDHA	C28H7	Cell Signaling Technology
BAX	T40051	Aibimat Medical Technology Co., LTD

Bcl-2	ARC0173	Thermo Fisher Scientific company
Caspase-3	#9662	Cell Signaling Technology
MDA	ab243066	Abcam plc
SOD	A19576	ABclonal Technology Co.,Ltd.
PI3K	A27717	ABclonal Technology Co.,Ltd.
P-PI3K	AP1463	ABclonal Technology Co.,Ltd.
AKT	A17909	ABclonal Technology Co.,Ltd.
P-AKT	AP1208	ABclonal Technology Co.,Ltd.
HIF-1α	A26899	Wuhan San Ying Biotechnology Co., LTD
HRP-conjugated affinipure goat anti-mouse IgG (H+L)	SA00001-1	Wuhan San Ying Biotechnology Co., LTD
HRP-conjugated affinipure goat anti-rabbit IgG (H+L)	SA00001-2	Wuhan San Ying Biotechnology Co., LTD

Table 4. Main reagents for qRT-PCR experiment

Name of Reagent	Manufacturer
AG RNAex Pro RNA extraction reagent	Hunan Aikori Bioengineering Co., LTD. (China)
Reverse transcription kit	Beijing Quanshi Jin Biotechnology Co., LTD. (China)
Upstream and downstream primers for related proteins PCR	Shanghai Shenggong Bioengineering (Co., Ltd.) (China)
SYBR GREEN staining solution	Jiangsu Novozymes Bioengineering Co., LTD. (China)
Urase	Shark Biotechnology Co., Ltd./biosharp (China)
Gene Green nucleic acid dye	Tiangen Biochemical Technology (Beijing) Co., Ltd. (China)
isopropanol	Chengdu Kelong Chemicals Co., LTD. (China)

Name of Reagent	Manufacturer
absolute ethyl alcohol	Chengdu Kelong Chemicals Co., LTD. (China)
Chloroform (trichloromethane)	Chengdu Kelong Chemicals Co., LTD. (China)

Table 5. Main reagents for Western blot and immunohistochemistry

Name of Reagent	Manufacturer
BCA protein quantification kit	Beijing Kangwei Century Bioengineering Co., Ltd./CWBIO (China)
RIPA lysate (high potency)	Beijing Solarbio Technology Co., Ltd./Solarbio (China)
Western and IP cell lysate	Shanghai Biyuntian Biotechnology Co., LTD. (China)
PMSF	Beijing Kangwei Century Bioengineering Co., Ltd./CWBIO (China)
PBS powder	Shark Biotechnology Co., Ltd./biosharp (China)
5× protein loading buffer	Beijing Solarbio Technology Co., Ltd./Solarbio (China)
Tween-20	Beijing Solarbio Technology Co., Ltd./Solarbio (China)
PAGE gel rapid preparation kit	Shanghai Yase Biomedical Technology Co., Ltd./Yase Biotech (China)
Tri-color pre-stained protein Marker	Shanghai Yase Biomedical Technology Co., Ltd. (China)
PVDF membrane	Merck/MERCK (USA)
carbinol	Chengdu Kelong Chemicals Co., LTD. (China)
Glycine (Glycine)	Beijing Zhongsheng Ruitai Technology Co., Ltd. (China)
Sodium dodecyl sulfate (SDS)	Beijing Biotopped Technology Co., LTD. (China)
Tris (aminothioglycol)	Beijing Zhongsheng Ruitai Technology Co., Ltd. (China)
dried skimmed milk	Inner Mongolia Yili Industrial Group Co., Ltd. (China)
Stripping Buffer membrane eluent	Beijing Puli Le Gene Co., LTD. (China)
DAB colorimetric kit	Beijing Zhongshan Jinqiao Biotechnology Co., LTD. (China)
Improved sodium citrate antigen repair fluid (50X)	Shanghai Biyuntian Biotechnology Co., LTD. (China)
Ultra-sensitive ECL chemiluminescence is ready to use substrate	Wuhan Bode Biological Engineering Co., LTD. (China)

Table 6. Main instruments and equipment

Instrument name	Model	Manufacturer
Ultra pure water machine	ZWM-UT1-10	Hunan Zhongwo Water Environmental Protection Technology Co., LTD. (China)
Ultra low temperature refrigerator (-80℃)	MDF-86V3401 1	Zhongke Duling Commercial Electrical Appliances Co., Ltd. (China)
Vertical electrophoresis tank	BV-4	Beijing Berlandt Instrument Co., LTD. (China)
Vertical electrophoresis instrument (power supply)	043BR11295	Bio-Rad Corporation (USA)
Single person purification workbench	SW-CJ-1D	Shanghai Huizu Medical Equipment Co., LTD
electronic analytical balance	ME104E	METTLER TOLEDO Company (Switzerland)
electro-heating standing-temperature cultivator	ZXDP-B2160	Shanghai Zhicheng Analytical Instrument Manufacturing Co., LTD. (China)
Use a decolorizing shaker	TS-200A	Haimen Qilin Medical Instrument Factory (China)
Multiple tissue grinders	Tissuelyser-24	Shanghai Jingxin Industrial Development Co., Ltd. (China)
high speed freezing centrifuge	5804R	Eppendorf (Germany)
Isolated water constant temperature incubator	GNP9080	Shanghai Jinghong Experimental Equipment Co., LTD
light microscope	SY100	Nikon Corporation (Japan)
Constant temperature water bath	SY1220	Suzhou Jimei Electronics Co., LTD. (China)
clean bench	OptiClean-130 0	Shanghai Yajing Biotechnology Co., LTD. (China)
LED digital display metal bath host	SCI120-S	SCILOGEX (USA)
Heating magnetic stirrer	MS-01H	Suzhou Jimei Electronics Co., LTD. (China)
Gel analysis system	Tanon5500	Shanghai Tianeng Technology Co., LTD. (China)
PCR thermal cycler	A24812	Thermo Fisher Scientific Company (USA)
qRT-PCR appearance	A28132	Thermo Fisher Scientific Company (USA)
qRT-PCR system	QuantStudio 3	Thermo Fisher Scientific Company (USA)
Fully automatic snowflake ice maker	IMS-150	Xueke Electric Co., LTD. (China)
Fully automatic enzyme marker	RS-232.C	Thermo lab systems company (USA)
micropipet	2.5/10/20/100/ 200/1000 μ L	Eppendorf (Germany)
micro-spectrophotometer	K5500Plus	Beijing Kai 'ao Technology Development Co., LTD. (China)
Microplate centrifuge	CF2800M	Beijing Lanjieke Technology Co., Ltd. (China)
Vortex homogenizer	VM-01U	Suzhou Jimei Electronics Co., LTD. (China)

Instrument name	Model	Manufacturer
Transfuser	221BR35908	Bio-Rad Corporation (USA)
CO2gas incubator	HF90	Thermo lab systems company (USA)
inverted microscope	Axioscope5	Carl Zeiss AG (Germany)
fluorescence microscope	AX10	Carl Zeiss AG (Germany)

1.2. Experimental Methods

1.2.1. Western Preparation Methods of Main Reagents for Blot and Immunohistochemistry

(1) Preparation of electrophoresis fluid

The 10× electrophoresis buffer was prepared according to the formula listed in Table 7. The prepared electrophoresis buffer was placed on a magnetic stirrer and stirred continuously at 800 rpm for 30 minutes until completely dissolved. The buffer was labeled with the preparation date and stored at room temperature.

Table 7. Electrophoresis solution preparation

reagent	Dose 10×
Glycine	28.8 g
Tris Base	6 g
SDS	2 g
hyperpure water	2 L
Glycine	28.8 g
Tris Base	6 g

(2) Transfer membrane solution preparation

Following the composition in Table 8, accurately weigh glycine, Tris base, methanol, and other components. Prepare the transfer membrane working solution using deionized water in a reagent bottle. Place the mixture on a magnetic stirrer and stir at 600 rpm for 20 minutes until fully dissolved. Store the solution in a 4℃ refrigerator for later use.

Table 8. Transmembrane fluid preparation table

reagent	dosage	
	1×	10×
Glycine	14.4 g	144 g
Tris Base	3.03 g	30.3 g
carbinol	200 mL	-
hyperpure water	800 mL	800 mL
Methanol: ultrapure water	1:4	

(3) Preparation of PBS solution and PBST solution

Following the instructions in the reagent manual, slowly pour the entire bag of PBS dry powder along the container wall into a bottle containing 2 L of ultrapure water. Place the bottle on a magnetic stirrer and stir at 500 rpm for 30 minutes until completely dissolved to obtain 0.1M PBS buffer. Store the prepared buffer at room temperature under sealed conditions, clearly labeled with the preparation date.

For subsequent PBST preparation, take 2 L of freshly prepared 0.1 M PBS buffer and add 2 mL Tween-20. Place the mixture on a magnetic stirrer and stir at 600 rpm for 1 hour until thoroughly mixed to obtain a PBST working solution containing 0.1% Tween-20. Store at room temperature under light protection. Before use, ensure the solution is clear with no flocculent floating particles.

(4) 5% skimmed milk preparation

Weigh 0.5 g of skimmed milk powder and dissolve it completely in 10mL of PBST solution to achieve a 5% concentration of the sealing agent. This dosage is suitable for sealing a single PVDF membrane, and the actual amount should be proportionally adjusted according to the number of membranes used. Mix thoroughly using a vortex mixer to ensure no milk particles settle, then store the mixture in a 4°C constant temperature refrigerator for later use.

1.2.2. Real-time Fluorescent Quantitative PCR (qRT-PCR)

1.2.2.1. Total RNA Extraction and Concentration Determination

(1) Sample preparation

Using tweezers, extract 3.2 mm magnetic beads from medical alcohol and wash them three times with double-distilled water to thoroughly remove residual alcohol. Gently absorb any remaining liquid from the beads using qualitative filter paper. Place each 1.5 mL RNase-free EP tube containing 3 beads and 1 mL RNA extraction reagent. Immediately thaw ovarian tissue samples frozen at -80°C on ice before transferring them to the RNase-free EP tubes. Perform mechanical homogenization for 60 seconds using a tissue grinder. If small tissue fragments remain, continue grinding until fully dispersed.

(2) RNA precipitation

After thorough lysis of ovarian tissue or cell samples in the RNA extraction reagent, add 200 μL chloroform to the lysis buffer and manually shake to ensure complete mixing. The mixture is centrifuged at 12,000 r/min for 20 minutes under 4°C conditions, resulting in clear stratification with the upper aqueous phase containing RNA. Carefully transfer 100 μL of the upper aqueous phase to a pre-chilled RNase-free EP tube. Add 200 μL of pre-chilled isopropanol solution at 4°C slowly into the centrifuge tube. Invert the tube 15 times to achieve thorough mixing, then immediately submerge it in an ice bath for 5 minutes. Centrifuge the RNA-containing aqueous phase at 12,000 r/min for 10 minutes under 4°C conditions, revealing a white gel-like RNA precipitate at the bottom. Completely aspirate the supernatant using a 200 μL pipette, then add 1 mL of pre-chilled 75% ethanol in DEPC water and gently aspirate the white flake-like precipitate. Centrifuge at 8,000 r/min for 10 minutes under 4°C conditions. Discard the upper 75% ethanol layer, then centrifuge again at 8,000 r/min for 15 seconds to remove residual ethanol. In a laminar flow unit, invert the EP tube onto sterile filter paper and allow it to air-dry at room temperature for 5 minutes until the remaining ethanol completely evaporates, leaving a translucent RNA precipitate without noticeable ethanol odor. Then 20 μL nuclease-free sterilized water was added to the centrifuge tube and gently blown to promote full RNA dissolution. The dissolved RNA solution should be immediately measured for concentration or transferred to -80°C temperature refrigerator for storage.

(3) RNA concentration determination

The RNA precipitate was resuspended in 20 μL DEPC water. The concentration was measured using a microspectrometer set to RNA detection mode (wavelength 260 nm). Prior to measurement, the instrument was zeroed with 1 μL of enzyme-free water, and this procedure was repeated twice to ensure accuracy. 1 μL samples from each group were analyzed to record the A260/280 absorbance ratio. A ratio between 1.9-2.1 indicated qualified RNA purity suitable for subsequent experiments. Values below 1.8 suggested residual protein in the RNA extract, while ratios above 2.2 indicated organic solvent contamination requiring re-extraction. Finally, the extracted RNA samples were diluted with enzyme-free water to achieve uniform concentration.

1.2.2.2. Reverse transcription

The reverse transcription reaction system was prepared according to the detailed formula in Table 9.

Table 9. Reverse transcription reaction system

Reagent	Volume (μL)
RNA Template	2
RT Primer	1
5×RT Buffer	2
RTase Mix	2
RNase-free Water	3
Total volume	10

In the prepared reverse transcription reaction system, gently pipette 10 times to ensure thorough mixing of all reagents and eliminate air bubbles. Place the Erlenmeyer flask in a centrifuge for 5 seconds, then transfer the sample to a PCR thermal cycler for reverse transcription. After completion, add an appropriate amount of enzyme-free

water based on the cDNA extraction quantity, and store at 4°C. For long-term preservation, transfer to -20°C.

1.2.2.3 Quantitative PCR detection

(1) Primer dissolution and preparation

Place the dried primer powder tube in a microcentrifuge and centrifuge at 12,000 rpm, 15 minutes and under 4°C conditions to ensure the powder settles at the bottom. Slowly open the lid and add non-nucleic acid enzyme-free water according to the volume indicated on the tube. Vortex mix for 10 seconds, then briefly centrifuge again to remove air bubbles. Add 10 μL of the synthesized upstream primer, 10 μL of the downstream primer, and 180 μL of non-nucleic acid enzyme-free water. Vortex mix for 30 seconds to ensure thorough mixing, yielding a 200 μL primer mixture. Store the mixture in a 4°C refrigerator.

(2) Preparation of reaction system

Prepare a 10μL reaction mixture by adding 5 μL SYBR Green fluorescent dye pre-mix, 1 μL reverse transcription product cDNA, 1μL specific primer pair, and 3μL nuclease-free ultrapure water per well. Add all components sequentially to the PCR 96-well plate, followed by centrifugation and mixing.

(3) Computer test

First, launch the Quant Studio 3 real-time fluorescence quantitative PCR instrument. Create a new project on the main interface and configure experimental parameters. Select the SYBR Green fluorescent dye method for the detection system, and use the $2-\Delta\Delta$Ct relative quantification analysis method for data processing. Set the program parameters as follows: perform 95°C pre-denaturation for 10 minutes initially, followed by 40 standard cycles (each cycle including 95°C denaturation 10s, 60°C annealing 30 s, 95°C. extension 15s, and 60°C amplification 60 s). Finally, conduct

melting curve analysis with 95°C denaturation for 15 s. After completing parameter settings, arrange the prepared samples in the sample rack according to the preset sequence, and execute the program instructions after confirming no errors.

1.2.2.4 Primer Sequences

Table 10. Primer sequences

GENE	Sequence (5′-3′, 3’-5’)
mus BAX	Forward:TGCAGAGGATGATTGCTGAC Reverse:GATCAGCTCGGGCACTTTAG
mus Bcl-2	Forward:GGTGGTGGAGGAACTCTTCA Reverse:ATGCCGGTTCAGGTACTCAG
mus Caspase-3	Forward:TGACTGGAAAGCCGAAACTC Reverse:GCAAGCCATCTCCTCATCA
mus HK2	Forward:CGTGGTAAATGACACAGTTG Reverse:AGTTCCACATTACGCATCTC
mus LDHA	Forward:ACTGTGTAACTGCGAACTCC Reverse:GGGAATGATGAACTTGAAGA
Mus GAPDH	Forward:ATTGTCAGCAATGCATCCTG Reverse:ATGGACTGTGGTCATGAGCC
Human PI3K	Forward:TCTGTGTGGACAGCGTGTAA Reverse:TCTTGGTCTCCAGCATCTTG
Human AKT	Forward:CCTCCTCAAGAATGATGGCA Reverse:CGTGGTCCTGGTTGTAGAAG
Human HIF-1α	Forward:GAAAGCGCAAGTCCTCAAAG Reverse:TGGGTAGGAGATGGAGATGC
Human HK2	Forward: CGAGAGCATCCTCCTCAAGTG Reverse:AGCCACAGGTCATCATAGTTCC
Human PKM2	Forward: TGGGAGAGAAGGGAAAGAACATC Reverse:GCACCGTCCAATCATCATCTTC
Human LDHA	Forward:ATGAGTTGGACTGTGCCTGTTGTG Reverse: GTGAAGAGCCAGGTGCCGTTG

Human GAPDH	Forward:GAGTCCACTGGCGTCTTCAC Reverse:GAGGCATTGCTGATGATCTTGAG

1.2.3. Immunoblotting (Western Blot)

1.2.3.1. Total Protein Extraction and Determination

(1) Extraction of ovarian tissue proteins

The tissue grinding blocks from the grinder were pre-cooled in a -20°C freezer for 30 minutes. Using forceps, 3.2 mm magnetic beads were extracted from medical alcohol and thoroughly rinsed with double-distilled water to remove residual alcohol. The surface liquid was gently absorbed using qualitative filter paper. Each 1.5 mL EP centrifuge tube contained 2-3 magnetic beads mixed with 100 μL protein lysis buffer (RIPA: PMSF = 100:1, freshly prepared). Immediately after retrieving ovarian tissue samples from the -80°C freezer, they were transferred to pre-cooled 1.5 mL EP tubes. Mechanical homogenization was performed using a tissue grinder with a 60-second single-cycle program, repeated 2-3 times. During homogenization, the samples were closely monitored: if unbroken tissue clumps remained, the grinding time was extended until complete homogenization; if a uniform paste without white fascicular material appeared, the EP tubes were rapidly chilled on ice for 30 minutes of protein lysis. After complete lysis, the protein samples were transferred to a high-speed centrifuge pre-cooled to 4°C , centrifuged at 12,000 rpm, 20 minutes. The supernatant was then transferred to fresh EP tubes.

(2) Determination of protein concentration

Prepare BCA working solution (A: B = 50:1) before determination, and add it to the 96-well plate according to Table 11.

Table 11. Protein concentration determination reaction system

reagent （μL）	1	2	3	4	5	6	Sample to be tested
fluid	200	200	200	200	200	200	200
hyperpure water	20	19	18	17	16	15	19

reagent （μL）	1	2	3	4	5	6	Sample to be tested
2 mg/mL standard	0	1	2	3	4	5	-
Sample to be tested	-	-	-	-	-	-	1

After adding 200μL working solution to each reaction well, incubate in a 37°C constant temperature incubator for 30 minutes. Upon reaction termination, set the microplate reader to detect at 450 nm and sequentially measure the OD values of each reaction well. Select wells 1-6 as standard reaction wells, perform linear regression analysis using the standard concentration (x-axis) and corresponding OD values (y-axis), derive the standard curve equation, and calculate the coefficient of determination (R^2). When R^2 value is ≥0.990, it is deemed suitable for calculating protein concentrations in each sample group. The specific method involves deriving and calculating protein concentration values for each sample based on the standard curve equation.

1.2.3.2. Protein denaturation

The samples were first normalized for concentration using double-distilled water. Protein solutions were mixed with 5× Loading Buffer at a 4:1 volume ratio, thoroughly mixed with a pipette, and then heated in a 100°C metal bath for 8-10 minutes to denature proteins. The treated protein samples underwent rapid cooling in an ice bath immediately after processing, followed by prompt transfer to -20°C freezer for subsequent storage.

1.2.3.3. SDS-PAGE Gel Electrophoresis

(1) Gel preparation

Prior to gel preparation, the glass plate must undergo rigorous cleaning. Begin with a preliminary wash using neutral detergent, followed by initial rinsing with tap water, final rinsing with ultrapure water to ensure no residual gel remains. After cleaning, align thin and thick plates in a closed configuration and install them on the gel

preparation rack to form a sealed laminated structure. Inject ultrapure water for airtightness verification, then observe the liquid level changes after 8-10 minutes of static observation. If the liquid level remains stable during this period, discard any residual liquid and thoroughly absorb any remaining moisture using qualitative filter paper. Glass plate systems passing leak detection can be configured with separation gel and concentrated gel according to the formulation system of the rapid gel preparation kit.

First, inject the separation gel (lower layer). Pour the separation gel solution along the inner surface of the glass plate while strictly controlling the injection speed to minimize bubble formation. Apply approximately 4-4.5 mL of gel on one side of the glass plate. Immediately after injection, perform alcohol sealing to ensure surface alignment through hydraulic pressure, then let it stand at room temperature for 25 minutes. When clear refracted lines form at the liquid-gel interface, confirm complete solidification. Remove the upper layer of alcohol and thoroughly absorb residual liquid using qualitative filter paper. Next, prepare and inject the concentration gel (upper layer). Insert the concentration gel into a cleaned hole comb immediately after pouring, maintaining vertical insertion and checking for residual bubbles in comb teeth gaps. Allow it to stand at room temperature for 25 minutes to achieve complete solidification.

(2) Sample loading and electrophoresis

Load the solidified gel into the electrophoresis apparatus and fill its inner tank with electrophoresis buffer. Gently pinch the comb and pull it upward steadily. Add Marker to each well (2.5 μL) followed by denatured protein samples (minimum 20μg per well), then dispense electrophoresis buffer into the outer tank. Activate the power supply, initially setting the constant voltage to 60V to initiate electrophoresis. Continuously monitor bromophenol blue indicator migration during the process. When the bromophenol blue has fully migrated into the gel, increase the voltage to 120V to accelerate separation until it reaches the lower edge of the gel. Immediately shut off the power to terminate electrophoresis.

1.2.3.4. Transmembrane

First, immerse the thick filter paper used for membrane transfer into a pre-cooled transfer solution. After removing it, place it on a foam plate and roll it flat using a

small roller. Next, gently pry open the fixed glass plate assembly with a pry bar to avoid damaging the gel. Transfer the intact gel onto the foam plate and precisely align with the pre-stained protein molecular weight bands. Cut the target protein-containing gel section and transfer it gently onto the prepared thick filter paper. Trim the PVDF membrane to the required size and activate it by immersing it in methanol. Place the PVDF membrane over the cut gel section and roll it slowly with a roller to eliminate air bubbles between the gel and membrane. Cover the PVDF membrane with another thick filter paper and roll it flat using the same small roller. Flip the entire assembly horizontally into the transfer chamber, carefully roll again to remove air bubbles, then insert an ice pack of appropriate size into the chamber. Cover the chamber with a lid and transfer the membrane for 45 minutes at a constant voltage of 13V in a low-temperature environment.

1.2.3.5. Closure

After completing the operation, confirm that the Marker has been fully transferred to the PVDF membrane surface to verify the successful transfer process. Mark experimental information on the membrane edge using a ballpoint pen, then immerse the membrane in pre-prepared milk blocking solution and incubate it on a horizontal shaker at room temperature for 2 hours.

1.2.3.6 Incubation of Antibodies

(1) Incubation of primary antibody

After the membrane is sealed, it undergoes five PBS washes for 5 minutes each. Following the antibody product manual instructions, the target protein antibody is diluted in PBS. The qualified membranes are placed in plastic sealing sleeves, trimmed into rectangular shapes, and sealed with a heat-sealing machine on three sides. After adding the diluted antibody solution to the bag and completely removing air bubbles, the fourth side is sealed. The sealed antibody incubation bag is then laid flat on a horizontal shaker, and incubated at 4°C for 12-16 hours to ensure full binding between the antibodies and target proteins.

(2) Incubation of secondary antibody

After completing the primary antibody incubation, the primary antibody solution was collected and the PVDF membrane was washed five times with PBS buffer, each wash lasting 5 minutes. The secondary antibody was diluted to a working concentration of 1:5000 using PBS buffer. The washed membrane was then immersed in the secondary antibody solution, incubated at room temperature on a horizontal shaker for 2 hours.

1.2.3.7. Development

After completing the secondary antibody incubation, collect the secondary antibody and perform five PBS wash cycles on the PVDF membrane, each lasting 5 minutes. Pre-run the developing instrument for preliminary cooling. Mix reagent A and reagent B in a light-shielding reaction chamber at a 1:1 volume ratio, mix thoroughly by horizontal shaking, and use immediately within 30 minutes. If the reaction time exceeds this limit, re-prep the mixture. Gently blot residual buffer from the membrane surface with qualitative filter paper, then transfer it to a reaction chamber containing freshly prepared developing solution. Position the membrane on the dark chamber platform of the developing instrument, ensuring full coverage of the detection area. After closing the dark chamber door, activate the imaging program to capture chemiluminescence images through auto-exposure mode. Save the raw data and perform quantitative analysis using ImageJ software.

1.2.4. Immunohistochemistry (IHC)

Dewaxing

Refer to Chapter Ⅱ 1.2.8. for dewaxing.

Antigen repair

The glass slides were first washed with PBS buffer using a horizontal decolorization shaker, followed by three 5-minute rinses. The slides were then immersed in freshly prepared 3% H_2O_2-methanol solution 30 minutes, eliminate endogenous peroxidase activity. After three additional PBS rinses, 800 mL of antigen retrieval solution was placed in a heat-resistant container, covered with aluminum foil, and preheated at 90% power for 10 minutes in a microwave oven. The rinsed slides were fully submerged in boiling antigen retrieval solution and heated at 90% power for 3 minutes. The heated slides were then left at room temperature for 5 minutes before repeating this process three times. Following the final retrieval, the aluminum foil was

removed and the slides cooled to room temperature. The cooled slides underwent three PBS rinses (5 minutes each) before being immersed in freshly prepared 1% Triton X-100-PBS for 30 minutes at room temperature to enhance cell membrane permeability. Finally, the slides were rinsed three more times (5 minutes each) using PBS.

Seal off

Using a filter paper, blot the residual buffer from the edges of the dried glass slide. With an immunohistochemistry-specific pen, outline a water barrier around the tissue periphery, maintaining a 1-2 mm safety margin between the marked area and the tissue. After completing the marking, apply 5% BSA blocking solution to the tissue surface to ensure uniform coverage. Allow the specimen to incubate at room temperature for 45 minutes. Maintain the slide horizontally throughout this process to prevent leakage or drying of the blocking solution.

Incubation antibody

(1) Incubation of primary antibody

After the blocking reaction with bovine serum albumin (BSA) is complete, gently shake the slides to remove residual blocking buffer. Dilute the primary antibody to working concentration using PBS buffer according to the manufacturer's recommended ratio. Add the antibody dropwise into the blocking ring to ensure complete specimen coverage. Place the prepared slides in a humid incubator and incubate at 4°C for over 12 hours. Maintain horizontal positioning during incubation to ensure uniform antibody distribution.

(2) Incubation of secondary antibody

The glass slides were placed on a horizontal decolorization shaker and rinsed three times with PBS buffer, each rinse lasting 5 minutes. After gently blotting residual liquid from the edges of the slides using qualitative filter paper, the secondary antibody was diluted concentration of 1:200 in PBS buffer according to the recommended ratio specified in the kit instructions. The antibody solution was carefully dispensed into the water-blocking ring to ensure complete coverage of the specimen surface. Following a 45-minute room temperature incubation, the slides were transferred to a 37°C constant temperature incubator for an additional 45-minute static incubation period.

(3) Incubation of three anti-bleed antibodies

Place the glass slide on a horizontal decolorization shaker. Perform three cycles of PBS buffer rinsing for 5 minutes each. Gently blot residual buffer from the edges using filter paper. Dilute the tertiary antibody to a concentration of 1:200 using PBS buffer according to the recommended ratio in the tertiary antibody manual. Add the diluted antibody solution into the water-blocking ring to ensure complete coverage of the specimen surface, then transfer it to a 37°C incubator for 45 minutes of continued incubation.

Coloration

Place the slide on a horizontal decolorization shaker and wash three times with PBS for 5 minutes each. Prepare the chromogenic working solution in a light-shielding environment. Drop the chromogenic solution into the water-blocking ring to ensure complete coverage of the specimen surface, then observe the chromogenic reaction in real-time under an optical microscope. When brown coloration appears in the target tissue, immediately terminate the reaction with PBS buffer. Perform three additional PBS rinses for 5 minutes each. Subsequently, perform hematoxylin re staining by immersing the slide holder in hematoxylin stain for 5 minutes. After rinsing off surface color with water, place it in a 1% hydrochloric acid alcohol solution about 3-5 seconds of differentiation. Finally, soak in running water for 20 minutes to complete the counterstaining process.

Deprivation of body fluids

The tissue sections were processed using the gradient alcohol dehydration method described in Chapter Ⅱ Section 1.2.8. After each treatment stage, the previous solution must be thoroughly drained before transferring to the next reagent chamber to prevent cross-contamination. Following completion of gradient dehydration and clearing to meet mounting standards, the sections were mounted with neutral resin mount medium. Upon complete resin curing, microscopic observation was performed using an optical microscope for image acquisition.

1.2.5. NAD^+ /NADH Content Test Kit (colorimetric method)

The NAD^+ detection kit manufactured by Nanjing Institute of Biological Engineering was employed for testing. The solution was prepared using a 1:5-10 ratio of tissue weight (g) to acidic extraction volume (mL), requiring immediate

preparation. Tissue samples were homogenized in an ice bath, transferred to centrifuge tubes, and heated in a boiling water bath, 5 minutes to terminate enzymatic reactions. After cooling to ice temperature, the samples underwent 10 minutes, 10,000 rpm for 4 °C cycles. The supernatant was transferred to fresh centrifuge tubes, and an equal volume of alkaline extraction buffer was added for neutralization. Following thorough mixing, the mixture was centrifuged again under identical conditions for 10 minutes. The collected supernatants were divided into two portions: one portion was used for protein concentration determination following Method 2.3.1 in Section 2.3.1, while the other portion was processed according to the kit's instructions for subsequent detection.

After thorough vortex mixing, use a pipette to precisely transfer 200μL of the reaction mixture into each well of the 96-well plate. Set the detection wavelength at 530 nm on the microplate reader and measure the absorbance values, recording the OD values for each well. The NAD^+ content in tissues is calculated using the formula:

NAD^+ Content (nmol/g tissue) = (A measured-A control-0.099) × 72.2 ÷ Sample Mass (g)

1.3. Statistical Analysis

All data were repeated at least three times. Shapiro-Wilk tests were first conducted to assess normality. When data met normality assumptions, one-way ANOVA was used for inter-group analysis of normal distribution data, with Tukey's tests for multiple comparisons. Results were presented as mean ± standard deviation (Mean±SD). For non-normal distribution data, Kruskal-Wallis H tests were employed for inter-group comparisons, with results expressed as median and interquartile range. All statistical analyses were performed using GraphPad Prism 9.0 software, with statistical significance defined as $P < 0.05$.

2. Results

2.1. Effect of NMN Supplementation on Local NAD^+ Levels in the Mouse Ovary

To evaluate the effects of IR on ovarian metabolic homeostasis, we employed a colorimetric method (enzyme cycle assay) to measure NAD^+ levels in ovarian tissues from control, 5Gy, 5Gy+NMN, and NMN groups at the end of the experiment. Results clearly indicated that NAD^+ levels in the control group remained within normal physiological ranges. However, radiation-exposed mice showed significant decreases in ovarian NAD^+ levels, suggesting severe disruption of local redox metabolism ($P < 0.05$). The supplementation of NMN reversed this phenomenon. Compared to the 5Gy group, the 5Gy+NMN group demonstrated a marked increase in ovarian NAD^+ levels ($P < 0.05$), approaching control group levels with statistically significant recovery amplitude, indicating NMN's notable restorative effect on radiation-induced NAD^+ depletion. Radiation significantly depletes ovarian NAD^+, while NMN supplementation can alter local NAD^+ levels and restore ovarian metabolic homeostasis, providing mechanistic evidence for its radiation protection effects. Additionally, NMN supplementation in normal mice significantly elevated local ovarian NAD^+ levels.

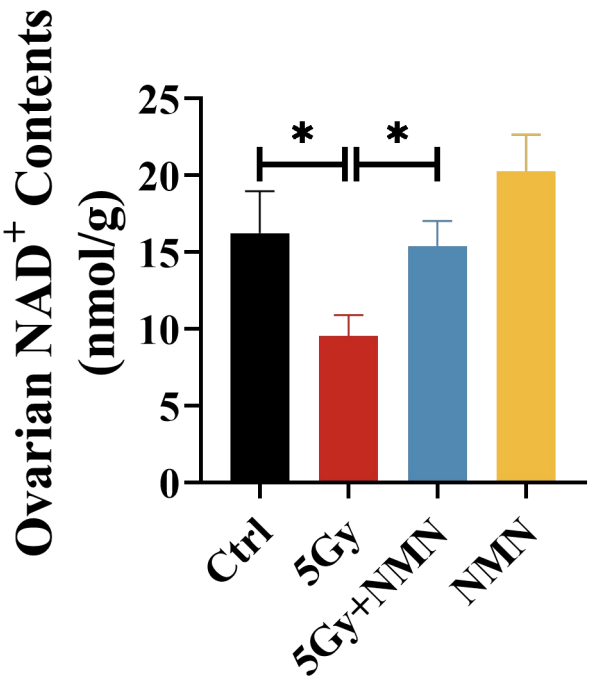

Figure 8. Effects of NMN supplementation on NAD^+ levels in ovaries of radiation-exposed mice

The figure displays NAD^+ concentrations in ovaries from different mouse groups (control, radiation, radiation+NMN, NMN). Compared with the control group, radiation significantly reduced NAD^+ levels, while NMN supplementation effectively restored NAD^+ concentrations. n=5, *P <0.05

2.2. Effect of NMN on Local Oxidative Stress in Ovary Caused by IR

To examine the role of NMN on oxidative stress in radiation-induced ovarian injury, we assessed the antioxidant enzyme superoxide dismutase (SOD) and the oxidative stress marker malondialdehyde (MDA, Figure 9). Western blot analysis demonstrated that in the 5Gy irradiation group, SOD expression was significantly reduced ($P < 0.01$), whereas protein MDA adducts, indicative of lipid peroxidation, were markedly elevated compared with the control group ($P < 0.001$). NMN supplementation effectively reversed these alterations, restoring SOD expression and markedly reducing protein-MDA adduct accumulation ($P < 0.001$). Notably, the NMN-only group maintain levels comparable to the control group, indicating that NMN preserves local redox homeostasis in ovarian tissue without perturbing basal oxidative parameters.

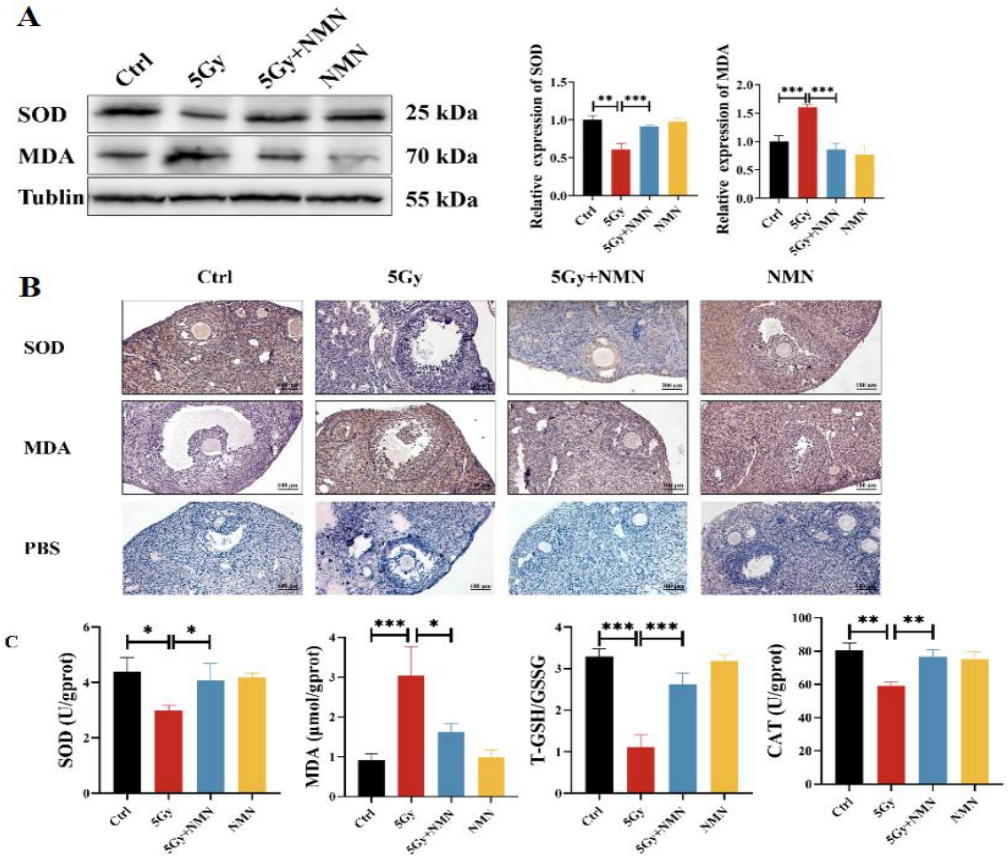

Figure 9. NMN alleviates radiation induced oxidative stress in mouse ovaries

(A) Protein expression levels of antioxidant enzyme SOD and oxidative stress-related protein MDA complex were detected in ovarian tissues of mice across different groups. The 5Gy group showed decreased SOD levels and increased MDA expression, while NMN intervention restored SOD levels and reduced MDA expression.

(B) Immunohistochemical analysis of ovarian tissue sections from each group showed significantly reduced SOD staining and increased MDA levels in the 5Gy treatment group, with NMN intervention reversing these changes. The PBS control group served as a negative reference. Scale bar: 100 μm.

(C) The kit-based colorimetric method was used to detect oxidative stress-related enzyme activities in the ovaries. Radiation significantly reduced SOD and CAT activity, lowered the T-GSH/GSSG ratio, and increased MDA levels. NMN intervention improved antioxidant enzyme activity, restored glutathione's redox balance, and decreased MDA accumulation.

n=5; data are expressed as mean ± SEM; *P <0.05, **P <0.01, ***P <0.001.

2.3. Effect of NMN on Local Glycolysis Changes in Ovaries Caused by IR

To determine whether NMN supplementation ameliorates radiation-induced disturbances in ovarian glycolysis, we evaluated four aspects: (i) mRNA and protein expression of key glycolytic enzymes (HK2, PKM2, and LDHA), (ii) histological distribution (Figure 10), and (iii) the metabolic end products pyruvate and lactate

(Figure 11). qPCR analysis revealed that in the 5Gy irradiation group, mRNA levels of HK2, PKM2, and LDHA were significantly reduced compared with the control group. NMN intervention restored their expression to levels comparable with controls. Similarly, the NMN-only group in normal mice exhibited expression patterns indistinguishable from the control group (Figure 10A). Western blotting confirmed these findings, showing markedly decreased protein expression of HK2, PKM2, and LDHA in the 5Gy group, which was significantly reversed following NMN treatment (Figure 10B-C). Immunohistochemistry further demonstrated the tissue distribution of these enzymes (Figure 10D). In control ovaries, both follicular granulosa cells and interstitial cells displayed strong positive staining for HK2, PKM2, and LDHA. Irradiated ovaries showed markedly reduced staining intensity, indicative of impaired glycolytic activity. NMN treatment substantially restored staining intensity and distribution, providing histological evidence of metabolic repair. Colorimetric assays of glycolytic end products revealed that pyruvate levels were significantly elevated in the 5Gy group relative to controls, whereas lactate levels were markedly reduced (Figure 11), indicating impaired conversion of pyruvate to lactate. Although the absolute pyruvate concentration was not substantially higher than in other groups, its relative accumulation reflected a metabolic blockade.

Collectively, these results demonstrate that radiation disrupts ovarian glycolysis and compromises oocyte energy supply by suppressing key glycolytic enzymes. NMN supplementation, by elevating tissue NAD^+ levels, restores HK2, PKM2, and LDHA expression and activity, thereby promoting lactate production and energy generation. This multifaceted mechanism highlights NMN′s capacity to repair radiation-induced glycolytic dysfunction in ovarian tissue.

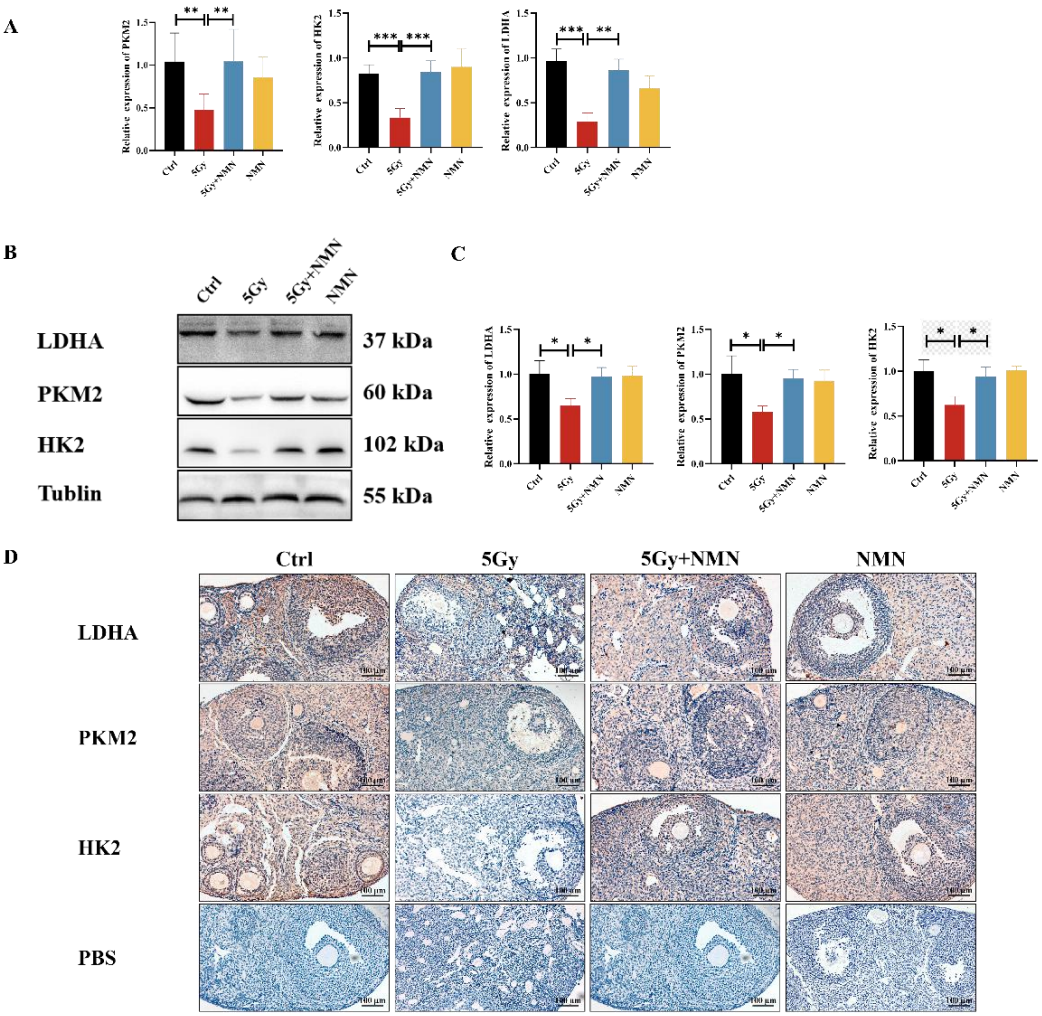

Figure 10. Glycolytic metabolism of NMN in radiation-damaged ovaries

(A) PCR was used to determine the mRNA expression levels of key glycolysis enzymes HK, PK and LDHA in ovarian tissue.

(B, C) Western blot quantitative analysis of the expression levels of key glycolysis enzymes HK2, PKM2 and LDHA proteins.

(D) IHC analysis of HK2, PKM2, and LDHA expression in ovarian tissues from different groups. The distribution patterns in follicular and interstitial cells were visualized (scale bar = 100 μm). n=5. Data are presented as mean ± ± standard deviation. Significant differences are marked: *P <0.05, **P <0.01, ***P <0.001.

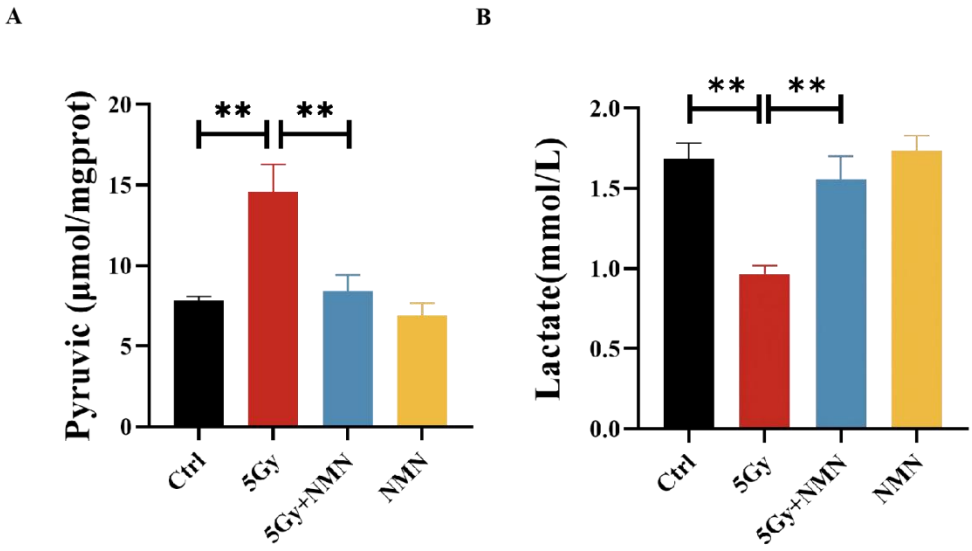

Figure 11. Effects of NMN on pyruvate and lactate in ovarian tissue after radiation damage
(A) The expression of pyruvate and lactate were determined by colorimetric method. Compared with Ctrl group and 5Gy+NMN group, pyruvate increased in 5Gy group
(B) The lactic acid level decreased in the 5Gy group compared with the Ctrl group and 5Gy+NMN group.
n=5; data are expressed as mean ± standard deviation. **P <0.01.

2.4. Effects of NMN on Apoptosis of Ovarian Tissue Caused by IR

We examined apoptosis-related molecules, including Bax, Bcl-2, and Caspase-3, at the transcriptional, translational, and histological levels (Figure 12). qPCR analysis revealed that in the 5Gy group, mRNA expression of Bax and Caspase-3 was significantly upregulated, whereas Bcl-2 expression was markedly downregulated compared with the control group. NMN supplementation effectively reversed these alterations, restoring all three factors to near-control levels. The NMN-only group displayed expression patterns similar to those of controls (Figure 12A). Western blot analysis confirmed these findings: irradiated ovarian tissues exhibited enhanced expression of Bax, Caspase-3, and Cleaved Caspase-3, accompanied by a reduction in Bcl-2 protein levels. In contrast, NMN treatment markedly attenuated pro-apoptotic protein expression while restoring Bcl-2 levels (Figure 12B). IHC analysis further validated these results (Figure 12C). Radiation exposure led to increased Bax and Caspase-3 positive staining and reduced Bcl-2 staining in ovarian follicles. NMN

administration significantly diminished Bax and Caspase-3 signals while enhancing Bcl-2 positivity, closely paralleling the Western blot results. The PBS control group showed no nonspecific staining.

In summary, radiation activated pro-apoptotic pathways and suppressed anti-apoptotic signals in ovarian tissue, thereby exacerbating follicular apoptosis. NMN intervention significantly mitigated these effects, inhibiting radiation-induced apoptosis and providing mechanistic evidence for its protective role in ovarian function.

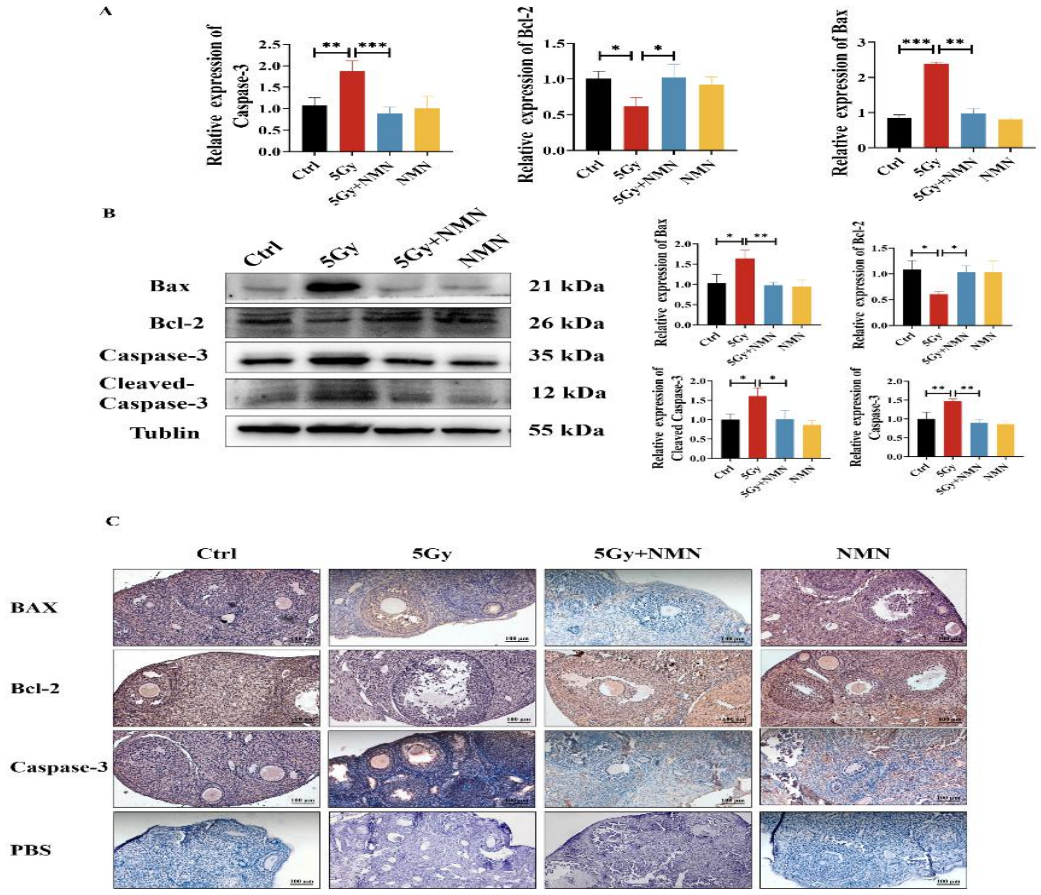

Figure 12. NMN inhibits radiation induced apoptosis of mouse ovarian cells

(A) PCR detected the expression of mRNA of apoptosis-related factors. Radiation (5Gy) significantly increased the expression of Bax and Caspase-3, and decreased the level of Bcl-2; however, NMN treatment reversed these changes.
(B) Western blot analysis was performed to detect the expression of Bax, Bcl-2, Caspase-3, and Cleaved-Caspase-3 in mouse ovaries. In the radiation group, Bax, Caspase-3, and Cleaved-Caspase-3 showed increased expression while Bcl-2 expression decreased. These trends were significantly improved after NMN supplementation. β-tubulin was used as the internal control. The figure displays representative bands and grayscale quantification results.

(C) IHC analysis was performed to evaluate the localization and expression of apoptosis-related factors in ovarian tissue sections from different groups. In the radiation group, Bax and caspase-3 staining showed increased intensity while Bcl-2 staining decreased. After NMN treatment, the staining intensity recovered to levels comparable to the control group. The PBS group served as a negative control.
Scale = 100 μm. n=5; Data are expressed as mean ± SEM; *P <0.05, **P <0.01, ***P <0.001.

3. Discussion

This study utilizes an ionizing radiation-induced ovarian injury model in mice to systematically elucidate the mechanisms by which radiation disrupts ovarian energy metabolism homeostasis and functional integrity. For the first time, we demonstrated the metabolic protective role of NMN. Our findings reveal that radiation-induced NAD^+ depletion significantly elevates oxidative stress levels while suppressing the expression and activity of key glycolytic enzymes, leading to insufficient lactate and ATP production that triggers energy crisis in granulosa cells. The combined effects of energy metabolism disorders and oxidative damage induce ovarian granulosa cell apoptosis and follicular atresia associated with functional impairment. Our conclusions suggest that radiation-induced ovarian dysfunction occurs through a cascade reaction involving oxidative stress-energy metabolism disorder and mitochondria-mediated apoptosis.

Previous studies have extensively demonstrated that IR generates significant ROS through water molecule ionization, leading to DNA damage, lipid peroxidation, and protein oxidative modifications[145]. Ovarian tissue is particularly susceptible to oxidative stress, where excessive ROS disrupts the microenvironment of granulosa cells, inducing follicular atresia and oocyte apoptosis[146], [147]. Furthermore, the overactivation of PARP1 rapidly depletes NAD^+, creating a cellular energy crisis that closely aligns with the NAD^+ depletion observed in our experiments[148], [149].

In terms of energy metabolism, this study observed that radiation significantly reduced the expression levels of HK2, PKM2, and LDHA, accompanied by decreased lactate production. These findings suggest that radiation suppresses glycolytic flux,

exacerbating energy deficiency in ovarian cells. Previous research has indicated that glycolysis not only serves as the primary energy supply pathway but also provides key metabolic substrates (such as pyruvate and lactate) for granulosa cells to supply oocytes[150]. Therefore, glycolytic dysfunction directly impacts follicular development and oocyte quality, ultimately compromising reproductive function.

More importantly, this study found that supplementation with NAD^+ precursor NMN significantly alleviated the aforementioned damage. NMN can enhance cellular NAD^+ levels, activate SIRT1/SIRT3, improve mitochondrial function, and boost antioxidant defenses[151], [152]. In ovarian tissue, NMN supplementation markedly restored expression of key glycolytic enzymes, improved lactate production, and reduced apoptosis levels. This suggests NMN exerts its effects through dual mechanisms: rebuilding NAD^+ dependent energy metabolism networks while enhancing mitochondrial function and antioxidant capacity, thereby breaking the vicious cycle from oxidative stress energy to metabolism disorder to mitochondrial apoptosis.

In conclusion, our study has elucidated the metabolic mechanisms by which ionizing radiation damages ovarian function, while demonstrating for the first time that NMN shows potential in repairing radiation-induced glycolytic dysfunction in ovaries. This discovery not only deepens our understanding of the pathological mechanisms underlying ovarian radiation damage but also provides experimental evidence for targeted NAD^+ metabolic interventions. Future research could further integrate multi-omics technologies such as transcriptomics, metabolomics, spatial omics, and single-cell sequencing to comprehensively analyze the dynamic role of NAD^+ metabolic remodeling in radiation-induced ovarian damage and repair processes, thereby offering new protective and therapeutic strategies for female reproductive health.

4. Summary

This study demonstrates that IR impairs ovarian function primarily through a cascade involving oxidative stress, metabolic disruption, and apoptosis. Radiation induces excessive ROS generation and NAD^+ depletion, leading to mitochondrial membrane potential loss and dysfunction of the electron transport chain. Concurrently, radiation downregulates key glycolytic enzymes, suppressing lactate and ATP production and thereby aggravating cellular energy deficits. Under these conditions of redox imbalance and metabolic insufficiency, mitochondria release cytochrome c and activate the caspase cascade, resulting in granulosa cell apoptosis and follicular atresia. Collectively, these findings suggest that radiation-induced ovarian injury is mediated through an oxidative stress, energy metabolism disorder, mitochondrial apoptosis' cascade, providing mechanistic insight into ovarian dysfunction after irradiation and a rationale for targeted metabolic interventions.

Chapter Ⅳ. Metabolomic Analysis of NMN Mediated Restoration of Radiation Induced Ovarian Dysfunction

The ovaries are among the most radiosensitive organs of the female reproductive system, with their susceptibility to radiotherapy, chemotherapy, and environmental irradiation being well documented[153], [154]. Exposure to cesium-137 γ rays generates reactive oxygen species (ROS) via water radiolysis, leading to DNA double-strand breaks, lipid peroxidation, and protein oxidation that severely damage ovarian cells, particularly granulosa cells. Under oxidative stress, intracellular NAD^+ levels decline sharply, mitochondrial membrane potential (Δψm) decreases, and electron transport chain dysfunction accelerates apoptosis and follicular atresia[155]. In parallel, IR downregulates the expression of HK2, PKM2, LDHA, resulting in Ⅳ impaired lactate and ATP production. This energy deficit in granulosa cells further exacerbates mitochondrial-mediated apoptosis[156]. Together, these molecular and metabolic perturbations culminate in diminished ovarian reserve and premature ovarian insufficiency.

In recent years, metabolic interventions have emerged as promising strategies for the prevention of ovarian dysfunction. NMN effectively elevates intracellular NAD^+ , activates the SIRT1/SIRT3 signaling axis, enhances mitochondrial function, and reinforces antioxidant defenses. It has demonstrated protective effects across multiple models of tissue injury and aging[136], [157], [158]. Notably, NMN has been shown to improve follicular development and hormone secretion in models of premature ovarian failure and granulosa cell injury, suggesting that its protective mechanisms may involve the regulation of energy metabolism and oxidative stress[124]. Based on these findings, we propose that the pathological cascade of radiation-induced ovarian

dysfunction can be conceptualized as ‘oxidative stress, energy metabolism disorder, mitochondrial apoptosis, ovarian dysfunction.’ By replenishing NAD^+ , restoring glycolytic flux, and improving mitochondrial function, NMN may interrupt this vicious cycle and preserve ovarian function.

To systematically elucidate the molecular mechanisms underlying NMN’s protective actions, the present study employs transcriptome sequencing of ovarian tissue in an animal model. The analysis focuses on: (i) core glycolysis/glucose metabolism genes and their upstream regulatory pathways (PI3K/AKT/HIF-1α, mTOR, AMPK, FOXO); (ii) oxidative stress and antioxidant response pathways (Nrf2/Keap1, SOD family, GPX, CAT, HO-1) in conjunction with lipid peroxidation biomarkers such as MDA. By integrating phenotypic assessment of radiation damage with transcriptomic network analysis, we aim to construct a mechanistic framework linking radiation-induced injury, molecular targets, and NMN mediated activity. This approach is expected to identify critical therapeutic pathways and potential intervention targets, thereby providing experimental evidence to support the development of novel strategies for the management and clinical translation of ovarian radiation injury.

1. Materials and Methods

1.1. Experimental Materials

The animal experiment section is partially referenced from the animal experiment section of Chapter II-III. After obtaining ovarian tissue specimens, we commissioned Beijing Novo gene Technology Co., Ltd. to complete the ovarian tissue transcriptome sequencing.

1.2. Experimental Methods

1.2.1. Ovarian Transcriptome Analysis in Mice (RNA-seq)

To investigate the molecular effects of ionizing radiation on ovarian tissues, we performed transcriptome sequencing of mouse ovaries. Total RNA was extracted using standardized protocols, and its quality and integrity were assessed by spectrophotometry and Agilent Bioanalyzer, ensuring purity (A260/A280 $\approx$ 1.8–2.1) and integrity (RIN $\geq$ 7.0). High-quality RNA samples were used for strand-specific library construction, followed by paired-end sequencing (150 bp) on the Illumina platform to generate comprehensive transcriptome profiles. After stringent quality control and data filtering, differential expression analysis was performed with the DESeq2 package, applying the thresholds of |log2 fold change| $\geq$ 1 and false discovery rate (FDR) < 0.05. Differentially expressed genes (DEGs) were further subjected to Kyoto Encyclopedia of Genes and Genomes (KEGG) pathway enrichment using the cluster Profiler package, with adjusted $P < 0.05$ considered significant. This strategy enabled the identification of critical metabolic and signaling pathways associated with radiation exposure and NMN intervention, thereby providing a molecular basis for downstream mechanistic exploration.

1.3. Statistical Analysis

Shapiro-Wilk tests were first conducted to assess normality. For normally distributed data, one-way ANOVA was employed for inter-group comparisons, with Tukey's tests for multiple comparisons. Results were presented as mean $\pm$ standard deviation (M $\pm$ SD). For non-normal distributions, Kruskal-Wallis H tests were used for inter-group comparisons, with results expressed as median and interquartile range (IQR). All statistical analyses were performed using GraphPad Prism 9.0 software, with statistical significance defined as $P < 0.05$.

2.Results

To further elucidate the molecular regulatory networks underlying the protective role of NMN in ionizing radiation-induced ovarian insufficiency, we performed RNA sequencing (RNA-seq) based transcriptomic profiling of ovarian tissues from four experimental groups: Ctrl group, 5Gy group, 5Gy+NMN, and NMN group (n=3 per group). After standardized sequencing and quality control, principal component analysis (PCA) revealed well-clustered intra-group distributions, indicating high reproducibility and reliability of the data.

Differential expression analysis focused on 5Gy vs. Ctrl and 5Gy+NMN vs. 5Gy. Volcano plots highlighted a substantial number of upregulated and downregulated differentially expressed genes (DEGs), while Venn diagrams delineated shared and specific DEGs, thereby identifying potential key candidates. Subsequent KEGG enrichment analysis uncovered pathways related to energy metabolism, oxidative stress, and cell survival, and further indicated that NMN could partially restore the transcriptional perturbations induced by radiation exposure.

Global heatmap analysis based on highly significant DEGs outlined the overall transcriptional differences among the four groups. A refined heatmap comparison across the Ctrl, 5Gy and 5Gy+NMN groups provided molecular-level evidence of NMN's protective effects. Importantly, comparison between the Ctrl and NMN groups revealed highly similar transcriptional profiles in both PCA clustering and Venn analysis, suggesting that NMN administration under physiological conditions does not exert adverse effects on ovarian tissue, thereby supporting its safety.

2.1. Sequencing and Quality Control (PCA)

Each sample yielded 2.3–3.1 $\times 10^7$ clean reads with high sequencing quality (Q30 $\geq$ 92%), and 92–96% of reads were successfully mapped to the mouse reference genome (GRCm39). Principal component analysis (PCA) revealed tight clustering

within each group, indicating reliable sequencing and normalization quality with minimal batch effects. Clear separation was observed among the four groups: the 5Gy group was distinctly separated from the Ctrl group along Dim1 (explaining 20.3% of the variance), which represented the major source of variation and reflected profound transcriptional remodeling induced by radiation. The 5Gy+NMN group was positioned between the Ctrl and 5Gy groups and shifted toward the Ctrl cluster, suggesting a partial reversal of radiation-induced transcriptional perturbations by NMN. The NMN group largely overlapped with the Ctrl group, showing no systematic shift, thereby supporting that NMN exerts minimal transcriptional disturbance under physiological conditions and demonstrates good safety. Dim2 (accounting for 16.1% of the variance) mainly captured subtle intra-group differences and secondary biological variation, without altering the overall separation pattern (Fig. 13).

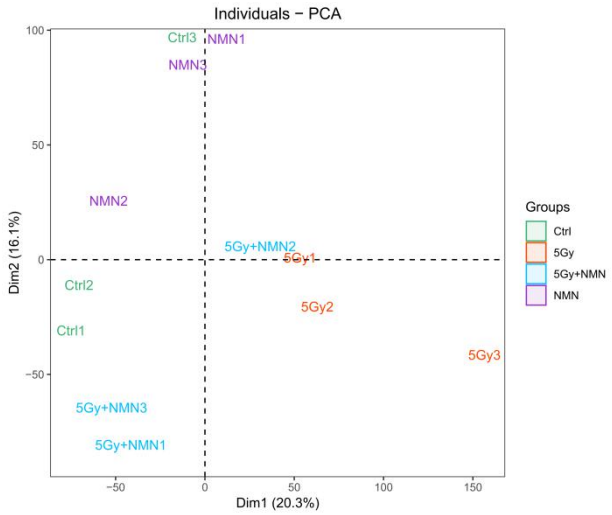

Figure 13. PCA of mouse ovarian transcriptomes

RNA-seq generated 2.3–3.1 × 10^7 clean reads per sample (Q30 ≥ 92%; 92–96% mapped to GRCm39). PCA showed tight intra-group clustering with clear separation among groups. The 5Gy group segregated from Ctrl along Dim1 (20.3% variance), indicating radiation-induced transcriptome remodeling. The 5Gy+NMN group shifted toward Ctrl, suggesting partial reversal by NMN, while the NMN-alone group overlapped with Ctrl, supporting minimal perturbation under physiological conditions.

2.2. Differentially Expressed Genes (DEGs)

The comparison between the 5Gy group and the Ctrl group (Fig. 14A), the volcano plot revealed a large number of differentially expressed genes (DEGs). Upregulated genes were predominantly enriched in pathways related to DNA damage response,

oxidative stress, and apoptosis, with representative genes including Tp53, Bax, Casp3, and Gadd45a, indicating that irradiation activated cell death and stress-response networks. Conversely, downregulated genes were mainly associated with glycolysis/glucose metabolism, energy supply, and ovarian function maintenance, such as Hk2, Pkm2, Ldha, and Slc2a1, suggesting that irradiation markedly suppressed glycolytic flux and energy production.

In the comparison between the 5Gy+NMN group and the 5Gy group (Fig. 14B), the volcano plot identified a distinct set of DEGs, showing a “bidirectional correction” pattern with both upregulation and downregulation, indicative of a partial reversal of radiation-induced transcriptional perturbations by NMN. Specifically, multiple genes involved in glycolysis and lactate metabolism (e.g., HK2, PKM, LDHA, TPI1, PGAM1, ALDOB, SLC16A3), antioxidant and glutathione pathways (e.g., HMOX1, GPX1, GCLC), and mitochondrial electron transport chain/OXPHOS (e.g., COX6B1, COX7A2L, COX17) were significantly altered, indicating a functional recovery of mitochondrial activity and energy metabolism, consistent with the observed improvements in mitochondrial membrane potential and ATP levels. Moreover, transcriptional changes in IRS1, FOXO1, EIF4EBP1, and EIF4E pointed to the reactivation or correction of the insulin/PI3K-AKT-mTOR-HIF-1α signaling axis, further supporting the role of NMN in restoring energy metabolism and cell survival signaling.

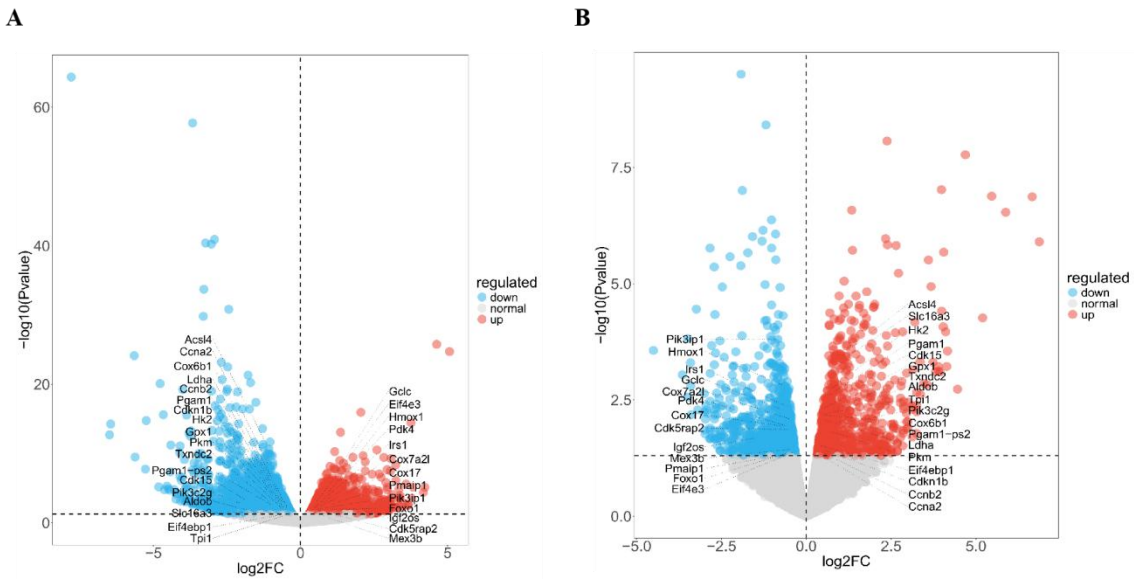

Figure 14. Volcano plot of differentially expressed genes (DEGs) between 5Gy and Ctrl group, 5Gy+NMN and 5Gy group ovarian tissues.

Red dots represent significantly upregulated genes, green dots represent significantly downregulated genes, and gray dots represent non-significant genes.(A)The 5Gy group showed extensive transcriptional alterations, with upregulated genes enriched in oxidative stress and apoptosis pathways, while downregulated genes were mainly associated with glycolysis and energy metabolism, indicating profound radiation-induced transcriptome remodeling. (B) In 5Gy group notable signals include glycolysis transport, antioxidant and heme metabolism, mitochondrial OXPHOS, and PI3K/AKT–mTOR/translation and apoptosis/ferroptosis markers trend downward. Collectively, these changes indicate a partial reversal of radiation-induced transcriptional perturbations by NMN.

By focusing on the Venn diagram analysis of DEGs between the 5Gy vs Ctrl and 5Gy+NMN vs 5Gy comparisons (Fig. 15), we observed that in the 5Gy group relative to Ctrl, 1,574 genes were significantly upregulated and 1,909 genes were significantly downregulated. The upregulated gene set largely represents radiation-induced transcriptional activation, predominantly enriched in pathways related to oxidative stress, DNA damage response, inflammation, and apoptosis. Conversely, the downregulated gene set reflects radiation-suppressed transcriptional programs, mainly involving glycolysis, substrate transport, mitochondrial energy production, steroid biosynthesis, and ovarian function maintenance. Upon NMN intervention (5Gy+NMN vs 5Gy), 872 genes were significantly upregulated and 773 genes were significantly downregulated.

Among these, 1,016 core DEGs (555+461) were identified as overlapping with radiation-responsive genes, representing key molecular targets for elucidating the protective mechanisms of NMN in ovarian function. Specifically, 461 genes were upregulated by radiation but suppressed by NMN, indicating that NMN may attenuate stress- and apoptosis-driven transcriptional programs activated by irradiation. In contrast, 555 genes were downregulated by radiation but restored by NMN, suggesting that NMN reactivates radiation-suppressed metabolic and functional genes, including key glycolytic enzymes, lactate transporters, OXPHOS components, and genes involved in steroidogenesis and granulosa cell function.

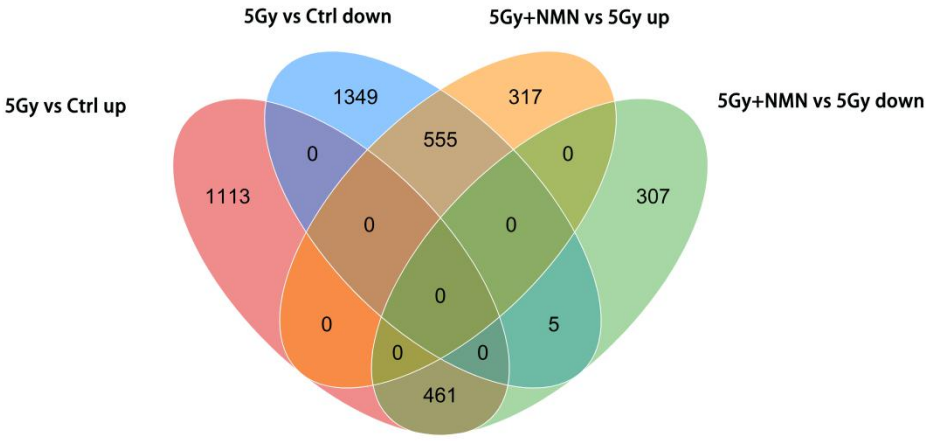

Figure 15. Venn diagram analysis of differentially expressed genes (DEGs)

In the 5Gy vs Ctrl comparison, 1,574 genes were significantly upregulated， and 1,909 genes were significantly downregulated . In the 5Gy+NMN vs 5Gy comparison, 872 genes were upregulated and 773 genes were downregulated. A total of 1,016 core DEGs overlapped between the two comparisons: 461 genes were induced by radiation but suppressed after NMN treatment and 555 genes were suppressed by radiation but restored by NMN. These core DEGs provide key molecular targets for elucidating the protective mechanisms of NMN against radiation-induced ovarian dysfunction.

Further analysis using the overall gene expression heat map (Figure 16A) revealed distinct clustering patterns of differentially expressed genes across groups. The 5Gy group showed the most divergent expression profile compared with the Ctrl group. The 5Gy+NMN group shared partial similarity with the 5Gy group likely reflecting

radiation-induced oxidative stress responses while the remaining profile was closer to Ctrl, suggesting that NMN intervention partially restored the transcriptomic alterations induced by IR. The NMN group clustered closely with Ctrl group, indicating no adverse effects of NMN under physiological conditions. Cluster analysis focusing on genes related to oxidative stress, glycolysis, apoptosis, and PI3K/AKT signaling pathways (Figure 16B) showed that the 5Gy group displayed the largest divergence from Ctrl, whereas both 5Gy+NMN and NMN groups exhibited expression profiles more similar to Ctrl, underscoring the corrective effect of NMN on IR-induced ovarian dysfunction.

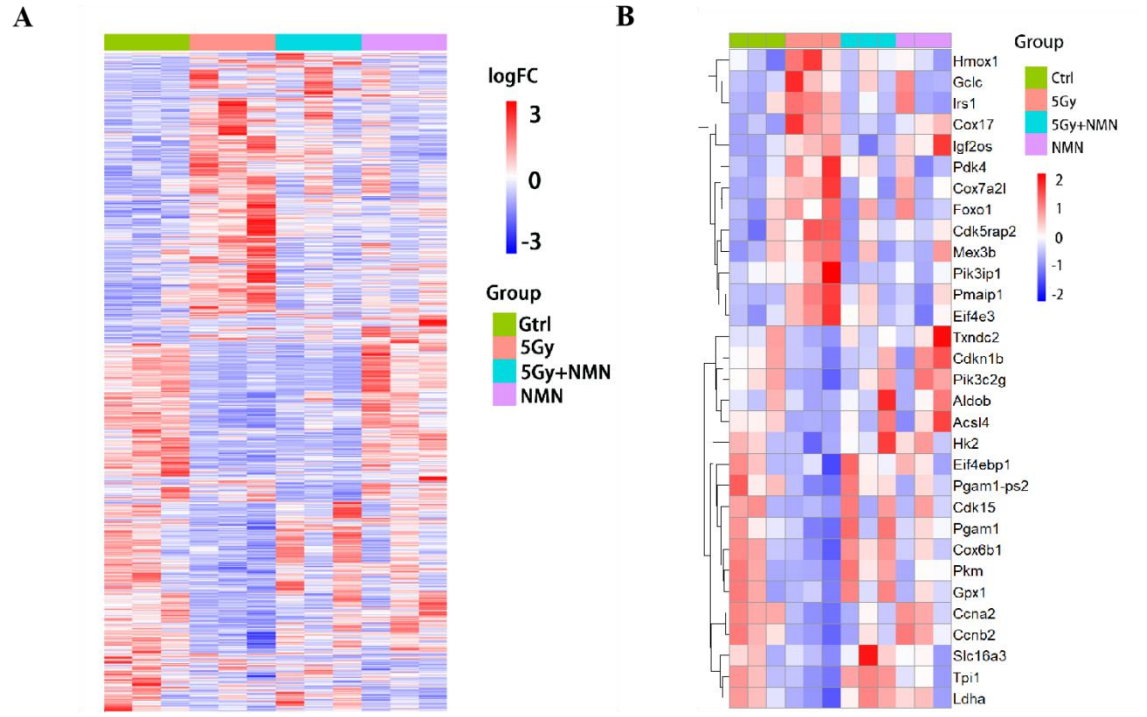

Figure 16. Heatmap analysis of differentially expressed genes

(A) Overall clustering of DEGs revealed that the 5Gy group diverged most strongly from Ctrl, while the 5Gy+NMN group showed partial overlap with 5Gy (oxidative stress–related genes) and partial similarity to Ctrl, indicating a restorative effect of NMN. The NMN group closely resembled Ctrl, suggesting minimal transcriptional disturbance under normal conditions.

(B) Cluster analysis of genes related to oxidative stress, glycolysis, apoptosis, and PI3K/AKT signaling demonstrated marked separation between 5Gy and Ctrl, whereas both 5Gy+NMN and NMN groups were closer to Ctrl, supporting the corrective role of NMN.

Considering that these differentially expressed genes (DEGs) may be involved in the molecular mechanisms by which NMN supplementation improves ovarian reserve, we performed KEGG pathway enrichment analyses for the 5Gy vs. Ctrl and 5Gy+NMN vs. 5Gy comparisons. The enriched pathways showed a high degree of overlap between the two comparisons, predominantly including oxidative stress, glycolysis, apoptosis, and PI3K/AKT signaling regulation (Figure 17A, B).

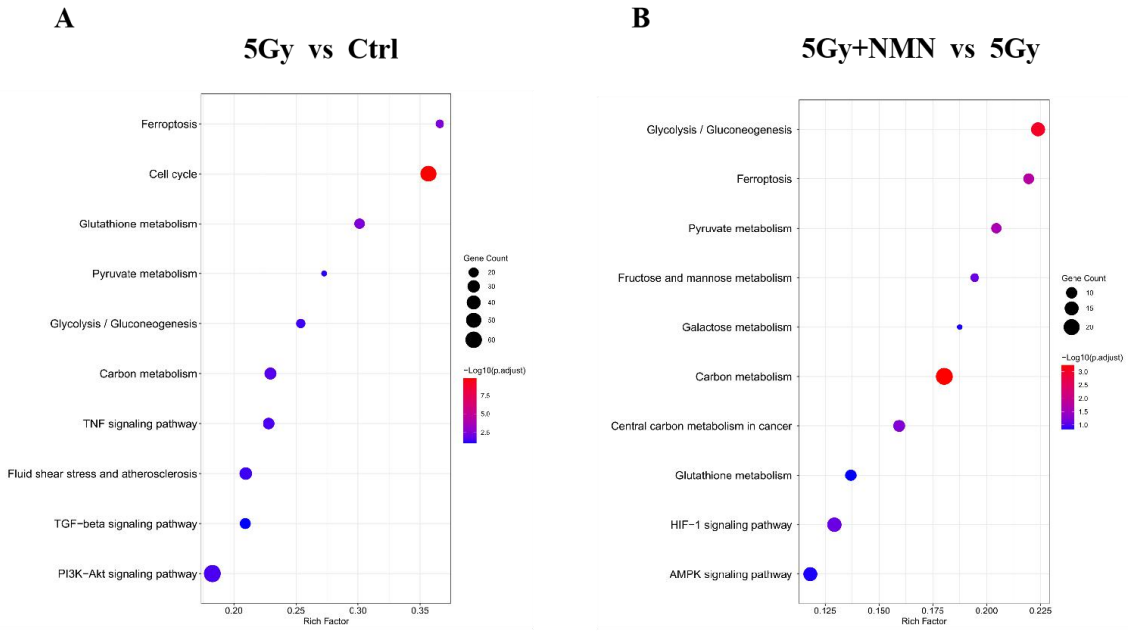

Figure 17. KEGG pathway enrichment analysis of DEGs

(A) KEGG analysis of DEGs between the 5Gy and Ctrl groups. (B) KEGG analysis of DEGs between the 5Gy+NMN and 5Gy groups. The enriched pathways showed substantial overlap between the two comparisons, predominantly involving oxidative stress, glycolysis, apoptosis, and PI3K/AKT signaling regulation, suggesting that NMN supplementation may improve ovarian reserve through modulation of these molecular pathways.

2.3. Safety and specificity

The number of DEGs between NMN and Ctrl was small, the multiple was low, and the enriched pathways were not significant (FDR>0.1), which further supported that

NMN had a small disturbance to ovarian tissue under physiological conditions, its main role was reflected in "directed correction" under radiation damage background.

3. Discussion

This study employed RNA-seq transcriptomic sequencing of mouse ovarian tissues to systematically analyze the molecular characteristics of ionizing radiation-induced ovarian dysfunction at the transcriptional level, while evaluating the transcriptional repair effects of NMN intervention. Overall, the 5Gy radiation group exhibited bidirectional remodeling compared to the Ctrl group, characterized by inhibition of glycolysis and energy metabolism-related transcriptional programs and activation of oxidative stress and cell death-related pathways. In contrast, the 5Gy+NMN group demonstrated a corrective trend toward normalizing these key pathways. Minimal differences were observed between the NMN single-group and Ctrl group, indicating that NMN causes limited disturbance to ovarian tissue under physiological homeostasis with good safety profile. This comprehensive pattern aligns with our observations at both phenotypic and biochemical levels including premature ovarian failure phenotype, decreased AMH/FSH ratio, reduced SOD/MDA levels, insufficient lactate and ATP production, collectively forming a closed loop of ‘radiation-damage-phenotype-molecular network-mechanism validation.’

Suppression of the glycolysis/glucose metabolism axis under radiation and metabolic reconstruction of NMN

Transcriptomic analysis revealed that metabolic pathways including Glycolysis/Gluconeogenesis, Carbon Metabolism, and Pyruvate Metabolism were collectively suppressed. Key enzyme and substrate transport-related genes (e.g., Hk2, Pfkfb3, Pkm2, Ldha) showed decreased transcriptional activity, which aligns with our observations of reduced lactate production and lower ATP levels in ovarian tissue/serum. The suppression of glycolysis not only weakens granulosa cells' metabolic substrate support for oocytes (due to insufficient lactate/acetate supply) but also increases mitochondrial reliance on oxidative phosphorylation, thereby amplifying mitochondrial damage under ROS conditions. In the 5Gy+NMN group, the expression and pathway enrichment of these glycolytic genes demonstrated significant recovery/positive enrichment, indicating that NMN can reconstruct NAD^+

dependent metabolic networks and restore glycolytic flux, providing a foundation for energy and reducing equivalent supplementation. This finding is consistent with recent reports using NMN to improve follicular quality and enhance energy metabolism-related gene expression during radiotherapy or chemotherapy[159].

Coordinated imbalance and correction of upstream energy/survival signals (PI3K/AKT/HIF-1α, mTOR, AMPK, FOXO)

In the upstream regulatory layer, the PI3K-AKT-HIF-1α axis serves as a critical node for maintaining glycolytic programs and cellular survival under stress conditions. Following radiation, gene transcription of PIK3c, Akt1/2, and HIF-1α declines, with mTOR and its downstream components (Rps6kb1/S6K) entering an inhibited state, indicating that energy perception and protein synthesis processes are being suppressed. Meanwhile, AMPK and the FOXO family may exhibit compensatory upregulation or mixed-type regulation under stress (dependent on time windows and cell types), collectively resulting in suppression of proliferation/promotion of autophagy as a short-term survival strategy. In the 5Gy+NMN group, the enrichment levels of PI3K/AKT and HIF-1α related genes and pathways rebounded, aligning with the restoration direction of the glycolytic axis. This suggests that NMN's metabolic protection is not merely substrate supplementation but also involves transcriptional reactivation of upstream signals. The synergy between ‘metabolic-signal’ dual pathways constitutes the core mechanism of NMN's radiation resistance and maintenance of granulosa cell function, which parallels recent findings in middle-aged mice where NMN or NR improved mitochondrial dynamic imbalance to restore follicular development[160].

Imbalance of Oxidative Stress/antioxidant response network and correction of NMN

Radiation-induced ROS surge manifests at the transcriptional level through a state of overactive yet insufficient antioxidant and clearance systems: While pathways like glutathione metabolism and peroxisomes show significant enrichment, key execution genes such as Nfe2l2/Nrf2, HMOX1, Gpx, Sod, Cat, and Prdx are generally

suppressed or imbalanced. Genes associated with lipid peroxidation and ferroptosis (Alox, Ptgs2, Acsl4, etc.) exhibit abnormalities, suggesting the molecular basis for elevated lipid peroxidation markers like MDA. In the 5Gy+NMN group, the Nrf2-ARE axis and glutathione/peroxisome-related genes showed recovery, consistent with biochemical observations of increased SOD activity and reduced MDA. This indicates NMN alleviates the ROS-lipid peroxidation vicious cycle by restoring NADPH/NADH balance and upstream antioxidant transcription programs[161].

Coupling of mitochondrial dysfunction with cell fate pathways

The oxidative phosphorylation (OXPHOS) pathway and mitochondrial structural/mass control genes (e.g., Uqcrc, Cox, Atp5f1, PINK1/PRKN, Mfn/Opa1/Drp1) showed dysregulation. Transcriptional-level inhibition of the OXPHOS pathway combined with kinetic disruption collectively indicate decreased mitochondrial coupling ($\Delta\psi m$) and impaired ATP generation. In the cell fate pathway, apoptosis, p53 signaling, ferroptosis, and autophagy pathways were activated, manifested by upregulation of Bax, Pmaip1/Noxa, Casp9/3, and downregulation of Bcl2. This ultimately leads to granulosa cell apoptosis, follicular atresia, and insufficient hormone synthesis support. In the 5Gy+NMN group, mitochondrial-related genes and OXPHOS pathway transcription rebounded, while cell death pathway enrichment decreased. This suggests NMN's bidirectional improvement through ‘reducing ROS and restoring energy’ effectively mitigates mitochondrial-mediated apoptosis induction. These findings are corroborated by our observations of JC-1 red/green ratio recovery, restored ATP/ATPase activity, and decreased Cleaved Caspase-3 levels at both animal and cellular levels[162].

Implications for mechanism integration and transformation

Through the integrated pathway network of ‘glycolysis/upstream signaling-antioxidant response-mitochondrial function-cell fate’, RNA-seq data reveals a striking alignment with our functional measurements: Radiation pushes the

system beyond the homeostasis of ‘oxidative stress↑-energy limitation-mitochondrial damage-apoptosis/function’, failurewhile NMN restores the system to health by reactivating NAD^+ and antioxidant-metabolic networks. Translationalally, NMN demonstrates "targeted correction" under stress conditions and ‘low disturbance’ in homeostasis, providing a rationale for its potential as a radiation protection/adjuvant therapy strategy. Notably, extensive crosstalk exists between PI3K/AKT and key regulators including HIF-1α, Nrf2, AMPK, and mTOR, with NMN's core pathway and auxiliary pathways potentially varying by dose/time window. Future studies should integrate temporal transcriptomics, spatial transcriptomics/single-cell sequencing, and metabolic isotope tracing to elucidate NMN's spatiotemporal dynamics and cell-type specificity, while validating its effects on follicular lineage remodeling (primordial-primary-secondary) and ovarian microenvironmental reprogramming (endothelial/immune/fibroblastic).

Limitations

The RNA-seq analysis in this study achieved preliminary transcriptionome screening with n=3 per group, though its detection sensitivity for minor effects and population-specific variations remains limited. It should be emphasized that transcriptional levels do not directly equate to protein expression or enzymatic activity, requiring cross-verification through proteomic/polyphosphorylation studies and metabolic flux analysis. Despite comprehensive multi-level validation at cellular and animal models, we recommend implementing genetic/pharmacological multi-omics interventions in subsequent studies to strengthen causal relationships.

4. Summary

RNA-seq analysis revealed that radiation-induced ovarian tissue exhibited a molecular pattern characterized by ‘glycolytic inhibition+antioxidant imbalance+mitochondrial dysfunction+activation of apoptosis pathways’. NMN

achieved systematic reversal of radiation-induced perturbations at the transcriptional level by restoring the PI3K/AKT-HIF-1α glycolytic axis and Nrf2 antioxidant axis, while improving mitochondrial homeostasis. These findings align with our phenotypic, biochemical, and cytological evidence, providing scientific justification for the clinical translation of NMN as an intervention strategy against ovarian radiation damage.

Chapter Ⅴ. NMN Modulates Oxidative Stress in Ovarian Granulosa Cells

Ovarian granulosa cells are pivotal in follicle development and oocyte maturation, maintaining ovarian microenvironment homeostasis through energy provision, sex hormone secretion, and regulatory functions. Their metabolic status directly determines oocyte quality and female fertility. Radiation therapy and environmental hazards can induce ovarian dysfunction, manifesting as depleted follicular reserve, premature ovarian failure, and even reproductive disorders in clinic. IR may trigger oxidative stress, mitochondrial dysfunction, and programmed cell death in GCs by inducing DNA double-strand breaks and excessive ROS production[163], [164]. Oxidative stress not only directly damages granulosa cells but also disrupts their energy metabolism. Studies have shown that GCs primarily rely on lactic acid and ATP generated through glycolysis for energy supply to oocytes[139]. Under oxidative stress, ROS can damage key ovarian glycolysis enzymes such as HK2, PKM2, and LDHA, disrupt NAD^+ /NADH metabolism, exacerbate energy crises, and induce apoptosis[165]. Therefore, investigating the relationship between oxidative stress, glycolytic metabolism, and mitochondrial function in granulosa cells following ionizing radiation is crucial for elucidating the mechanisms underlying radiation-induced premature ovarian failure.

In vitro experiments commonly employ hydrogen peroxide (H_2O_2) treatment to establish cellular oxidative stress models. These models effectively simulate the ROS surge effects induced by radiation or environmental toxins, triggering lipid peroxidation in cell membranes, mitochondrial dysfunction, and apoptosis[166]. This model provides a reliable tool for systematically evaluating the survival status of ovarian granulosa cells, mitochondrial homeostasis, and glycolytic levels under oxidative stress conditions.

NMN has been shown in recent studies to enhance cellular NAD^+ levels, activate the SIRT1/SIRT3 signaling pathway, improve mitochondrial function, strengthen antioxidant defenses, and maintain energy metabolism homeostasis[167]. While existing research indicates NMN's protective effects against radiation-induced or toxic tissue damage[168], [169], [170], its specific mechanisms in addressing oxidative stress damage in ovarian granulosa cells remain unclear.

Building on this foundation, our study aims to establish an oxidative stress model using H_2O_2 to simulate ionizing radiation-induced damage in ovarian granulosa cells. The research will systematically evaluate changes in oxidative stress levels, glycolytic metabolism, and mitochondrial function within the model cells, while investigating the regulatory effects of NMN intervention. This investigation will help elucidate the potential mechanisms of NMN in protecting ovarian function, providing new experimental evidence for early intervention strategies against radiation-induced ovarian damage and premature aging.

1. Materials and Methods

1.1. Experimental Materials

Table 12. Consumables for KGN Cell Culture

Item	Specification	Manufacturer/Brand
Cell culture flasks (T-25 / T-75)	Treated surface, vented cap	Corning

6-well/12-well/24-well plates	Tissue culture grade	Corning
96-well plate	Flat bottom, transparent	Corning
Serological pipettes	1/5/10 mL	Corning
Filter tips	0.1–10/200/1000 μL	Eppendorf

Table 13. Reagents for KGN Experiments

Item	Specification/Grade	Manufacturer/Brand
KGN cells	Human granulosa cell line	RIKEN BRC
DMEM/F-12 medium	With/without phenol red	Gibco (Thermo)
Fetal bovine serum (FBS)	Qualified, heat-inactivated	Gibco
Penicillin-Streptomycin	10,000 U/mL & 10,000 μg/mL	Gibco
Hydrogen peroxide (H_2O_2)30%	Analytical/cell culture grade	Sigma-Aldrich

Table 14. Major Instruments for KGN Experiments

Instrument	Model/Specification	Manufacturer/Brand
Class II Biosafety Cabinet (BSC-II)	MSC-Advantage	Thermo Scientific

CO_2 Incubator	Heracell VIOS 160i	Thermo Scientific
Inverted microscope	CKX53	Olympus
Fluorescence inverted microscope	Eclipse Ti2	Nikon
Multimode microplate reader	Synergy H1	Agilent BioTek

The reagents and consumables used in qRT-PCR and WB are referenced in Chapter ⅳ, 1.1

1.2. Experimental Methods

1.2.1. Preparation of Laboratory Reagents

Preparation of NMN solution

We accurately weighed 16.7 mg of NMN powder using a precision electronic balance, transferred it into a 15 mL conical centrifuge tube, and added 5mL of pre-chilled 0.9% sterile saline. After thorough vortex shaking to ensure complete dissolution, the solution was adjusted to a final volume of 5 mL to prepare a 10 mM NMN stock solution. This stock solution was immediately transferred to a 4°C low-temperature environment for storage. Subsequent experiments can perform gradient dilution operations as required.

Complete culture medium preparation

Perform aseptic operations in a biosafety cabinet. Take a sterilized 50 mL centrifuge tube and sequentially add the following components: 45 mL DMEM high-sugar basal medium, 5 mL fetal bovine serum (FBS), and 1 mL penicillin-streptomycin-amphotericin B mixture (triple antibody). Vigorously mix each component by repeatedly pipetting to ensure thorough blendinimately obtaining a complete medium containing 10% FBS and 1% triple antibody.

Preparation of Hydrogen Peroxide (H_2O_2) Working Solutions

A 100 mM intermediate stock of hydrogen peroxide was prepared on ice and under light protection by diluting 30% (w/w) H_2O_2 (≈9.8 M) into sterile water (102 µL into 9.898 mL). The stock was 0.22µm-filtered (PES), aliquoted into amber tubes, and stored at 4 °C for ≤1 week. Working solutions (100, 250, 500, and 1000 µM) were freshly prepared by diluting the 100 mM stock into complete DMEM/F-12 medium

immediately before use (e.g., for 10mL: add 10, 25, 50, or 100 µL of the 100mM stock, respectively). All solutions were handled with sterile, low-binding plasticware to minimize catalytic decomposition. Optional verification of H_2O_2 concentration was performed spectrophotometrically at 240 nm using $\varepsilon = 43.6 M^{-1} cm^{-1}$, accounting for dilution factors.

The preparation of hydrogen peroxide (H_2O_2) working solutions for oxidative stress modeling in KGN granulosa cells, starting from 30% (w/w, ≈9.8 M) molecular biology grade H_2O_2.

(1) Preparation of 100 mM Intermediate Stock

On ice and protected from light, dilute 30% H_2O_2 stock solution in sterile water:

- Add 102 µL of 30% H_2O_2 into 9.898 mL sterile water (or 10.2 µL into 989.8 µL).
- This yields a 100 mM intermediate stock.
- Optionally filter sterilize through a 0.22 µm PES filter.
- Aliquot into amber tubes, store at 4 °C, use within 1 week (preferably 3–5 days).

(2) **Preparation of Working Solutions (freshly before use) (Table 15)**

Targetconcentration	Volumeof100mMstock	Finalvolume (example)	Volumeofmedium
100 µM	10 µL	10 mL	9.99 mL
250 µM	25 µL	10 mL	9.975 mL
500 µM	50 µL	10 mL	9.95 mL
1000 µM (1 mM)	100 µL	10 mL	9.90 mL
100 µM	50 µL	50 mL	49.95 mL
250 µM	125 µL	50 mL	49.875 mL
500 µM	250 µL	50 mL	49.75 mL
1000 µM (1 mM)	500 µL	50 mL	49.5 mL

(3) Notes and Safety

- Working solutions must be prepared freshly each time, as decomposes rapidly in culture medium.
- Handle 30% H_2O_2 with gloves and goggles; it is corrosive and a strong oxidizer.
- Use sterile plasticware to minimize catalytic decomposition (avoid metal contact).
- Verify concentration spectrophotometrically at 240 nm ($\varepsilon = 43.6 M^{-1} cm^{-1}$) if required.

- Typical KGN treatments: 100–400 μM for 6–24 h, titrated by CCK-8/MTT assays.

1.2.2. Cell Culture

1.2.2.1. Cell Recovery

Activate the air purification system in the cell culture room while operating UV sterilization lamps on the laminar flow cabinet to treat experimental equipment for 30 minutes. During this period, pre-packaged complete culture medium should be placed in a water bath to reach optimal temperature. Heat the constant-temperature water bath to 37°C and transfer KGN or 293T cells from the -80°C freezer into the water bath immediately after thawing until fully dissolved. After disinfecting the vials with medical-grade alcohol, store them in the laminar flow cabinet. Use a pipette to transfer frozen cell suspension into new culture flasks, followed by adding 2 mL of complete medium. Gently aspirate to resuspend cells thoroughly, then shake the flask to ensure uniform spreading. Observe cell morphology under an inverted microscope and mark the flask base for future experiments. Place the flask in a constant temperature incubator for cultivation. After 12 hours, assess cell adhesion and morphology integrity. If over 50% of cells are properly attached with normal morphology, the recovery is confirmed. Since DMSO in the cryopreservation medium may inhibit cell growth, replace the medium after complete adhesion to eliminate this effect.

1.2.2.2. Cell Cryopreservation

Activate the air purification system in the cell culture room 30 minutes prior to operation, while simultaneously activating UV sterilization lamps on the laminar flow cabinet for comprehensive sterilization of experimental equipment. Allow complete culture medium, sterile PBS buffer, and trypsin digestion solution to reach equilibrium temperature at room level. After disinfecting all reagent bottles with 75% ethanol, transfer them into the laminar flow cabinet. Light the alcohol lamp to ensure aseptic conditions.

Using a pipette, aspirate the old medium from the culture flask and add 1mL of sterile PBS for two washes to ensure complete removal of residual medium. After

thoroughly discarding the PBS buffer, add 500 μL of trypsin digestion solution and gently rotate the flask to ensure uniform coverage of the cell layer. Observe real-time morphological changes under a microscope. When adherent cells transition from spindle-shaped to round and begin detaching from the flask base, immediately add 1 mL of complete medium to terminate the trypsin digestion. Use a pipette to repeatedly blow on the flask base (especially the corner areas) to ensure complete cell detachment and formation of a uniform suspension. Transfer the cell suspension to a sterilized 15 mL conical centrifuge tube and centrifuge at 1000 r/min for 5 minutes at room temperature. After removing the supernatant, add 1 mL of pre-chilled serum-free cell cryopreservation medium to the sediment and gently blow to form a single-cell suspension. Seal the tube with a sealing film and label information, then transfer to a dedicated cryovault for long-term storage in an -80 °C ultra-low temperature freezer.

1.2.2.3. Cell Passage

The cell culture rooms and laminar flow hoods were sterilized with 30-minute UV radiation to ensure aseptic conditions. All laboratory supplies were surface-disinfected with 75% medical alcohol and properly stored in laminar flow hoods. Complete culture medium, sterile PBS, and EDTA-containing trypsin digestion solution were pre-extracted from refrigerated storage and thawed to room temperature for later use. During procedures, operations were conducted in aseptic zones surrounding the flame of an ignited alcohol lamp. First, the original culture mediumin petri dishes was aspirated using a sterile pipette, followed by two thorough rinses with 1 mL sterile PBS to completely remove residual liquid. Subsequently, 500 μL trypsin digestion solution was added. The digestion process was terminated under microscopic observation when cell morphology became rounded and intercellular spaces expanded. The cell suspension was transferred to sterilized 15 mL conical centrifuge tubes and centrifuged at 1000 rpm for 5 minutes at room temperature. After discarding the supernatant, 4 mL complete culture medium was added to resuspend cells uniformly. The resuspended cell suspension was then divided into two new 25 cm^2 culture flasks

at a 1:2 ratios. After screwing caps tightly and marking experimental parameters, the flasks were transferred to a cell culture incubator for cultivation.

1.2.2.4. Cell Count and Plate Seeding

Cell count

Clean the counting chamber and coverslip with alcohol swabs. Gently place the coverslip onto the chamber's groove using sterile forceps. Aspirate 10 μL from the single-cell suspension and slowly drop it onto the chamber along the bottom edge, ensuring full coverage. Under the microscope, observe four 1 mm^2 squares using the ‘fortress-style’ counting method. Strictly follow the rule: count only upper/lower cells and left/right cells, recording only complete single cells.

Cell culture plate

Based on the cell count results, perform gradient dilution of the cell suspension using complete medium and precisely adjust to the required inoculation density for each culture plate. Transfer the diluted cell suspension into each petri dish while maintaining a vertical and steady operation with the pipette. Subsequently, gently tap the surface 10 times using the cross-tapping method to ensure uniform cell spreading across the culture medium. Finally, transfer the inoculated culture plates to a constant temperature incubator for cultivation.

1.2.3. Oxidative Stress Model Preparation of KGN Cell Lines

Select ovarian granulosa cell lines (KGN cells, RIKEN RCB1154). Cultivate the cells in DMEM/F-12 medium containing 10% FBS and 1% penicillin-streptomycin at 37°C with 5% CO_2 After two passages, inoculate the cells into 6-well plates at $1\text{-}2\times10^5$ cells per well. Wait until the cells reach the logarithmic growth phase with 70−80% fusion rate.

Prepare the H_2O_2 working solution by freshly diluting the intermediate solution at 100 mM to 100-1000 μM (concentrations of 100, 250, 500, and 1000 μM). Treatment

duration: 0-12 hours (0 h, 4 h, 8 h, 12 h). Determine the optimal dosage and treatment time through CCK-8 pre-experiments (survival rate>60%).

According to the determined concentration and action time of hydrogen peroxide, the groups were divided into control group (equal volume of water/PBS), H_2O_2 group (select appropriate H_2O_2 concentration and action time), and H_2O_2+NMN group (NMN solution 50 μM/L pretreatment for 24 hours and then add appropriate concentration of hydrogen peroxide for action).

1.2.4. Mitochondrial function assays

1.2.4.1. JC-1 detects mitochondrial membrane potential (Δψm)

Reagents: JC-1 kit, PBS (no calcium and magnesium), trypsin, Hoechst 33342.

Culture plate: 24-well plate (imaging), 96-well black transparent plate (enzyme reader reading).

Steps (using 24-well plate as an example)

（1）Wash with PBS once after treatment.

（2）Configure JC-1 working fluid (2-10 μM) according to the instructions.

（3）Add 500 μL to each well and incubate at 37 °C in the dark for 20 min.

（4）Wash twice with JC-1 buffer or PBS, and add fresh medium.

（5）Fluorescence microscopy: red aggregates (Ex/Em 535/595 nm), green monomers (Ex/Em 485/535 nm).

（6）Calculate the red/green ratio and normalize it to the control.

Positive control: 15-30 min of treatment with CCCP 10 μM.

1.2.4.2. DCFH-DA detected intracellular ROS

Reagents: DCFH-DA, serum-free medium, PBS.

Step (96-well plate)

（1）10 mM DCFH-DA was dissolved in DMSO for storage and prepared into 10 μM working solution.

（2）Wash with PBS once after treatment, add 100 μL working solution, and incubate at 37 °C in the dark for 20-30 min.

（3）Wash twice with PBS and add 100-200 μL non-pholred medium.

（4）Fluorescence enzyme label instrument was used to detect Ex/Em 485/535nm.

（5）Result correction: normalized to cell count or protein concentration.

1.2.4.3. ATP quantitative detection (luminescence method)

Reagent: CellTiter-Glo® (Promega G7572).

Step (96-well plate)

（1）Reagent and cell plate were restored to room temperature (20-30 min).

（2）Add equal volume of reagent to each hole (e.g., 100 μL culture + 100 μL reagent).

（3）The sample was oscillated for 2 min and left at room temperature for 10 min to stabilize the signal.

（4）Reading: luminance value (RLU).

（5）Data: ATP level is expressed as RLU/protein or RLU/cell number; absolute amount can be converted by ATP standard curve.

1.2.4.4. ATPase activity detection (inorganic phosphorus method)

Reagent kit: Ca^{2+} /Mg^{2+} -ATPase colorimetric method.

Principle: ATP hydrolysis produces Pi, which interacts with chromogen to form a complex and is detected at 660-700 nm.

sample treatment

（1）After washing cells with ice PBS, add extract (50 mM Tris-HCl, pH 7.4 + 0.1 mM EDTA + protease inhibitor).

（2）Ultrasonic lysis, 12000 × g centrifugation for 10 min, 4 °C, take the supernatant, BCA protein quantification.

Reaction steps:

（1）Add sample (10-20μg protein) to the reaction mixture (containing 3-5 mM ATP) and ±inhibitor (e.g., 1 mM ubeoside).

（2）Incubate at 37 °C for 20-30 min, terminate the reaction, add chromogen and color for 15-20 min.

（3）Readings of 660-700nm; calculate Pi according to the KH_2PO_4 standard curve.

The results showed that ATPase activity = μmol Pi·min^{-1}·mg^{-1} protein.

1.2.5. CCK-8

After two passages of KGN cells, they were inoculated into 96-well plates at 8×10^3 to 1.2×10^4 cells per well, with 100 μL per well. The cells were allowed to adhere overnight, and treatment began when 70-80% of the cells had merged. Groups (with at least 3 technical replicates per group and 3 biological repeats) included: Blank: medium + CCK-8; No cell culture. Control: equal volume of solvent (e.g., water/PBS); Treatment: administration/stimulation as designed (e.g., H_2O_2 100-1000 μM, 0-12 h). After treatment, replace with phenol red-free medium (100 μL per well) if necessary to reduce background noise.

Add 10 μL of CCK-8 reagent per well (1:10 dilution with culture medium), gently mix. Incubate at 37 °C in the dark for 1-2 hours (adjust pre-experimentally for different cell lines to achieve A450≈0.6-1.2). Read the absorbance at 450 nm using a microplate reader (650 nm wavelength for background correction if available). Record the blank well reading for background subtraction.

Cell viability by CCK-8. KGN cells were seeded in 96-well plates ($8-12\times10^3$ cells/well, 100 μL) and treated as indicated. After treatment, 10 μL of CCK-8 reagent (Dojindo CK04) was added per well and incubated at 37 °C for 1–2 h

protected from light. Absorbance was measured at 450 nm (650 nm reference if available). Blank values (medium + reagent without cells) were subtracted.

1.2.6. qRT-PCR

1.2.6.1. Extraction of Cellular RNA

Aspirate the complete medium from the six-well plate and add 1 mL sterile PBS per well for washing. Place the plate on ice and add 500 μL RNA extraction reagent per well. Let it stand at room temperature for 3-5 minutes to fully lyse the cells. Transfer the lysate to a pre-cooled RNase-free labeled centrifuge tube and gently vortex 10-15 times. Centrifuge at 4 °C, 12000 r/min for 15 minutes. Subsequent RNA extraction steps should follow the methods described in Chapter Ⅲ 1.2.2.

1.2.6.2. Primer sequences

Table 16. List of primers

Target (Gene)	ForwardPrimer(5′→3′)	ReversePrimer(5′→3′)
BAX (Human)	TGCTTCAGGGTTTCATCCAG	GGCGGCAATCATCCTCTG
BCL2 (Human)	GGTGGGGTCATGTGTGTGG	CGGTTCAGGTACTCAGTCATCC
CASP3 (Human)	GCTCAGAGAGACATTCATGGG	TGACACAATACACGGGATCTG
HK2 (Human)	TGGAGCCACCACTCCTTTAT	CTTCTCCATCTCGCCTGTTG
PKM (PKM2) (Human)	TCCGCTTCTCCAGCTTCT	GCCACAGGATAGGCAGAGAT
LDHA (Human)	CGACCTGGGATTCCAGTGT	AGGCAACCCCAACAACTG
SOD2 (Human)	CAGACCTGCCTTACGACTATGG	CTCGGTGGCGTTGAGATTG
HIF1A (Human)	CGCATCTTGGACGAGTAAAG	TCAGTTTCTGTGTCGTTGCTG
PIK3CA (Human)	AGGCTGAGGGAGCTTGTAA	GGTCTTGTTGAGGGCAGAGT
AKT1 (Human)	TGGACTACCTGCACTCGGAG	GCCATCATTCTTGAGGAGGAAG

GAPDH (Human)	GGTGTGAACCATGAGAAGTATGA	GAGTCCTTCCACGATACCAAAG

1.2.7. Immunoblotting (Western Blot)

Remove the cell culture dishes from the 37°C incubator and carefully discard the old medium. Add 1mL of pre-chilled PBS (4°C) to each well, gently shaking the dish twice for washing. Add RIPA lysis buffer containing 1 mM PMSF (volume ratio of lysis buffer to PMSF: 100:1) to each well. After resting for 3 minutes, scrape cells off the dish base using a cell scraper and transfer them to pre-chilled 1.5 mL centrifuge tubes. Incubate at 4°C with ice bath for 30 minutes. After lysis completion, centrifuge the tubes at 4°C at 12,000 rpm for 20 minutes. Transfer the supernatant to fresh centrifuge tubes. Subsequent procedures follow those specified in Chapter Ⅲ 1.2.3.

1.2.8. Detection of Metabolites and Sex Hormones in Culture Supernatant

Sample collection and processing

KGN cells were routinely cultured in DMEM/F-12 with 10% FBS. NMN pretreatment was administered 24 hours prior to sampling, followed by H_2O_2 (250 μM) treatment for 8 hours. The supernatant was collected, gently mixed, and transferred to ice. The collected culture medium was centrifuged at 4 °C and 12,000 g, 10 minutes, then the supernatant was aspirated to eliminate residual cells. The aliquots were distributed into 50μLEP tubes. Samples were stored at −80°C for ≤1-2 months. E_2 was lipophilic and stored in low-adhesion centrifuge tubes.

Lactate detection (colorimetric method)

Detection kit: Sigma MAK064, Cayman 700510, BioVision K607. The detection was based on the principle of chromogenic or fluorescent signal generated by lactate oxidase/dehydrogenase reaction.

Specific operation steps:

（1）Prepare a standard curve (0-10 mM).

（2）Add 50 μL of sample and 50 μL of reaction solution to each well.

（3）Incubate at room temperature 20-30 min.

（4）The absorbance of the enzyme detector was detected at 570-590 nm.

Pyruvate assay (deproteinized)

Reagent kit selection: Sigma MAK071, BioVision K609, Abcam ab65342. As pyruvate is unstable, immediate protein removal was required. Protein was removed using an ultrafiltration method with a 10 kDa retention time centrifuge tube. The specific procedures were similar to those for lactate detection, with a standard curve ranging from 0-1 mM and detection at 570-590 nm.

AMH test (ELISA)

Selection of kits: Ansh Labs AL-105; Beckman Coulter AMH Gen II; Abcam ab260076.

detailed procedures ：

（1）Equilibrate at room temperature and prepare the standard (0.05-15 ng/mL).

（2）Add 50 μL of sample or standard to each well and incubate for 1-2 h.

（3）Wash the plate 3-5 times, add the detection antibody and incubate again.

（4）Wash the plate, add HRP-TMB for color development and terminate the reaction.

（5）The 450 nm detection of the enzyme detector was performed, and the concentration was calculated by fitting the 4PL curve.

E_2 detection (ELISA)

ELISA kits selected: Cayman 582251, Enzo ADI-900-174, DRG EIA-2693. The detection limit typically ranges from 10−30 pg/mL. Since background E_2 is present in FBS, serum was removed using charcoal stripping (charcoal-stripped FBS). The assay was validated by LC-MS/MS: the supernatant was extracted with ethyl acetate, purified via nitrogen blow-down, and reconstituted in methanol before injection. E_2 was detected in MRM mode, with the recommended internal standard being E_2-d5.

1.2.9. Statistical Analysis

All data were analyzed with at least three replicates. Shapiro-Wilk tests were first conducted to assess normality. For normally distributed data, one-way ANOVA was employed for inter-group comparisons, with Tukey's test used for multiple comparisons. Results were presented as mean ± standard deviation (M±SD).

2. Results

2.1. Effects of IR on KGN Cells

2.1.1. Effects of IR on Oxidative Stress in KGN Cells and NMN Intervention

To evaluate the protective effect of NMN against irradiation-induced oxidative stress in KGN cells, we examined the expression of the lipid peroxidation marker MDA and the SOD. Western blot analysis revealed that SOD expression was markedly decreased while MDA expression was significantly increased in the 5Gy irradiation group, indicating a substantial elevation of oxidative damage following irradiation. Notably, pretreatment with NMN 24 h prior to irradiation effectively attenuated these alterations: SOD expression in the 5Gy+NMN group was significantly higher than in the 5Gy group, whereas MDA levels were significantly reduced, approaching those of the control group. Cells treated with NMN alone exhibited no significant changes, with both SOD and MDA remaining stable. Statistical analysis (n=3) confirmed that NMN significantly mitigated irradiation-induced oxidative stress ($p<0.01$).

In summary, these results suggest that NMN markedly alleviates oxidative stress in irradiated KGN cells by enhancing antioxidant defenses and reducing lipid peroxidation damage.

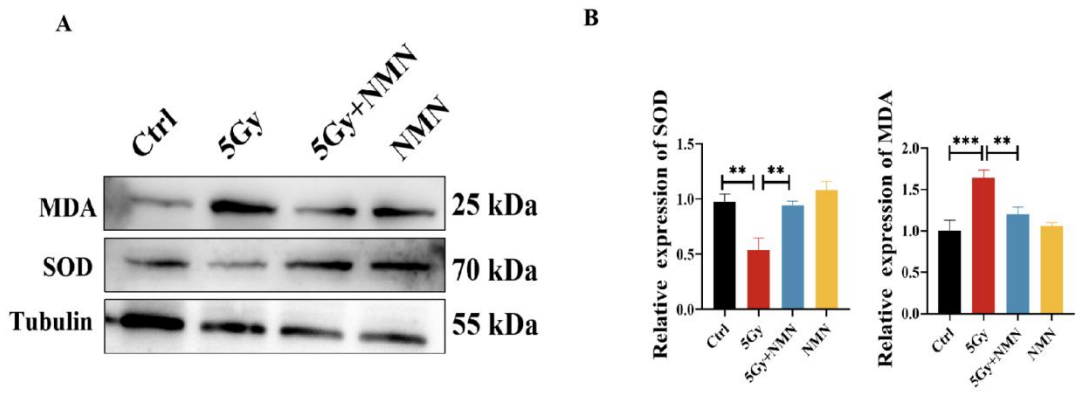

Figure 19. Protective effects of NMN against irradiation-induced oxidative stress in KGN cells

(A) Western blot analysis showed that 5Gy irradiation significantly decreased SOD protein levels and increased MDA expression, while pretreatment with NMN 24 h prior to irradiation markedly reversed these changes.

(B) Quantification indicated that SOD expression was significantly reduced and MDA levels significantly increased in the 5Gy group, whereas NMN pretreatment significantly restored SOD expression and decreased MDA levels. Data are presented as mean ± SD (n=3). **p<0.01, ***p<0.001.

2.1.2. Effects of IR on Apoptosis of KGN Cells and Effects of NMN Intervention

To further investigate the effect of NMN on irradiation-induced apoptosis in KGN cells, we examined the expression of apoptosis-related proteins Bax, Bcl-2, Caspase-3, and its cleaved active form (Cleaved caspase-3). Western blot analysis demonstrated that compared with the control group, the 5Gy irradiation group showed significantly increased expression of Bax, Caspase-3 and Cleaved caspase-3, accompanied by a marked decrease in Bcl-2 expression, indicating that irradiation promoted apoptosis in KGN cells. Notably, NMN pretreatment 24 h prior to irradiation significantly attenuated these changes Bax, Caspase-3 and Cleaved caspase-3 expression were markedly reduced, while Bcl-2 levels were restored, and NMN group expression was closer to that of the control group. Statistical analysis (n=3) confirmed that these differences were significant (*p<0.05，**p<0.01).

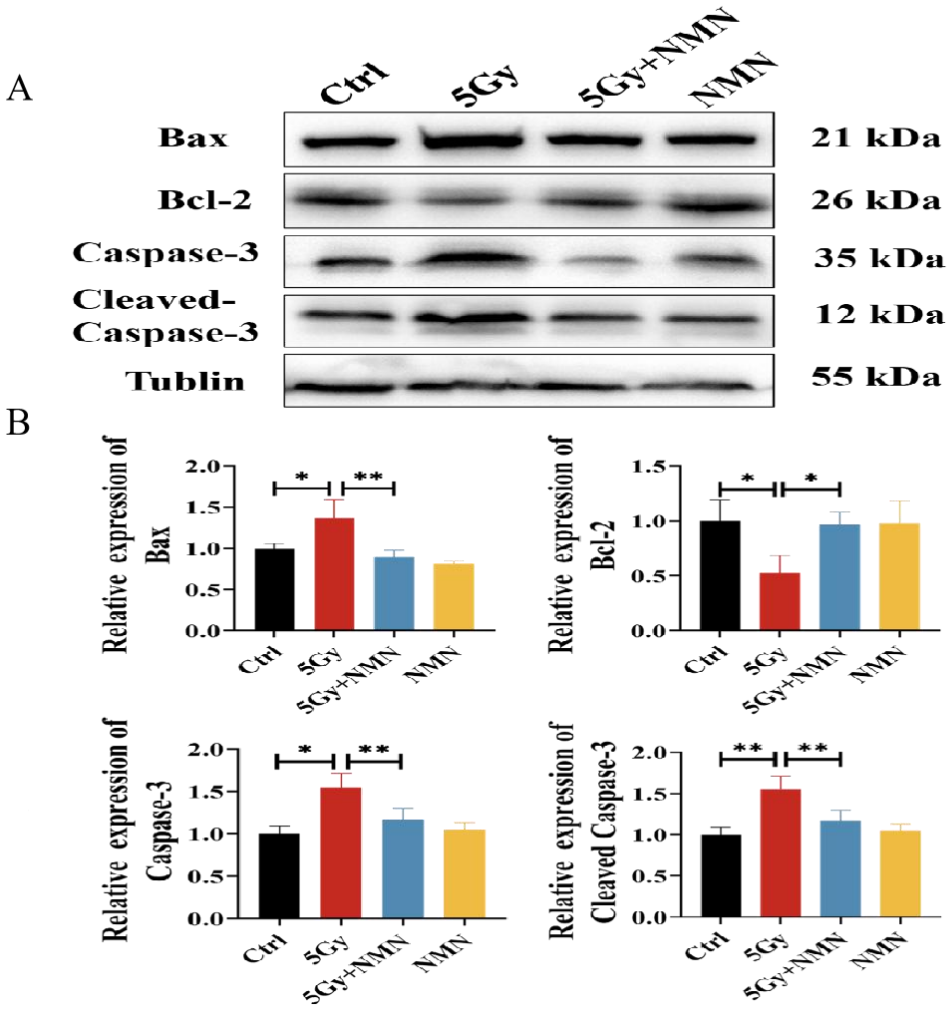

Figure 20. Effects of NMN on radiation induced apoptosis in KGN cell (n=3)

(A) Western blot results showed that 5Gy irradiation markedly increased Bax and Cleaved caspase-3 expression while reducing Bcl-2 expression, whereas NMN pretreatment 24 h prior to irradiation significantly reversed these changes. Tubulin was used as a loading control.

(B) Quantitative analysis indicated that Bax and Cleaved caspase-3 levels were significantly higher and Bcl-2 levels were significantly lower in the 5Gy group compared with the control group. NMN pretreatment significantly inhibited pro-apoptotic protein expression and restored Bcl-2 expression. Data are presented as mean ± SD (n=3). *p<0.05, **p<0.01.

2.2. Establishment of KGN Cells Oxidative Stress Model

To establish an oxidative stress model for KGN, this study tested different H_2O_2 concentrations (0 μM/L, 100 μM/L, 250 μM/L, 500 μM/L, 1000 μM/L) at 0, 4, 8, and 12 h. The CCK-8 assay was used to evaluate cell viability and identify optimal conditions. Results showed that cell viability gradually decreased with increasing H_2O_2 concentration and treatment duration. While the 100 μM concentration showed

no significant effect, both 500 μM and 1000 μM concentrations caused sharp declines in viability at 8 and 12 h, with some conditions recording survival rates below 40%, which hindered subsequent mechanistic studies. In contrast, the 250 μM × 8h concentration maintained approximately 70% viability, enabling stable and reproducible stress-induced damage while preserving sufficient cells for functional experiments. Therefore, 250 μM × 8 h was determined as the optimal condition for constructing the KGN oxidative stress model.

To establish an oxidative stress model of KGN, cells were treated with H_2O_2 at different concentrations (0, 100, 250, 500, 1000 μM) for 4, 8, and 12 h. Cell viability was assessed by the CCK-8 assay to determine suitable exposure conditions. The results showed a dose- and time-dependent decrease in cell viability. Treatment with 100 μM H_2O_2 had little effect on cell viability, while 500 μM and 1000 μM markedly reduced viability to below 40% after 8−12h, making them unsuitable for further mechanistic studies. In contrast, treatment with 250 μM H_2O_2 for 8 h reduced cell viability to approximately 70%, representing a stable and reproducible stress phenotype that induced significant cellular injury while retaining sufficient viable cells for downstream assays. Thus, 250 μM × 8 h was identified as the optimal condition for constructing the KGN oxidative stress model.

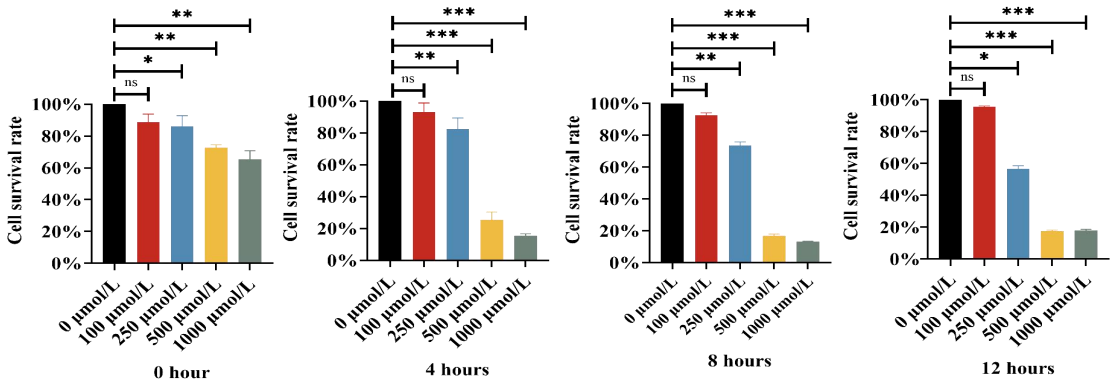

Figure 21. Effects of H_2O_2 on KGN cell viability assessed by CCK-8 assay

KGN cells were treated with various concentrations of H_2O_2 (0, 100, 250, 500, 1000 μM/l) for o 4, 8, and 12 h, and cell viability was measured using the CCK-8 assay. Cell viability decreased in a concentration- and time-dependent manner. Treatment with 250 μM H_2O_2 for 8h produced a moderate and reproducible reduction in cell viability and was therefore selected as the optimal condition for subsequent experiments. Data are presented as mean ± SD (n=3). *p<0.05, **p<0.01 versus control.

2.3. Regulation of Oxidative Stress Levels in the KGN Cells Oxidative Stress Model by NMN

To confirm NMN's antioxidant effects in the KGN oxidative stress model, Western blot was employed to detect SOD and MDA protein expressions, while colorimetric kits were used to measure SOD, CAT enzyme activities, and the total glutathione/oxidized glutathione(T-GSH/GSSG) ratio along with MDA levels. Western blot analysis revealed that compared to the control group, H_2O_2 treatment significantly decreased SOD protein expression while markedly increasing MDA protein signals, indicating enhanced oxidative damage. In contrast, the H_2O_2 + NMN group showed a marked recovery of SOD expression and a significant reduction in MDA levels, approaching control group levels (Figure 22A). Colorimetric assays demonstrated that H_2O_2 treatment significantly reduced SOD and CAT activity, lowered the T-GSH/GSSG ratio, and elevated MDA levels compared to the Ctrl group. Importantly, NMN intervention reversed these effects through early intervention.

The combined WB and colorimetric detection results showed that H_2O_2 successfully induced the oxidative stress state of KGN cells (decreased expression/activity of antioxidant enzymes and increased lipid peroxidation), while NMN could effectively improve the antioxidant capacity of cells, reduce lipid peroxidation level, and play a significant antioxidant protective effect.

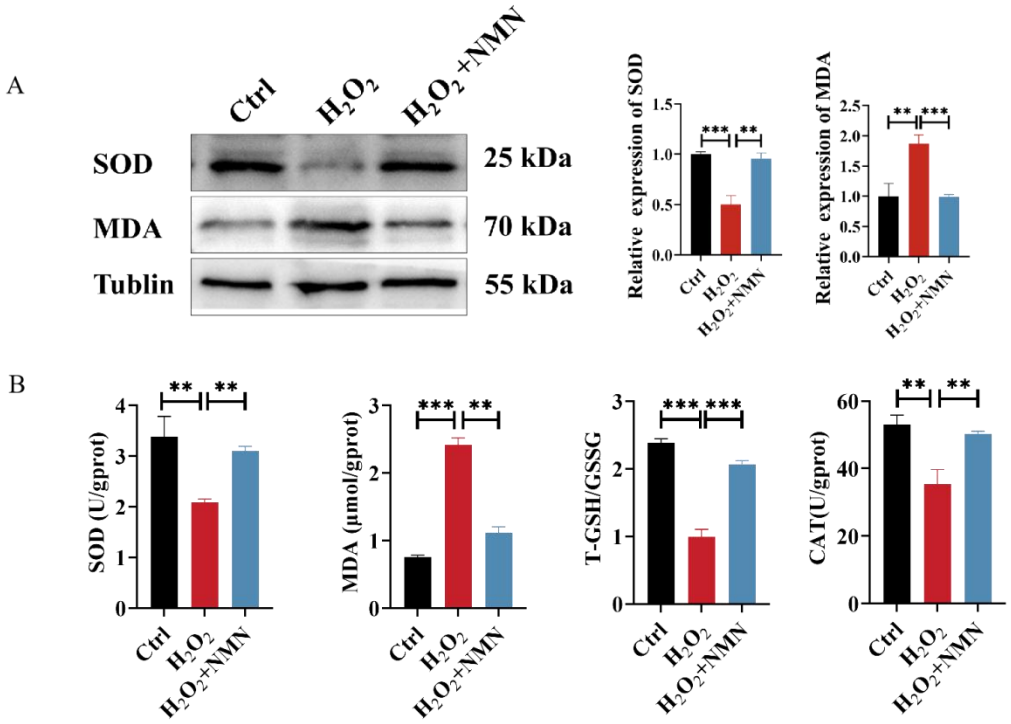

Figure 22. NMN alleviates KGN cell oxidative stress induced by H_2O_2

(A) Western blot analysis revealed representative bands for SOD and MDA, with β-tubulin serving as the internal control. Groups: Ctrl, H_2O_2 (H_2O_2 250 μM × 8 h), and H_2O_2+NMN (pre-treated with NMN before modeling). Quantitative WB gray-scale analysis showed decreased SOD expression and increased MDA levels in the Ctrl group; NMN intervention significantly reversed these changes.

(B) Colorimetric assay: SOD activity, CAT activity, T-GSH/GSSG ratio, and MDA content. The H_2O_2 group exhibited decreased SOD and CAT activity, reduced T-GSH/GSSG ratio, and elevated MDA levels. After NMN intervention, SOD and CAT activity were restored, T-GSH/GSSG ratio increased, and MDA decreased.

The data were expressed as mean ± standard deviation (mean ± SD), n=3; **p<0.01, ***P <0.001.

2.4. Regulation of Glycolysis and Sex Hormone Levels by NMN in the Oxidative Stress Model of KGN

To elucidate the effects of oxidative stress on glycolysis and endocrine function in granule cells and evaluate NMN's metabolic protective effects, we detected mRNA and protein expressions of key glycolytic enzymes HK2, PKM2, and LDHA (Figure 23). We also measured lactate and pyruvate levels in cell culture supernatants (Figure 24) and sex hormones AMH and E_2 (Figure 25). Compared with the control group, H_2O_2 group showed significantly reduced mRNA and protein expression of these enzymes (qPCR and Western blot). In NMN pretreatment group, expression of these three enzymes rebounded markedly (though still slightly lower than control),

indicating NMN partially restored H_2O_2 induced oxidative stress and inhibited the glycolytic axis in granule cells (Figure 23A, B). Further analysis of end products lactate and pyruvate revealed increased pyruvate and decreased lactate levels in H_2O_2 group compared to control, consistent with our earlier animal study results (Figure 24A, B). To investigate NMN's effects on endocrine function during oxidative stress, ELISA detection of supernatants showed significantly reduced AMH and E_2 levels in H_2O_2 group, indicating oxidative damage to endocrine function. Conversely, H_2O_2+NMN group demonstrated significant recovery of these hormones, approaching or partially restoring to control levels (Figure 25A, B). H_2O_2-induced oxidative stress inhibits the HK2-PKM2-LDH axis and reduces lactate/pyruvate production, accompanied by decreased AMH and E_2 secretion, indicating a progression from 'glycolytic impairment → insufficient energy and substrate supply → impaired granulocyte function'. NMN significantly upregulates key glycolytic enzymes, restores end metabolites, and improves AMH/E_2 secretion, demonstrating dual metabolic and endocrine protective effects against oxidative damage.

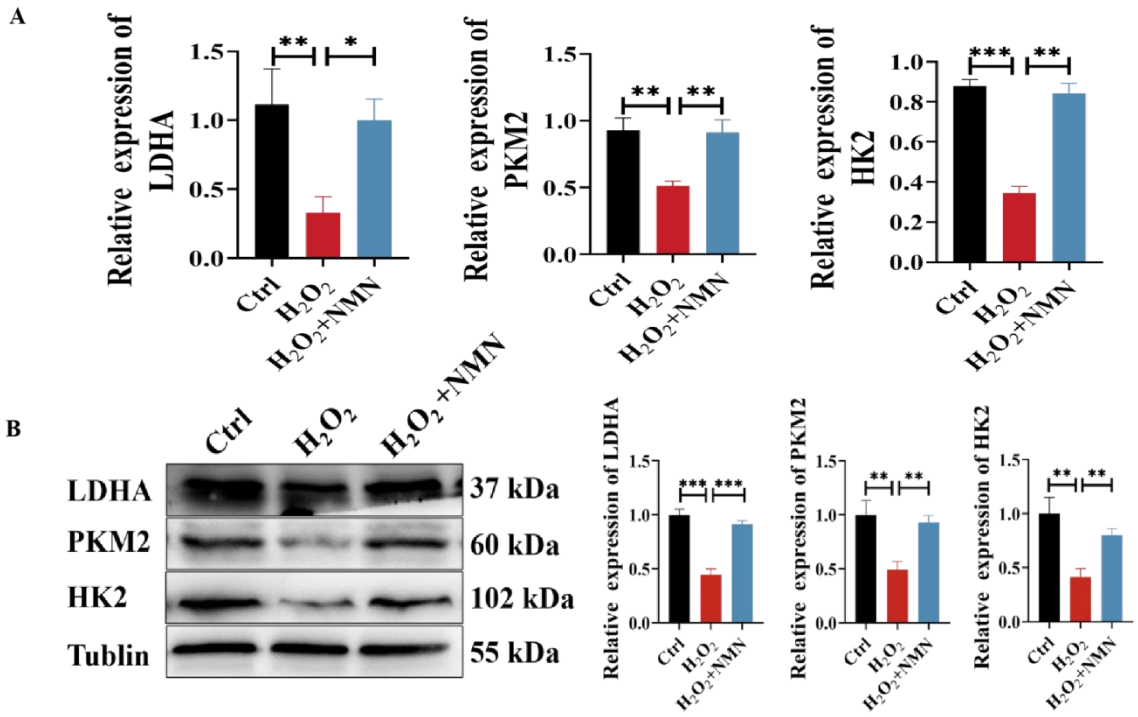

Figure 23. Effects of NMN on key enzymes of glycolysis in KGN cells induced by H_2O_2(n=3)
(A) The relative mRNA expression of key enzymes in each group was detected by qPCR;
(B) Western blot and gray-scale analysis were used to detect the expression of key glycolytic enzyme protein; tubulin served as the internal reference. Data are presented as mean ± standard deviation (n=3), with *p<0.05, **p<0.01, and ***p <0.001 significance levels.

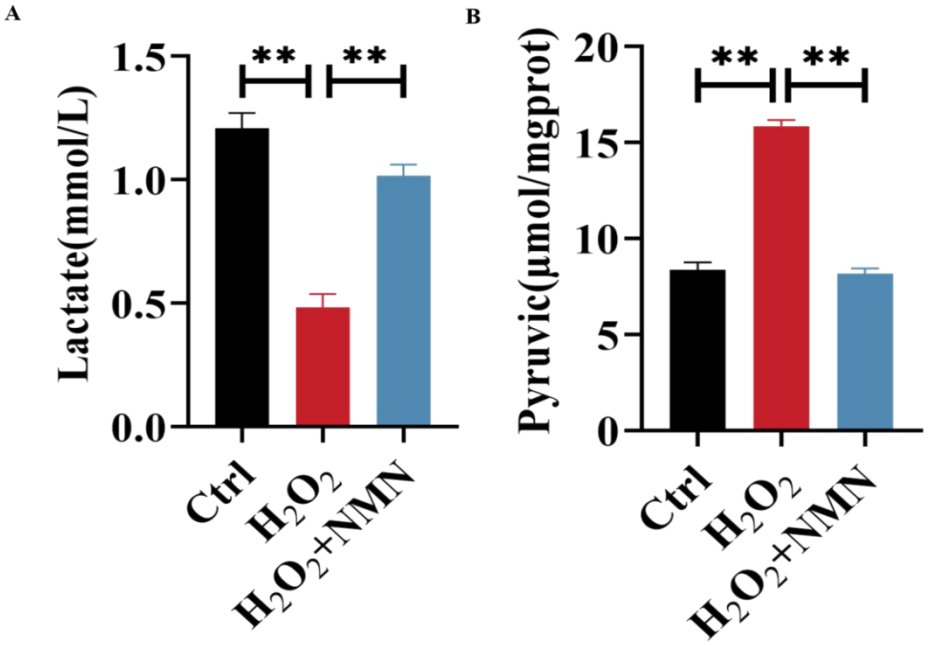

Figure 24. Effects of NMN on end metabolites of KGN cell glycolysis induced by H_2O_2
(A) The content of lactic acid in the culture supernatant was detected by colorimetric method. H_2O_2 group decreased significantly compared with the control group, and the addition of NMN promoted the recovery of lactic acid production
(2) The pyruvate content in the culture supernatant was detected by colorimetric method. H_2O_2 group was significantly higher than the control group, and the addition of NMN promoted the pyruvate production to be consistent with the control group
Data are expressed as mean ± SD (n=3), **p<0.01.

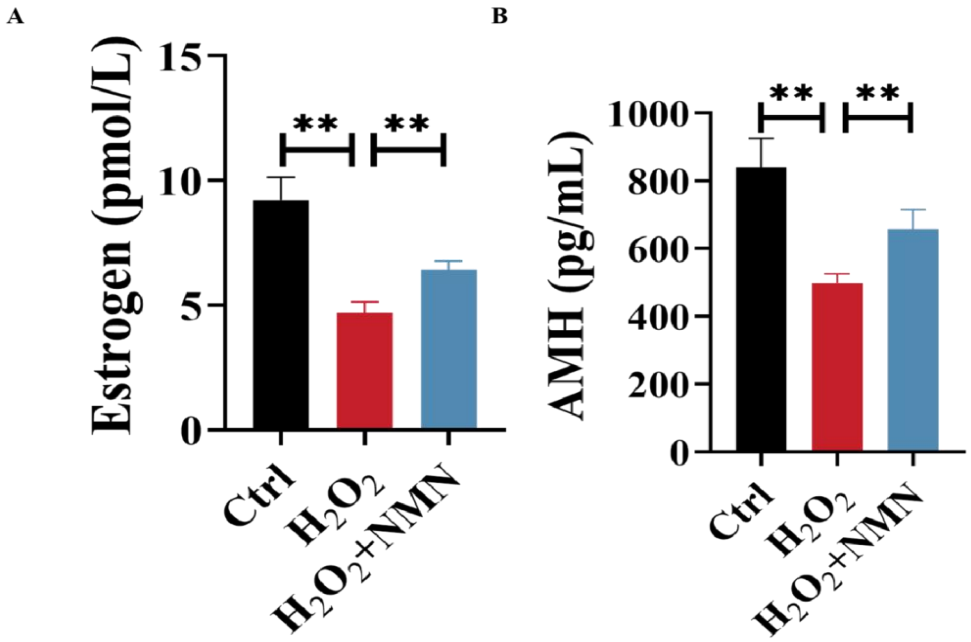

Figure 25. The effect of NMN on the restoration of endocrine dysfunction in KGN cells induced by H_2O_2

（A）The ELISA method was used to determine the E_2 level in the culture supernatant. H_2O_2 group decreased compared with the control group, indicating decreased ovarian function, and the NMN addition was similar to the control group.
（B）The ELISA method was used to determine AMH in the culture supernatant. Compared with the control group, H_2O_2 group was significantly reduced, reflecting the decreased ovarian reserve function. NMN pretreatment played a protective role in the damage, which was similar to the control group.
Data are expressed as mean ± SD (n=3), **p<0.01.

2.5. Effects of NMN on Mitochondrial Function in the Oxidative Stress Model of KGN

In order to evaluate the effect of chemical oxidative stress on mitochondrial function of granular cells and the protective effect of NMN, JC-1 staining was used to evaluate mitochondrial membrane potential (Δψm), and DCFH-DA was used to evaluate intracellular ROS level.

When observing mitochondrial membrane potential (JC-1), the H_2O_2 group exhibited a typical decrease in Δψm compared to the control group: enhanced JC-1 monomer (green) signals and significantly reduced JC-1 aggregates(red), leading to a decreased red/total green ratio(aggregates/monomers), indicating mitochondrial

depolarization. The H_2 O_2 +NMN group showed a marked rebound in red aggregate signals and decreased green monomer signals, with a significantly higher red/total green ratio than the model group and approaching control levels. The CCCP group, as a positive control, demonstrated near-complete depolarization (strong green, weak red). Intracellular ROS (DCFH-DA) was also observed.

The green fluorescent intensity in the H_2O_2 group was significantly higher than that in the control, indicating an elevated ROS load within cells. The model + NMN group showed markedly lower fluorescence intensity compared to the H_2O_2 group, demonstrating NMN's ability to significantly reduce oxidative stress levels. ROSUP (positive control) treatment also induced elevated ROS fluorescence. Collectively, NMN maintains mitochondrial membrane potential $\Delta\psi m$ stability and reduces intracellular ROS under oxidative stress conditions, suggesting its dual protective effects on mitochondria and antioxidant mechanisms.

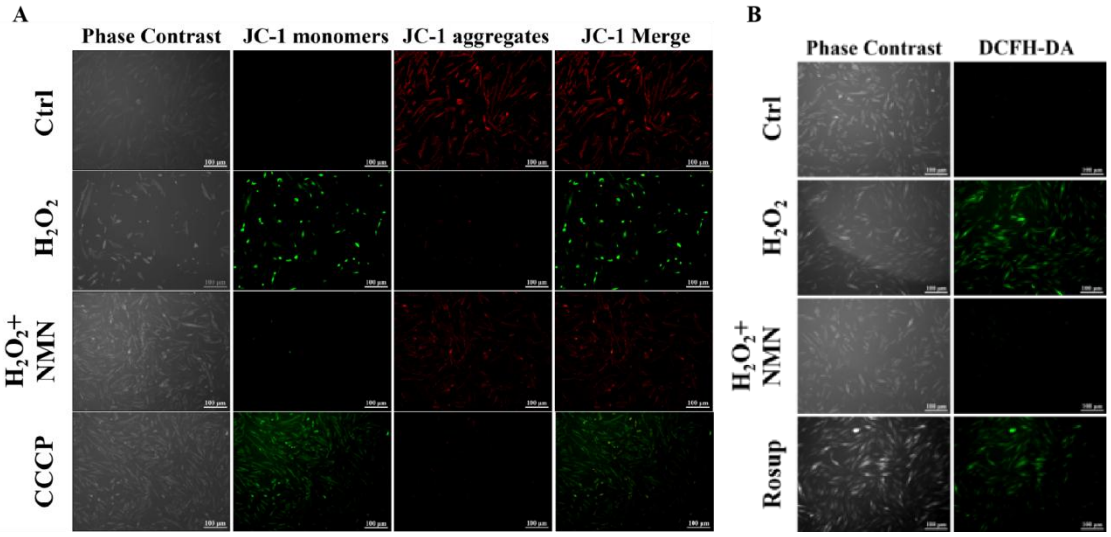

Figure 26. NMN improves the decrease of mitochondrial membrane potential and reduces ROS level in KGN cells induced by H_2O_2

(A) Phase contrast images, JC-1 monomers (green fluorescence), JC-1 aggregates (red fluorescence), and merged images demonstrate changes in Δψm values across groups. Compared to the control group, H_2O_2 treatment showed decreased Δψm (green ↑/red ↓), while NMN pretreatment significantly restored it (red ↑/green ↓). CCCP served as a depolarization positive control. (B) DCFH-DA fluorescence imaging reveals increased ROS levels in H_2O_2 group and

reduced ROS after NMN treatment. ROS is expressed as average green fluorescence intensity. Data are presented as mean ± standard deviation (mean ± SD), with n=3 per group and ≥5 fields per well. Significance: $p<0.05$. Scale bar represents 100μm, as annotated in the figure.

3. Discussion

Building upon previous animal studies, this research further validated at the KGN level that ionizing radiation significantly induces oxidative stress and triggers mitochondrial pathway-mediated apoptosis. Notably, NMN pretreatment exhibits distinct protective effects against these damages through antioxidant, anti-apoptotic, and metabolic repair mechanisms. This finding aligns with the pathogenesis of radiation-induced ovarian damage: Ionizing radiation generates substantial ROS via water ionization, inducing DNA damage, lipid peroxidation, and protein oxidation. These processes ultimately disrupt the ovarian microenvironment and follicular cell homeostasis, leading to ovarian dysfunction and follicular atresia [62], [171].

Oxidative stress is a key hub of granulocyte injury

In the H_2O_2 (250 μM, 8 h) chemical oxidative stress model we constructed, DCFH-DA revealed a significant increase in total ROS. JC-1 assays demonstrated decreased mitochondrial membrane potential ($\Delta\psi m$), while Bax, caspase-3, and cleaved-caspase-3 were upregulated alongside Bcl-2 downregulation, indicating activated mitochondrial-mediated apoptosis. This cascade aligns with the classic pathway of 'ROS elevation → $\Delta\psi m$ reduction → cytochrome c release → caspase cascade'[172], [173]. Concurrently, elevated MDA levels, reduced glutathione (T-GSH/GSSG) levels, and decreased SOD and CAT activity suggest that lipid peroxidation and depletion of antioxidant barriers jointly contribute to cellular fate determination.

Coupling of oxidative stress and glycolysis: from substrate and flux to explain ovarian dysfunction

The metabolic coordination between ovarian granulosa cells and oocytes is highly dependent on glycolysis. Granulosa cells utilize glucose as a substrate to produce lactate/acetate for oocyte utilization[174]. Our observations revealed that radiation/

H_2O_2 significantly downregulated the mRNA and protein levels of HK2, PKM2, and LDHA, leading to decreased lactate/acetate content in culture supernatants. Simultaneously, the secretion of sex hormones AMH and E_2 from granulosa cells was reduced. This suggests that oxidative stress not only disrupts mitochondrial function but also inhibits glycolytic flux and end-product supply, weakening the ovarian microenvironment from both 'substrate insufficiency + energy limitation' perspectives. Consequently, this compromises granulosa cells' ability to provide metabolic substrates for oocytes and their endocrine functions. This finding aligns with the concept that glycolytic products from granulosa cells maintain oocyte metabolic and developmental potential[47].

Metabolic protection of NMN: NAD^+ supplementation achieves repair of both mitochondrial and glycolytic pathways

NMN serves as a direct precursor to NAD^+. Extensive research demonstrates that NMN supplementation enhances cellular NAD^+ levels and activates SIRT1/SIRT3, thereby improving mitochondrial electron transport chain complex function, boosting antioxidant responses, and inhibiting NAD^+ depletion caused by PARP overactivation [175]. In this study, NMN pretreatment significantly restored SOD/CAT activity and the T-GSH/GSSG ratio, reduced MDA and ROS levels, improved $\Delta\psi m$, and decreased Bax, caspase-3, and cleaved caspase-3. It also markedly elevated HK2, PKM2, and LDHA levels while increasing lactate/acetate production, accompanied by rebound secretion of AMH and E_2. These findings indicate that NMN achieves bidirectional repair of mitochondrial function and glycolytic axis through its supplementation, demonstrating its ability to influence granular cell function at multiple metabolic nodes.

Methodology and model significance

(1) We screened the optimal H_2O_2 condition of 250 $\mu M \times 8$ h by CCK-8 dose-time curve, which can not only induce stable and measurable oxidative stress, but also retain sufficient viable cells for multi-indicator combined evaluation, which is replicable and scalable for subsequent drug intervention and pathway analysis.

(2) The JC-1 red/green ratio combined with DCFH-DA can describe the process of mitochondrial steady state change from the membrane potential and oxidative load respectively.

Limitations and prospects

First, while ionizing radiation and H_2O_2 share commonalities in 'oxidative stress' mechanisms, their upstream injury profiles, including DNA double-strand breaks and PARP-mediated NAD^+ depletion, remain distinct. Second, the direct regulatory factors underlying glycolysis downregulation (e.g., interactions between HIF-1α, PI3K/AKT, AMPK-PGC-1α, and Sirtuin) require further clarification. Third, whether NMN enhances NAD^+ levels through metabolic pathways like lactate transporter (MCTs)/NADH-NAD^+ cycle remains unproven by fluxomics studies. Future research should integrate transcriptomic, metabolomic, and mitochondrial respiration analyses (Seahorse) with single-cell/spatial omics approaches, using specific inhibitors or gene editing to pinpoint key pathways and targets. This will comprehensively elucidate how the 'NMN-NAD^+-Sirtuin-mitochondria-glycolysis' network regulates radiation-induced ovarian damage.

4. Summary

In summary, our study on ionizing radiation (which mimics the damage process of radiotherapy on ovarian granulosa cells) in NMN-treated granulosa cell lines revealed significant oxidative stress and apoptosis following radiation exposure. NMN intervention effectively maintained cellular homeostasis in these cells, demonstrating antioxidant and anti-apoptotic effects. This confirms oxidative stress as a critical factor in granulosa cell apoptosis, consistent with earlier animal experiments. To further explore NMN's protective mechanism against radiation-induced damage, we plan to investigate energy metabolism changes in granulosa cells from an oxidative stress perspective, aiming to elucidate NMN's action mechanisms.

We successfully established an oxidative stress model in granulosa cells using hydrogen peroxide, with optimal concentrations of 250 μmol and 8-hour exposure serving as standard parameters. Through comprehensive analysis of oxidative stress levels, expression patterns of key glycolytic enzymes, production of metabolic end products, sex hormone generation, and mitochondrial membrane potential stability, we hypothesize that granulosa cell apoptosis ultimately results from oxidative stress and NAD^+ deficiency, which deplete energy metabolism substrates and pathways in both granulosa cells and oocytes. However, the specific mechanisms likely involve

multi-level, network-like regulation. Building on these metabolic regulatory key points, we further investigated primary signaling pathways and target molecules underlying this regulatory mechanism.

Chapter Ⅵ. NMN's Energy Metabolism Regulation Effect on the Oxidative Stress Model of KGN through PI3K/AKT Signaling Pathway

GCs play a crucial role in follicular development and sex hormone synthesis, with their functions being precisely regulated by cellular energy metabolism and redox homeostasis. Oxidative stress can lead to mitochondrial dysfunction, accumulation of ROS, and apoptosis in granulosa cells, thereby reducing sex hormone secretion (e.g., AMH, E_2) and impairing ovarian function. In recent years, NMN, a precursor of NAD^+ , has been extensively studied as an intervention that improves mitochondrial function, reduces oxidative stress, and regulates cellular metabolism by restoring NAD^+ levels. Multiple cell and animal models have demonstrated NMN's ability to decrease ROS, restore mitochondrial membrane potential (as indicated by JC-1), and enhance antioxidant enzyme activity (e.g., SOD), thereby protecting cellular function[176]. Recent studies in granulosa cell models and ovarian function-related systems reveal that NMN can improve oxidative stress conditions and enhance steroid production/hormone secretion, suggesting its potential application in maintaining reproductive cell metabolic homeostasis.

At the signaling level, the PI3K/AKT/mTOR pathway serves as a central hub regulating cellular growth, metabolism, and stress responses. AKT activation inhibits TSC1/2-mediated mTORC1 activity, thereby promoting protein translation and metabolic reprogramming. Additionally, mTOR drives glucose uptake and lactate production by enhancing HIF-1α expression, which activates glycolytic genes including HK2, PKM2, and LDHA. This pathway becomes particularly crucial under mitochondrial damage or hypoxic/oxidative stress conditions[177]. The PI3K/AKT pathway plays a vital role in ovarian tissue regulation and granulosa cell function. Through this pathway, metabolic processes can be modulated to enhance antioxidant capacity and endocrine functions in granulosa cells.

Based on the above background, we hypothesize that NMN reprograms granulosa cells' energy metabolism by restoring NAD^+ levels and mitochondrial function, thereby activating or influencing the PI3K/AKT/mTOR/HIF-1α axis. This process enhances glycolytic enzyme expression and lactate/pyruvate metabolism while

reducing H_2O_2-induced oxidative damage. To validate this hypothesis, we employ a H_2O_2 modeling system of granulosa cell oxidative stress, comparing: ①control group, ② H_2O_2 group, ③ H_2O_2+NMN group, ④ H_2O_2+NMN+PI3K inhibitors (LY2940 02) group, ⑤ H_2O_2+NMN+AKT inhibitors (MK-2206) group. Western blot with phospho-specific antibodies assesses PI3K and AKT expression/activity (phosphorylation levels), while SOD activity and MDA content are detected along with mitochondrial membrane potential (JC-1), intracellular ROS (DCFH-DA), and key glycolytic enzymes (HK2, PKM2, LDHA). Additionally, lactate and pyruvate levels in culture supernatants, as well as AMH and E_2 secretion from granulosa cells, are measured. If the protective effects of NMN are partially or completely inhibited by LY294002 or MK-2206, this would confirm the central role of the PI3K/AKT/HIF-1α axis in NMN's regulation of granulocyte energy metabolism and antioxidant effects. Recent studies demonstrating NMN's ability to inhibit HIF-1α activation across various cell types, as well as its influence on HIF-1α through the NAD^+ /SIRT1 axis, further support the feasibility of this mechanism[178].

1. Materials and Methods

1.1. Experimental Materials

The commonly used consumables, reagents and instruments for cell culture are shown in Table 11-13 of Chapter V 1.1 Experimental Materials, and the reference antibody for the experiment is shown in Table 3 of Chapter Ⅲ 1.1

1.2. Experimental Methods

The preparation of experimental reagents, cell culture, real-time fluorescent quantitative PCR, immunoprotein blotting, mitochondrial function determination, and the determination of metabolites and sex hormones in the culture supernatant were all referenced to ChaperⅤ 1.2.1. to 1.2.8.

1.2.1. Statistical Analysis

See Chapter Ⅴ 1.2.9

2. Results

2.1. Effects of NMN on the Expression of PI3K/AKT/HIF-1α in KGN induced by Oxidative Stress

To elucidate the signaling pathway by which NMN alleviates oxidative stress-induced damage to ovarian granulosa cells, we analyzed the phosphorylation status of PI3K, AKT, and HIF-1α at both transcriptional and protein levels. The experimental groups included: Ctrl, H_2O_2, H_2O_2+NMN, H_2O_2+NMN+LY294002 (PI3K inhibitor), and H_2O_2+NMN+MK2206(AKT inhibitor). Quantitative PCR revealed that H_2O_2 treatment significantly reduced mRNA levels of PI3K, AKT, and HIF-1A compared to the control group (Figure 27A), indicating that oxidative stress suppresses transcriptional activity in this pathway. NMN intervention markedly elevated mRNA expression of all three proteins, showing significant differences from the H_2O_2 group. When PI3K inhibitor LY294002 or AKT inhibitor MK2206 was added, NMN's enhancement of PI3K/AKT/HIF-1 α transcription was partially or completely counteracted, with results similar to those in the H_2O_2 group but lacking statistically significant differences.

Western blot analysis revealed a slight decrease in PI3K and AKT levels in the H_2O_2 group, with significant reductions in p-PI3K (Tyr/Ser site, as per kit instructions) and p-AKT (Ser473/Thr308), leading to a decreased p-PI3K/PI3K/p-AKT/AKT ratio (Figure 27B). NMN intervention significantly restored the phosphorylation levels of PI3K and AKT. After adding LY294002, p-PI3K/PI3K and its downstream p-AKT/AKT showed a marked decrease again. When MK2206 was added, p-AKT/AKT was significantly inhibited while p-PI3K/PI3K showed minimal effect, consistent with the specificity of the inhibitors.

Regarding HIF-1α protein expression, the H_2O_2 group showed reduced HIF-1α protein levels, indicating that inhibition of the PI3K/AKT pathway under oxidative stress affects HIF-1α stability. NMN significantly upregulates HIF-1α. However, after intervention with LY294002 or MK2206, the elevated HIF-1α was markedly weakened, suggesting NMN's restorative effect on HIF-1α depends on PI3K/AKT activation. Under ionizing radiation or chemical oxidative stress, granular cells exhibit suppressed PI3K/AKT pathways accompanied by HIF-1α downregulation. NMN restores PI3K and AKT phosphorylation by enhancing NAD^+ related signaling homeostasis, thereby promoting HIF-1α expression. This upstream signaling mechanism provides an explanation for NMN's previously observed antioxidant effects and maintenance of glycolytic and mitochondrial functions. Specific inhibition of PI3K or AKT reverses NMN's protective effects, further validating the critical role of this pathway in NMN's action.

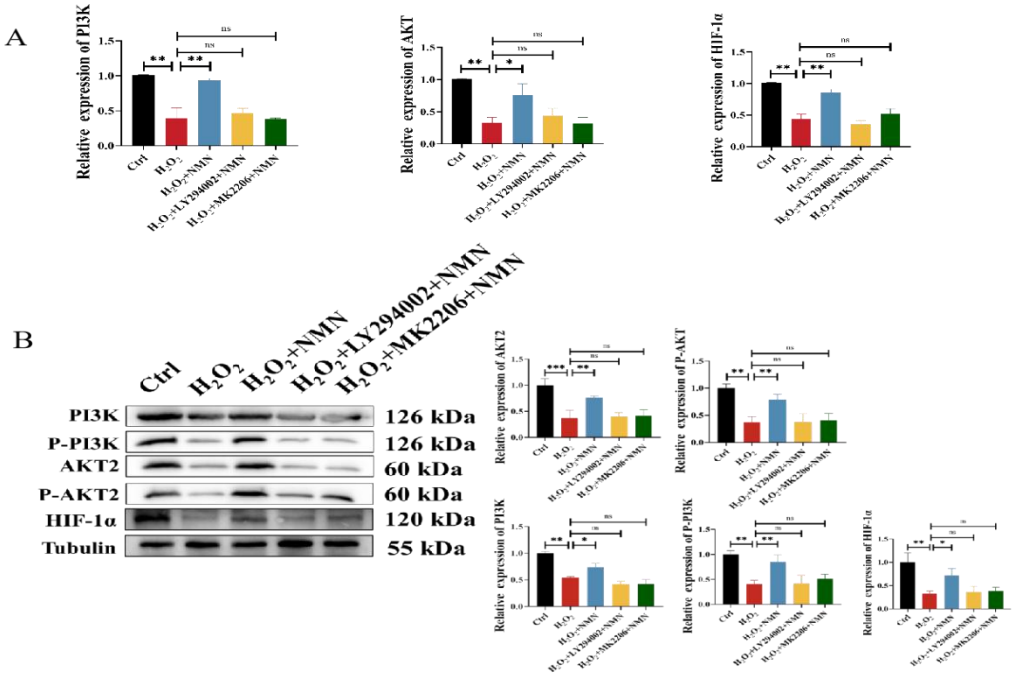

Figure 27. NMN upregulates HIF-1α by activating the PI3K/AKT pathway to relieve H_2O_2 induced KGN signal inhibition (n=3)

(A) The relative expression of PI3K, AKT and HIF-1α mRNA in qPCR was significantly decreased in H_2O_2 group; the expression increased after NMN intervention; and the increase of NMN was weakened after adding inhibitors. (B) Western blot detection of p-PI3K, PI3K, p-AKT, AKT, HIF-1α; β-tubulin as an internal reference.Expression of p-PI3K, p-AKT, and HIF-1α in the H_2O_2 group. H_2O_2 reduced phosphorylation and HIF-1α; NMN significantly restored these levels; LY294002 primarily inhibited p-PI3K, subsequently decreasing p-AKT and HIF-1α; MK2206 selectively inhibited p-AKT while reducing HIF-1α. Data are expressed as mean±standard deviation (mean±SD), n=3; *p<0.05, **p<0.01, ***P <0.001

2.2. NMN Improves Oxidative Stress Levels in KGN through PI3K/AKT/HIF-1α Pathway

To investigate the role of the PI3K/AKT/HIF-1α pathway in NMN's antioxidant effects, we measured four oxidative stress/antioxidant biomarkers: SOD, MDA, CAT, and T-GSH/GSSG. In the H_2O_2 group, decreased SOD, CAT, and T-GSH/GSSG levels were accompanied by elevated MDA, with NMN significantly reversing these changes. When PI3K or AKT was specifically inhibited, NMN's beneficial effects were partially offset. This functional-level evidence supports NMN's regulation of the PI3K/AKT/HIF-1α signaling pathway, thereby modulating cellular antioxidant networks.

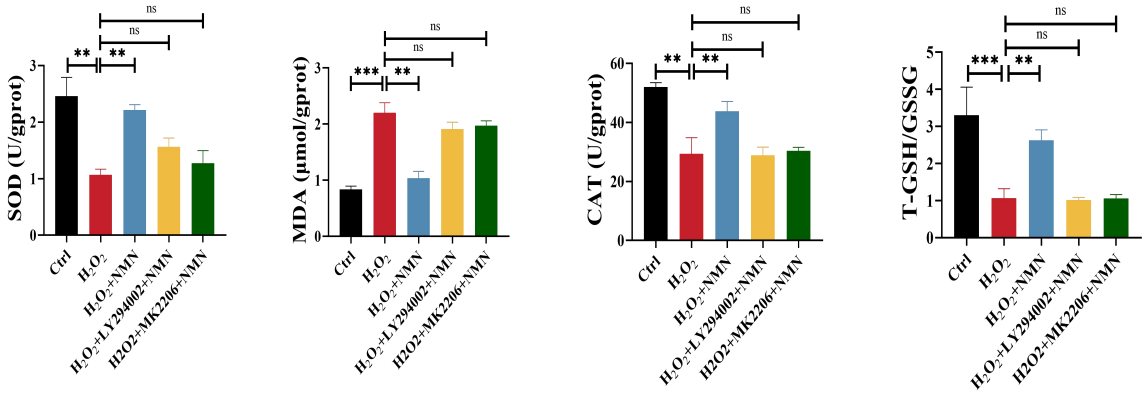

Figure 28. NMN alleviates H_2O_2 induced oxidative stress in granular cells by regulating PI3K/AKT/HIF-1α signaling pathway

The colorimetric method was used to detect SOD activity, MDA content, CAT activity, and the T-GSH/GSSG ratio. The H_2O_2 group showed decreased SOD and CAT activity along with

elevated MDA levels (indicating lipid peroxidation), while NMN demonstrated significant improvement. When LY294002 or MK2206 were added, NMN's protective effects were partially reversed. Data are presented as mean ± standard deviation (n=3), with **p<0.01 and ***P <0.001.

2.3. Effects of NMN on Mitochondrial Function of KGN induced by Oxidative Stress through PI3K/AKT pathway

Detect mitochondrial integrity

To investigate whether the protective effects of NMN on oxidative stress-induced mitochondrial dysfunction in KGN depend on the PI3K/AKT signaling pathway, we assessed $\Delta\psi m$ by JC-1 staining and intracellular ROS levels by DCFH-DA staining. About Mitochondrial membrane potential (JC-1). Control (Ctrl): Predominant red fluorescence (JC-1 aggregates) with a high red/green ratio, indicating intact $\Delta\psi m$. H_2O_2 group: Increased green monomer fluorescence and reduced red aggregates, with a decreased red/green ratio, suggesting mitochondrial depolarization. H_2O_2+NMN group: Restored red fluorescence and reduced green fluorescence, resulting in a significantly higher red/green ratio, indicating $\Delta\psi m$ recovery. H_2O_2+NMN+LY294002 and H_2O_2+NMN+MK2206 groups: Red fluorescence declined and green fluorescence increased compared with the NMN group, demonstrating that PI3K or AKT inhibition attenuated NMN′ s protective effect. CCCP group: Nearly complete depolarization with strong green and minimal red fluorescence, serving as a positive control. About ROS levels (DCFH-DA). Control: Weak green fluorescence, indicating low basal ROS. H_2O_2 group: Strong green fluorescence, reflecting elevated ROS. H_2O_2+NMN group: Reduced green fluorescence, suggesting that NMN effectively suppressed oxidative stress. H_2O_2+NMN+LY294002 and H_2O_2+NMN+MK2206 groups: Stronger green fluorescence compared with NMN alone, indicating partial loss of antioxidant protection after PI3K or AKT inhibition. ROS up group: The strongest green fluorescence, confirming assay reliability as a positive control. In summery, NMN

significantly restored Δψm and reduced ROS accumulation in oxidative stress conditions, whereas PI3K/AKT inhibition partially abrogated these effects, indicating that NMN's mitochondrial protective effects depend on activation of the PI3K/AKT pathway.

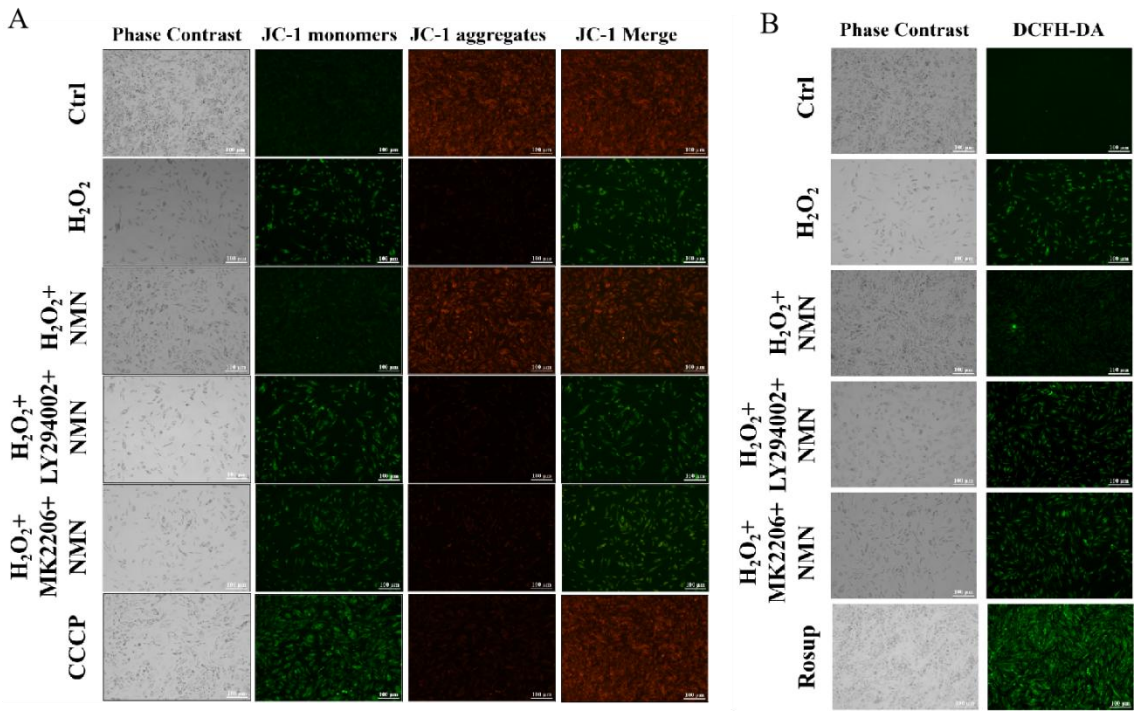

Figure 29. NMN improves oxidative stress induced mitochondrial dysfunction in granular cells through PI3K/AKT pathway

(A) JC-1 staining: Red indicates high Δψm, green represents monomeric fluorescence indicates low Δψm. The red-to-green ratio decreases in H_2O_2 group, NMN intervention restores Δψm, and NMN efficacy is partially lost after adding PI3K and AKT inhibitors.
(B) DCFH-DA staining: Green fluorescence reflects cellular ROS levels. The H_2O_2 group showed elevated ROS, while NMN significantly reduced ROS. PI3K and AKT inhibitors weakened NMN's antioxidant effect; the Rosup group exhibited the strongest fluorescence. Scale bar: 100μm.

Detect mitochondrial enzyme activity

In order to further evaluate the protective effect of NMN on mitochondrial function of granular cells under oxidative stress through PI3K/AKT signaling pathway, we used a colorimetric kit to measure the content of ATP and Ca^{2+} /Mg^{2}-ATPase activity reflecting mitochondrial function in each group.

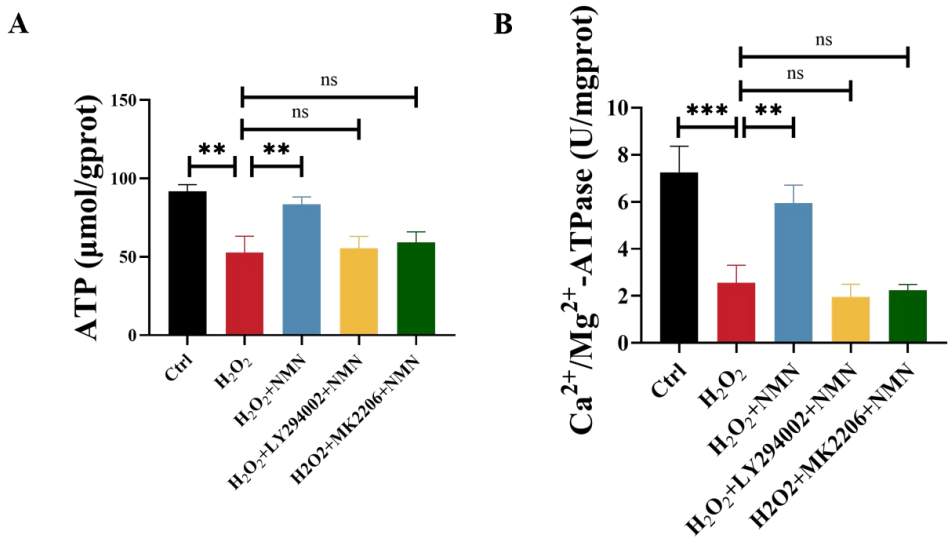

Figure 30. NMN improves oxidative stress induced mitochondrial ATP content and ATPase activity in KGN cells through PI3K/AKT pathway

（A）The content of ATP in each group decreased in H_2O_2 group, and NMN group significantly recovered. PI3K and AKT inhibitors weakened the effect of NMN repair.

（B）Na^+ /K^+ -ATPase activity assay: The H_2O_2 group showed a decrease, while the NMN group demonstrated significant recovery. The inhibitor weakened NMN's restorative effects, yielding results comparable to the H_2O_2 group. Data are presented as mean ± standard deviation (n=3). Significant differences are marked by **p<0.01, ***p<0.001, and ns denotes no statistically significant difference.

2.4. Effects of NMN on Glycolysis of KGN cells Induced by Oxidative Stress through PI3K/AKT pathway

To determine whether NMN regulates granular cell glycolysis under oxidative stress through PI3K/AKT/HIF-1α signaling, we measured mRNA and protein levels of HK2, PKM2, and LDHA across five groups: control, H_2O_2, H_2O_2+NMN, H_2O_2+NMN+LY294002(PI3K inhibitor), and H_2O_2+NMN+MK2206(AKT inhibitor). Transcriptional analysis (qPCR) revealed that H_2O_2 significantly reduced HK2, PKM2, and LDHA mRNA levels compared to the control. NMN pre-treatment significantly upregulated these three enzymes, restoring them to near-control levels. However, the effects of NMN on these glycolytic key enzyme genes were partially or significantly counteracted by the addition of LY294002 or MK2206, indicating that this effect depends on intact PI3K/AKT signaling (Figure 31A). Western blot analysis

showed reduced protein expression of HK2, PKM2, and LDHA in H_2O_2, with NMN significantly restoring these levels. When combined with LY294002 or MK2206, however, protein expression of these three glycolytic enzymes decreased again compared to the NMN-only intervention group, consistent with qPCR trends. The internal reference Tubulin remained stable. Quantitative results showed consistent band intensities (Figure 31B). Overall, the inhibition of key enzymes in oxidative stress that regulate granulocyte glycolysis, from upstream enzyme HK2 to PKM2 and through the lactate-producing LDHA in the glycolytic pathway. Suggests impaired glycolytic flux. NMN simultaneously restores expression of key enzymes at both transcriptional and translational levels. However, PI3K/AKT inhibitors weaken NMN's rescue effects, supporting the functional chain from NMN → PI3K/AKT → HIF-1α → activation of glycolytic genes.

Based on the metabolic and mitochondrial function results, we concluded that NMN maintains glycolytic substrates and energy by sustaining glycolysis. To further evaluate NMN's effects on glycolytic product formation under oxidative stress, we measured pyruvate and lactate levels in cell culture supernatants (Figures 32A, B). Regarding pyruvate content: The H_2O_2 group showed significantly higher pyruvate levels compared to the control, indicating oxidative stress-induced accumulation of glycolytic intermediates. In the H_2O_2+NMN group, pyruvate levels decreased markedly compared to the H_2O_2 group ($p<0.01$) and approached control levels, suggesting NMN alleviates abnormal metabolic disruption. In the H_2O_2+ NMN+LY294002 or MK2206 group, pyruvate levels increased again compared to the NMN intervention group, indicating PI3K/AKT inhibitors weakened NMN's regulatory effect on pyruvate accumulation. Further analysis of lactate levels showed: The H_2O_2 group exhibited significantly reduced lactate levels, suggesting impaired end-glycolysis metabolism. The H_2O_2 + NMN group demonstrated restored lactate levels approaching control levels, indicating NMN promotes end-glycolysis product formation. In the H_2O_2+NMN+LY294002 or H_2O_2+NMN+MK2206 group, lactate

levels decreased significantly compared to the H_2O_2+NMN group, demonstrating NMN's metabolic protective effect depends on intact PI3K/AKT signaling pathway integrity. Oxidative stress disrupts glycolysis, leading to pyruvate accumulation and reduced lactate production. NMN effectively restores the balance of end-product formation in glycolysis. However, inhibitors of PI3K or AKT partially or completely neutralize this metabolic protective effect. The results demonstrate that NMN maintains glycolytic flux through the PI3K/AKT signaling pathway, thereby preventing impaired energy metabolism and supply while mitigating oxidative stress-induced cellular dysfunction and apoptosis.

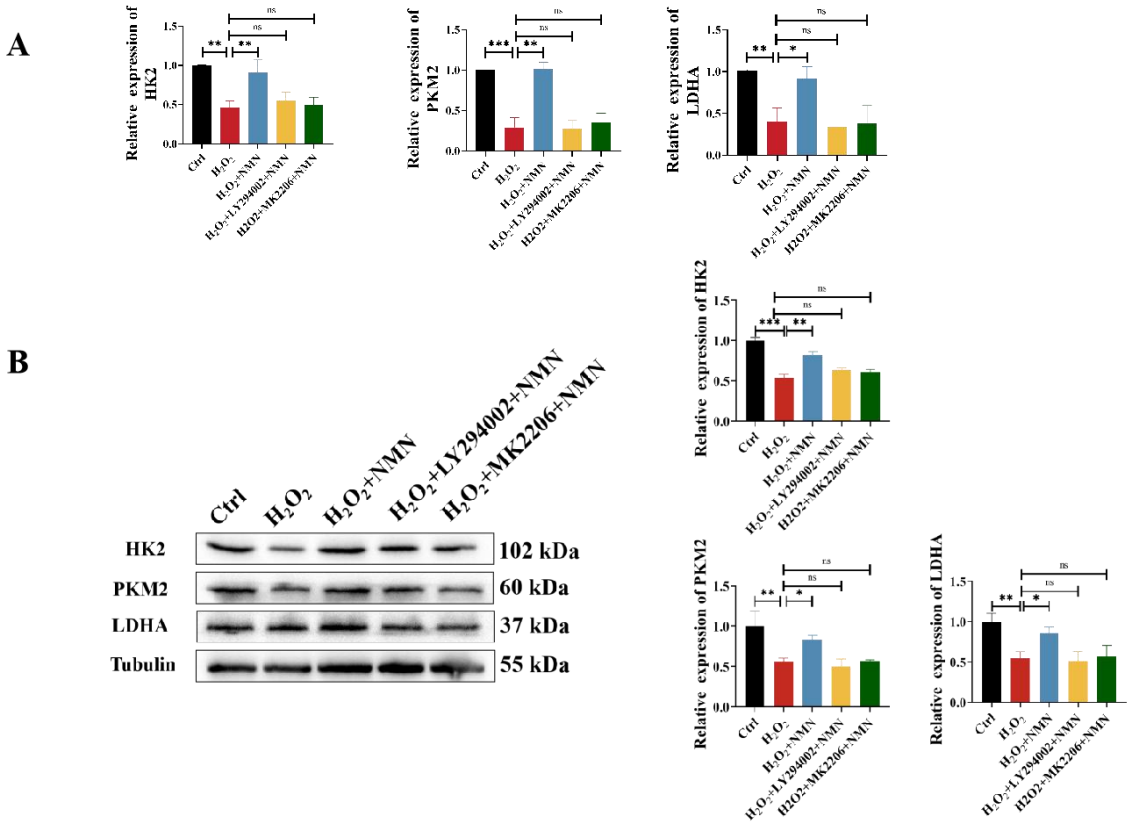

Figure 31. NMN restores the expression of key enzymes of glycolysis in granular cells under oxidative stress through PI3K/AKT pathway

(A) Relative mRNA expression levels of HK2, PKM2, and LDHA were detected by qPCR. The H_2O_2 group showed significantly decreased expression, while the NMN group exhibited a marked increase. The upregulation effect of NMN was partially or completely reversed when LY294002 or MK2206 was added.

(B) Western blot representative bands: HK2, PKM2, LDHA, with tubulin as the internal reference. The gray-scale quantification of bands aligns with qPCR results: The protein expression of three key glycolytic enzymes decreased in H_2O_2 group, while NMN group showed similar recovery to the control group. However, PI3K or AKT inhibition weakened the NMN effect. Expression levels were comparable to those in H_2O_2 group.

Data were expressed as mean ± SD (n=3); *p<0.05, **p<0.01, ns no statistical difference.

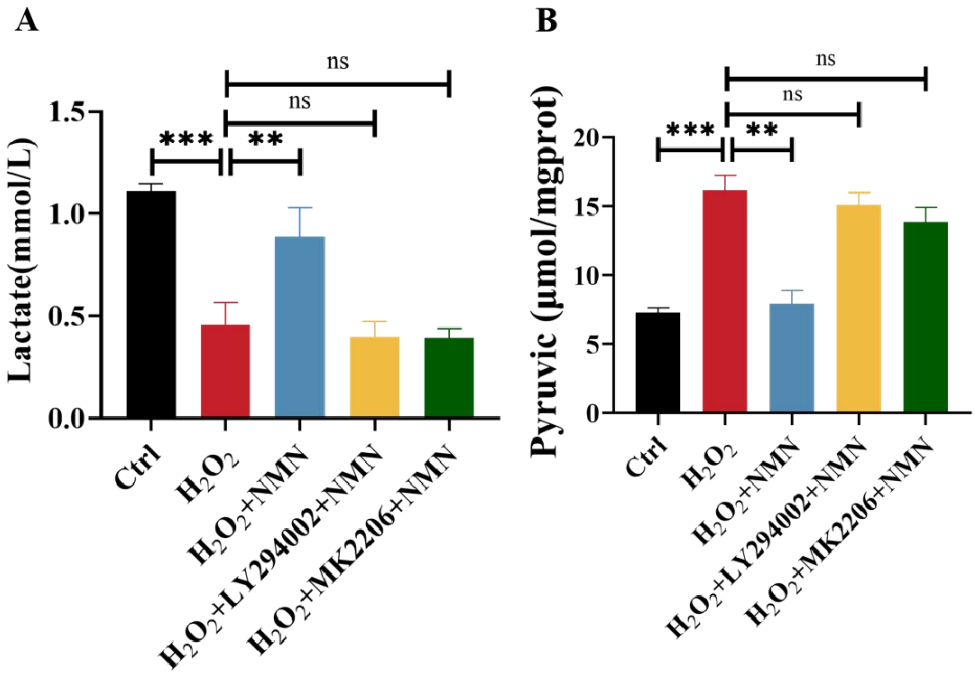

Figure 32. NMN regulates the level of glycolytic metabolites in granular cells under oxidative stress through PI3K/AKT pathway

(A) Pyruvate content: H_2O_2 treatment led to a significant increase in pyruvate, NMN intervention decreased it, and PI3K/AKT inhibitors weakened the effect of NMN.
(B) Lactic acid content: H_2O_2 treatment significantly reduced the level of lactic acid, NMN intervention significantly restored it; after inhibitor intervention, lactic acid production decreased again. Data are expressed as mean ± SD (n=3); **p <0.05, ***p <0.01 indicate significant differences.

2.5. NMN Induces Granulocyte Hormone Secretion Level induced by Oxidative Stress through PI3K/AKT Pathway

This study employed ELISA to measure AMH and E_2 levels in cell culture supernatants across experimental groups. Analysis revealed that H_2O_2 group exhibited significantly reduced AMH levels compared to the control group, indicating oxidative stress-induced impairment of granulosa cell secretion and follicular reserve. The H_2O_2+NMN group demonstrated markedly elevated AMH levels approaching baseline values, demonstrating NMN's capacity to restore granulosa cell hormone secretion. However, both H_2O_2+NMN+LY294002 and H_2O_2+NMN+MK2206 groups

showed significantly lower AMH levels than the NMN group, suggesting that PI3K or AKT inhibitors partially or completely compromised NMN's protective effects.

Continuing to monitor E_2 levels, we observed a significant decrease in E_2 levels in the H_2O_2 group compared to the Ctrl group, indicating that oxidative stress inhibits granulosa cell endocrine function and affects follicular development support. The H_2O_2+NMN group showed significantly higher E_2 levels than the H_2O_2 group, suggesting NMN can restore estrogen synthesis function. The H_2O_2+NMN+LY294002 and H_2O_2+NMN+MK2206 groups exhibited lower E_2 levels than the NMN group, indicating that the pathway plays a key role in NMN's protective effect on E_2 synthesis.

In conclusion, oxidative stress in granulosa cells impairs their endocrine function, with significant decreases in AMH and E_2 levels indicating suppressed ovarian reserve and sex hormone synthesis. NMN intervention restores these hormone levels, while PI3K/AKT inhibitors significantly diminish NMN's protective effects. This further supports NMN's maintenance of granulosa cell endocrine function through the pathway.

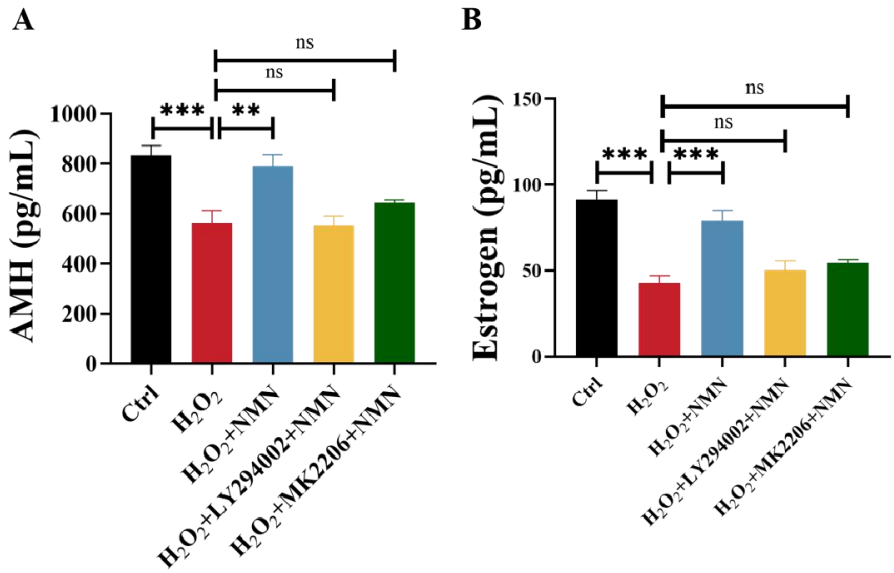

Figure 33. NMN restores KGN cell secretion function under oxidative stress through PI3K/AKT/HIF-1α pathway

(A) AMH content: H_2O_2 group significantly decreased AMH level; NMN intervention restored AMH content; after the addition of LY294002 or MK2206, NMN effect was partially or completely lost.
(B) E_2 content: E_2 production decreased significantly in H_2O_2 group; the use of NMN significantly restored E_2 level; PI3K or AKT inhibition weakened the protective effect of NMN.
The data were expressed as mean ± SD (n=3), **p <0.05, ***p <0.01 indicate significant differences.

3. Discussion

This study employed a hydrogen peroxide-induced ovarian granulosa cell oxidative stress model to systematically evaluate the regulatory effects of NMN and PI3K/AKT signaling pathway inhibitors on granulosa cell oxidative stress status, mitochondrial function, glycolytic metabolism, and secretory functions. The results demonstrated that oxidative stress caused decreased PI3K/AKT signaling activity, accompanied by elevated ROS levels, reduced mitochondrial membrane potential, decreased ATP content and ATPase activity, downregulated expression of key glycolytic enzymes (HK2, PKM2, LDHA), insufficient lactate production, and reduced levels of AMH and estradiol (E_2). These changes reflected severe disruption of energy supply and metabolic homeostasis in granulosa cells, thereby impairing their endocrine and supportive functions. Notably, NMN intervention significantly restored these abnormalities, indicating its crucial role in maintaining energy homeostasis and resisting oxidative damage.

Research has demonstrated that oxidative stress and mitochondrial dysfunction constitute key mechanisms underlying premature ovarian failure and reduced fertility. Through the accumulation of excessive ROS, oxidative stress disrupts mitochondrial membrane potential, and triggers apoptosis pathways[179]. Furthermore, oxidative stress damages key glycolytic enzymes, blocks NAD^+ /NADH metabolism, and exacerbates energy crisis. The findings of this study align closely with this mechanism, further confirming that oxidative stress directly impairs granulosa cell energy metabolism and endocrine function.

As a direct precursor of NAD^+, NMN effectively enhances intracellular NAD^+ levels, activates SIRT1/SIRT3 signaling, and improves mitochondrial function with antioxidant defense[157]. In this study, NMN intervention significantly restored mitochondrial membrane potential, ATP generation, and glycolytic metabolism in granular cells, while enhancing the secretion functions of AMH and E_2. This suggests

that NMN's protective effects are not limited to direct supplementation of NAD^+, but may also stem from reshaping energy metabolism networks and regulating key signaling pathways.

Further inhibition experiments demonstrated that the pathway plays a pivotal role in NMN's protective effects. When PI3K inhibitors LY294002 or AKT inhibitors MK2206 were administered, NMN's protective efficacy was significantly diminished, manifested by reduced antioxidant capacity, impaired glycolytic function, and decreased hormone secretion levels. These findings suggest that NMN may activate the PI3K/AKT/HIF-1α pathway to maintain energy metabolism and mitochondrial function, thereby mitigating oxidative stress damage. Previous studies have established that the PI3K/AKT pathway serves as a critical regulatory hub for glycolytic metabolism and cellular survival, with HIF-1α upregulation enhancing glycolytic enzyme expression and improving energy production efficiency[180]. Therefore, these results provide direct evidence for NMN's mechanism of action.

However, the PI3K/AKT pathway involves complex upstream-downstream networks, and its cross-regulation with mTOR, AMPK, and SIRT signaling pathways requires further investigation. Future studies should integrate multi-omics technologies (transcriptomics, metabolomics, spatial omics) and in vivo animal models to elucidate NMN's multi-level regulatory mechanisms on granulosa cell energy metabolism and oxidative stress responses. Additionally, it is crucial to explore the long-term protective effects of NMN on ovarian function across different dosages and administration windows, thereby evaluating its clinical translational potential.

In conclusion, this study demonstrates that NMN enhances oxidative stress-induced damage in granulosa cells by activating the pathway, thereby improving mitochondrial function and endocrine regulation. This mechanism enables NMN to exert antioxidant and anti-apoptotic effects. The findings provide a novel theoretical foundation and research direction for exploring NMN's potential applications in preventing premature ovarian failure and safeguarding female reproductive health.

4. Summary

In summary, we investigated the effects of NMN and NMN+PI3K/AKT selective inhibitors on PI3K, AKT, HIF-1α, oxidative stress status, mitochondrial function, glycolytic levels, and granulocyte endocrine function in hydrogen peroxide-induced granulocyte oxidative stress models. KGN cells were cultured and treated with drug interventions, divided into five groups: Ctrl, H_2O_2, H_2O_2+NMN, H_2O_2 NMN+LY294002 (PI3K inhibitor), and H_2O_2 +NMN+MK2206 (AKT inhibitor). The study revealed that H_2O_2 group exhibited low levels of PI3K and AKT activity with phosphorylation, elevated oxidative stress, impaired mitochondrial membrane potential, reduced ATP production and activity, decreased expression of glycolytic key enzymes, diminished lactate generation (a terminal glycolytic metabolite), and compromised granulocyte hormone secretion. NMN intervention maintained metabolic homeostasis and energy supply in granulocytes, demonstrating antioxidant and anti-apoptotic effects consistent with our previous findings. Importantly, the use of PI3K and AKT selective inhibitors confirmed that NMN reverses hydrogen peroxide-induced oxidative stress damage in granulocytes and subsequent energy/metabolic impairments through key nodes in the PI3K/AKT signaling pathway.

However, due to the complex network of PI3K/AKT upstream and downstream, we need to further in vivo and in vitro experiments to verify more specific key regulatory nodes. This will also provide ideas for the subsequent clinical application and drug improvement of NMN.

Chapter Ⅶ. Conclusion and prospect

1. Conclusion

This study established a mouse ovarian failure model using cesium-137 γ ray irradiation, systematically elucidating the effects of ionizing radiation on ovarian function and their molecular mechanisms. Our findings demonstrate that radiation not only causes weight loss, ovarian weight reduction, depletion of ovarian reserve, disrupted estrous cycles, decreased serum AMH levels, and elevated FSH in mice, but also triggers NAD^+ depletion, increased oxidative stress (SOD reduction and MDA Ⅶelevation), inhibited expression of key glycolytic enzymes, and insufficient lactate and ATP production. These processes ultimately lead to decreased mitochondrial membrane potential and activation of apoptosis programs in granulosa cells, resulting in ovarian granulosa cell dysfunction and oocyte atresia. This series of findings supports the pathological chain hypothesis of ‘oxidative stress-energy metabolism disorder-mitochondrial dysfunction-ovarian granulosa cell apoptosis-ovarian function decline’.

More importantly, this study elucidates the protective role of NMN, a natural precursor of NAD^+, in repairing ovarian radiation damage. Under a combined preventive and therapeutic administration model, NMN significantly restored NAD^+ levels, reduced oxidative stress, improved mitochondrial function, reconstructed glycolytic flux, and activated the PI3K/AKT-HIF-1α signaling pathway. These mechanisms collectively achieved a comprehensive reversal of radiation-induced dysfunction at multiple levels. This suggests that NMN, as a metabolic intervention molecule, holds potential applications in protecting ovarian function and promoting female reproductive health.

In this study, we established a cesium-137 γ ray induced mouse model of ovarian insufficiency and systematically revealed the molecular basis of radiation-induced ovarian dysfunction. We found that irradiation not only reduced body and ovaria weight, impaired follicle reserve, disrupted estrous cycles, and decreased serum AMH

levels, but also caused NAD^+ depletion, increased oxidative stress, downregulation of glycolytic key enzymes (HK2, PKM2, LDHA), and reduced lactate and ATP production, ultimately leading to mitochondrial depolarization, granulosa cell apoptosis, follicular atresia, and ovarian failure. These findings support the pathological cascade of ‘oxidative stress, energy metabolic impairment, mitochondrial apoptosis, ovarian dysfunction’.

Importantly, we confirmed the protective role of NMN against radiation-induced ovarian injury. NMN supplementation restored NAD^+ levels, enhanced glycolytic flux, alleviated oxidative stress, stabilized mitochondrial function, and activated the PI3K/AKT/HIF-1α axis, thereby reversing radiation-induced molecular and metabolic disturbances. These results suggest that NMN holds promise as a metabolic intervention for ovarian protection and female reproductive health.

2. Future Perspectives

Deepening institutional mechanisms

While this study highlights the pivotal role of the PI3K/AKT/HIF-1α axis in NMN's biological effects, the PI3K/AKT signaling network exhibits complex interactions with mTOR, AMPK, FOXO pathways, and potential connections to antioxidant defense systems like Nrf2/Keap1 in response to oxidative stress[181]. Future research should integrate single-cell transcriptomics, spatial transcriptomics, and metabolomics to identify key transcriptional factors and metabolic enzyme targets regulated by NMN. This will clarify NMN's functional roles across different follicular development stages and within the ovarian microenvironment, including interactions with immune cells, endothelial cells, and fibroblasts.

Metabolic network and energy homeostasis research

Given the high interaction between glycolysis and mitochondrial oxidative phosphorylation, we considered to evaluate the dynamic regulatory effect of NMN on energy substrate utilization and redox homeostasis by means of metabolic flow analysis (isotope tracing) and mitochondrial functional omics[182], so as to establish a system model of ‘metabolic network-energy homeostasis-ovarian function’.

Clinical transformation and individualized intervention

The protective effects of NMN observed in animal studies have established its clinical potential, though its pharmacokinetic characteristics, bioavailability, and long-term safety in ovarian function preservation require further validation through higher animal models (including offspring studies) and clinical trials (currently under investigation). Based on the findings of our preclinical studies, NMN has demonstrated a protective effect against IR induced ovarian dysfunction.

Considering the population characteristics and disease spectrum of Sardinia of Italy, we plan to conduct a prospective randomized controlled clinical study among young women (18−45 years) diagnosed with early-stage cervical or rectal cancer who have a clear intention to preserve fertility. Eligible participants will be those who have undergone pelvic radiotherapy(with or without surgical resection of the primary lesion) and have at least one ovary preserved, showing evidence of radiation-induced ovarian insufficiency, defined as AMH < 1.0 ng/mL and antral follicle count (AFC) < 5.

A total of 60 participants will be enrolled and randomly assigned into two groups:

Experimental group (n = 30), oral NMN 600 mg/day starting after completion of radiotherapy for two consecutive months. Control group (n = 30), oral placebo of identical appearance and taste for two months.

After the intervention, changes in ovarian function parameters (AMH and AFC) and the occurrence of adverse events will be compared between the two groups.

The study design has been completed and is currently under review by the institutional ethics committee.

Drug delivery and optimization

Furthermore, exploring synergistic combinations of NMN with antioxidants (e.g., NAC), mitochondrial-targeting drugs(e.g., MitoQ), or reproductive hormone modulators could enhance protective efficacy while reducing dosage requirements [183]. And we should also focus on the development of tissue-targeted delivery technologies (such as lipid nanoparticles, Gal NAc-modified delivery systems) and NMN derivatives to improve their specificity, stability and efficacy in ovarian tissue[184].

In conclusion, this study not only elucidates the key molecular mechanisms underlying ovarian dysfunction caused by ionizing radiation, but also systematically demonstrates the metabolic protective effects of NMN for the first time. Through the integration of transcriptomic analysis and multi-level mechanistic studies, NMN

shows promise as a potential therapeutic strategy for preventing premature ovarian failure and radiation-induced damage. This research provides crucial theoretical foundations for enhancing female fertility protection and advancing clinical translation in reproductive health.

Perspectives:

(1) Mechanistic insights: Given the complex crosstalk among PI3K/AKT, mTOR, AMPK, and FOXO signaling, future work should integrate single-cell and spatial transcriptomics to delineate NMN-regulated targets and hierarchies[181].
(2) Metabolic regulation: Isotope tracing and mitochondrial functional omics will be valuable to map NMN's effects on substrate utilization and redox homeostasis [182].
(3) Clinical translation: Preclinical studies in higher mammals are needed to assess NMN pharmacokinetics, safety, and efficacy, and combinational strategies with antioxidants or mitochondrial-targeted drugs may be explored[183].
(4) Drug optimization: Advances in tissue-specific delivery (e.g., lipid nanoparticles, GalNAc conjugates) and NMN derivatives may further enhance its therapeutic potential[184].

In conclusion, our study not only delineates the molecular mechanisms of radiation-induced ovarian dysfunction but also demonstrates NMN's metabolic protective role. Through multi-omics and mechanistic investigations, NMN may serve as a promising therapeutic strategy for ovarian insufficiency and radiation-induced reproductive disorders, offering translational potential for female reproductive health.

References

[1] A. N. Giaquinto *et al.*, 'Breast cancer statistics 2024', *CA. Cancer J. Clin.*, vol. 74, no. 6, pp. 477–495, 2024, doi: 10.3322/caac.21863.
[2] H. Sung *et al.*, 'Colorectal cancer incidence trends in younger versus older adults: an analysis of population-based cancer registry data', *Lancet Oncol.*, vol. 26, no. 1, pp. 51–63, Jan. 2025, doi: 10.1016/S1470-2045(24)00600-4.
[3] C. Petrini, 'Regulation (EU) No 536/2014 on clinical trials on medicinal products for human use: an overview', *Ann. Ist. Super. Sanita*, vol. 50, no. 4, pp. 317–321, 2014, doi: 10.4415/ANN_14_04_04.
[4] W. A. Peters *et al.*, 'Concurrent Chemotherapy and Pelvic Radiation Therapy Compared With Pelvic Radiation Therapy Alone as Adjuvant Therapy After Radical Surgery in High-Risk Early-Stage Cancer of the Cervix', *J. Clin. Oncol. Off. J. Am. Soc. Clin. Oncol.*, vol. 41, no. 29, pp. 4605–4612, Oct. 2023, doi: 10.1200/JCO.22.02769.
[5] Z. Bunjo and T. Sammour, 'The Landmark Series: Neoadjuvant Therapy for Locally Advanced Rectal Cancer', *Ann. Surg. Oncol.*, vol. 32, no. 7, pp. 4935–4944, Jul. 2025, doi: 10.1245/s10434-025-17299-5.
[6] K. Sato *et al.*, 'Impact of young age on local control after partial breast irradiation in Japanese patients with early stage breast cancer', *Breast Cancer Tokyo Jpn.*, vol. 24, no. 1, pp. 79–85, Jan. 2017, doi: 10.1007/s12282-016-0669-4.
[7] D. V. Nguyen *et al.*, 'Local Recurrence in Young Women with Breast Cancer: Breast Conserving Therapy vs. Mastectomy Alone', *Cancers*, vol. 13, no. 9, p. 2150, Apr. 2021, doi: 10.3390/cancers13092150.
[8] J.-T. Kim *et al.*, 'Treatment With Tissue Plasminogen Activator in the Golden Hour and the Shape of the 4.5-Hour Time-Benefit Curve in the National United States Get With The Guidelines-Stroke Population', *Circulation*, vol. 135, no. 2, pp. 128–139, Jan. 2017, doi: 10.1161/CIRCULATIONAHA.116.023336.
[9] R. Baskar, K. A. Lee, R. Yeo, and K.-W. Yeoh, 'Cancer and radiation therapy: current advances and future directions', *Int. J. Med. Sci.*, vol. 9, no. 3, pp. 193–199, 2012, doi: 10.7150/ijms.3635.
[10] D. Meirow and D. Nugent, 'The effects of radiotherapy and chemotherapy on female reproduction', *Hum. Reprod. Update*, vol. 7, no. 6, pp. 535–543, 2001, doi: 10.1093/humupd/7.6.535.
[11] W. H. B. Wallace, A. B. Thomson, F. Saran, and T. W. Kelsey, 'Predicting age of ovarian failure after radiation to a field that includes the ovaries', *Int. J. Radiat. Oncol. Biol. Phys.*, vol. 62, no. 3, pp. 738–744, Jul. 2005, doi: 10.1016/j.ijrobp.2004.11.038.
[12] E. Reiser *et al.*, 'Unlaid Eggs: Ovarian Damage after Low-Dose Radiation', *Cells*, vol. 11, no. 7, p. 1219, Apr. 2022, doi: 10.3390/cells11071219.
[13] O. Oktem and K. Oktay, 'Quantitative assessment of the impact of chemotherapy on ovarian follicle reserve and stromal function', *Cancer*, vol. 110, no. 10, pp. 2222–2229, Nov. 2007, doi: 10.1002/cncr.23071.
[14] E. J. Chow *et al.*, 'Pregnancy after chemotherapy in male and female survivors of childhood cancer treated between 1970 and 1999: a report from the Childhood Cancer Survivor Study cohort', *Lancet Oncol.*, vol. 17, no. 5, pp. 567–576, May 2016, doi: 10.1016/S1470-2045(16)00086-3.
[15] Y. Guo *et al.*, 'High-level expression and characterization of a novel aspartic protease from Talaromyces leycettanus JCM12802 and its potential application in juice clarification', *Food Chem.*, vol. 281, pp. 197–203, May 2019, doi: 10.1016/j.foodchem.2018.12.096.
[16] F. J. M. Broekmans, D. de Ziegler, C. M. Howles, A. Gougeon, G. Trew, and F. Olivennes, 'The antral follicle count: practical recommendations for better standardization', *Fertil. Steril.*, vol. 94, no. 3, pp. 1044–1051, Aug. 2010, doi: 10.1016/j.fertnstert.2009.04.040.
[17] A. Templeton, A. Bodnar, S. I. Gan, S. Irani, A. Ross, and D. Low, 'Occurrence of invasive cancer after endoscopic treatment of Barrett's esophagus with high-grade dysplasia and intramucosal cancer in physiologically fit patients: time for a review of

surveillance and treatment guidelines', *Gastrointest. Endosc.*, vol. 79, no. 5, pp. 839–844, May 2014, doi: 10.1016/j.gie.2013.11.024.
[18] Z. W. Castillo and M. D. Burton, 'Utilizing multiphoton imaging and integrative clearing to reveal sex differences in neuroimmune interactions after nerve injury', *Neural Regen. Res.*, vol. 17, no. 11, pp. 2429–2430, Nov. 2022, doi: 10.4103/1673-5374.335809.
[19] F. J. Broekmans, J. Kwee, D. J. Hendriks, B. W. Mol, and C. B. Lambalk, 'A systematic review of tests predicting ovarian reserve and IVF outcome', *Hum. Reprod. Update*, vol. 12, no. 6, pp. 685–718, 2006, doi: 10.1093/humupd/dml034.
[20] R. O. Bahado-Singh *et al.*, 'Fetal male gender and the benefits of treatment of mild gestational diabetes mellitus', *Am. J. Obstet. Gynecol.*, vol. 206, no. 5, p. 422.e1–5, May 2012, doi: 10.1016/j.ajog.2012.03.015.
[21] W. H. B. Wallace, A. B. Thomson, and T. W. Kelsey, 'The radiosensitivity of the human oocyte', *Hum. Reprod. Oxf. Engl.*, vol. 18, no. 1, pp. 117–121, Jan. 2003, doi: 10.1093/humrep/deg016.
[22] D. Meirow and D. Nugent, 'The effects of radiotherapy and chemotherapy on female reproduction', *Hum. Reprod. Update*, vol. 7, no. 6, pp. 535–543, 2001, doi: 10.1093/humupd/7.6.535.
[23] L. T. Shuster, D. J. Rhodes, B. S. Gostout, B. R. Grossardt, and W. A. Rocca, 'Premature menopause or early menopause: long-term health consequences', *Maturitas*, vol. 65, no. 2, pp. 161–166, Feb. 2010, doi: 10.1016/j.maturitas.2009.08.003.
[24] T. R. Smith, J. P. Drozda, J. A. Vanslette, A. S. Hoeffken, and R. A. Nicholson, 'Medication class effects on visit-to-visit variability of blood pressure measurements: analysis of electronic health record data in the "real world"', *J. Clin. Hypertens. Greenwich Conn*, vol. 15, no. 9, pp. 655–662, Sep. 2013, doi: 10.1111/jch.12165.
[25] S. Palomba, P. Affinito, G. A. Tommaselli, and C. Nappi, 'A clinical trial of the effects of tibolone administered with gonadotropin-releasing hormone analogues for the treatment of uterine leiomyomata', *Fertil. Steril.*, vol. 70, no. 1, pp. 111–118, Jul. 1998, doi: 10.1016/s0015-0282(98)00128-9.
[26] C. M. Seymen, S. Tuncer, M. Suhan Ayhan, and C. Elmas, 'Botulinum Toxin Type A: Assessing The Effects on The Brain Stem', *Aesthetic Plast. Surg.*, vol. 42, no. 2, pp. 538–545, Apr. 2018, doi: 10.1007/s00266-018-1092-3.
[27] C. Beyrer and A. Pozniak, 'HIV Drug Resistance - An Emerging Threat to Epidemic Control', *N. Engl. J. Med.*, vol. 377, no. 17, pp. 1605–1607, Oct. 2017, doi: 10.1056/NEJMp1710608.
[28] C. Beyrer and A. Pozniak, 'HIV Drug Resistance - An Emerging Threat to Epidemic Control', *N. Engl. J. Med.*, vol. 377, no. 17, pp. 1605–1607, Oct. 2017, doi: 10.1056/NEJMp1710608.
[29] Z. Liu, L.-A. Wang, S. Ding, and Y. Li, 'Effects of growth agents and mercury on several herbs', *Environ. Sci. Pollut. Res. Int.*, vol. 25, no. 12, pp. 12012–12021, Apr. 2018, doi: 10.1007/s11356-018-1498-0.
[30] C. A. Stuenkel *et al.*, 'Treatment of Symptoms of the Menopause: An Endocrine Society Clinical Practice Guideline', *J. Clin. Endocrinol. Metab.*, vol. 100, no. 11, pp. 3975–4011, Nov. 2015, doi: 10.1210/jc.2015-2236.
[31] J. A. Cauley *et al.*, 'Effects of estrogen plus progestin on risk of fracture and bone mineral density: the Women's Health Initiative randomized trial', *JAMA*, vol. 290, no. 13, pp. 1729–1738, Oct. 2003, doi: 10.1001/jama.290.13.1729.
[32] J. E. Manson *et al.*, 'Menopausal hormone therapy and health outcomes during the intervention and extended poststopping phases of the Women's Health Initiative randomized trials', *JAMA*, vol. 310, no. 13, pp. 1353–1368, Oct. 2013, doi: 10.1001/jama.2013.278040.
[33] Y. Jin *et al.*, 'Maternal miR-202-5p is required for zebrafish primordial germ cell migration by protecting small GTPase Cdc42', *J. Mol. Cell Biol.*, vol. 12, no. 7, pp. 530–542, Jul. 2020, doi: 10.1093/jmcb/mjz103.
[34] L. Rigo, K. Basso, J. Pauli, G. O. Cericato, L. R. Paranhos, and R. R. Garbin, '[Satisfaction with life, dental experience and self-perception of oral health among the elderly]', *Cienc. Saude Coletiva*, vol. 20, no. 12, pp. 3681–3688, Dec. 2015, doi: 10.1590/1413-812320152012.18432014.

[35] R. J. Santen *et al.*, ‘Postmenopausal hormone therapy: an Endocrine Society scientific statement’, *J. Clin. Endocrinol. Metab.*, vol. 95, no. 7 Suppl 1, pp. s1–s66, Jul. 2010, doi: 10.1210/jc.2009-2509.
[36] M. Frank, S. Adham, F. Zinzindohoué, and X. Jeunemaitre, ‘Natural history of gastrointestinal manifestations in vascular Ehlers-Danlos syndrome: A 17-year retrospective review’, *J. Gastroenterol. Hepatol.*, vol. 34, no. 5, pp. 857–863, May 2019, doi: 10.1111/jgh.14522.
[37] C. Poirier *et al.*, ‘The role of environmental factors on transmission rates of the COVID-19 outbreak: an initial assessment in two spatial scales’, *Sci. Rep.*, vol. 10, no. 1, p. 17002, Oct. 2020, doi: 10.1038/s41598-020-74089-7.
[38] D. Bennett *et al.*, ‘Postoperative acute kidney injury in lung transplant recipients’, *Interact. Cardiovasc. Thorac. Surg.*, vol. 28, no. 6, pp. 929–935, Jun. 2019, doi: 10.1093/icvts/ivy355.
[39] J. Teixeira, H. Gonçalves, N. Ferrand, M. García-París, and E. Recuero, ‘Mitochondrial phylogeography of the Iberian endemic frog Rana iberica, with implications for its conservation’, *Curr. Zool.*, vol. 64, no. 6, pp. 755–764, Dec. 2018, doi: 10.1093/cz/zoy010.
[40] D. Bennett *et al.*, ‘Postoperative acute kidney injury in lung transplant recipients’, *Interact. Cardiovasc. Thorac. Surg.*, vol. 28, no. 6, pp. 929–935, Jun. 2019, doi: 10.1093/icvts/ivy355.
[41] D. Meirow and D. Nugent, ‘The effects of radiotherapy and chemotherapy on female reproduction’, *Hum. Reprod. Update*, vol. 7, no. 6, pp. 535–543, 2001, doi: 10.1093/humupd/7.6.535.
[42] J. J. Eppig, ‘Oocyte control of ovarian follicular development and function in mammals’, *Reprod. Camb. Engl.*, vol. 122, no. 6, pp. 829–838, Dec. 2001, doi: 10.1530/rep.0.1220829.
[43] D. L. Russell and R. L. Robker, ‘Molecular mechanisms of ovulation: co-ordination through the cumulus complex’, *Hum. Reprod. Update*, vol. 13, no. 3, pp. 289–312, 2007, doi: 10.1093/humupd/dml062.
[44] R. G. Bartlett, H. F. Brubach, and H. Specht, ‘Demonstration of aventilatory mass flow during ventilation and apnea in man’, *J. Appl. Physiol.*, vol. 14, no. 1, pp. 97–101, Jan. 1959, doi: 10.1152/jappl.1959.14.1.97.
[45] J. M. Young and A. S. McNeilly, ‘Theca: the forgotten cell of the ovarian follicle’, *Reprod. Camb. Engl.*, vol. 140, no. 4, pp. 489–504, Oct. 2010, doi: 10.1530/REP-10-0094.
[46] K. Sugiura, F. L. Pendola, and J. J. Eppig, ‘Oocyte control of metabolic cooperativity between oocytes and companion granulosa cells: energy metabolism’, *Dev. Biol.*, vol. 279, no. 1, pp. 20–30, Mar. 2005, doi: 10.1016/j.ydbio.2004.11.027.
[47] M. L. Sutton-McDowall, R. B. Gilchrist, and J. G. Thompson, ‘The pivotal role of glucose metabolism in determining oocyte developmental competence’, *Reprod. Camb. Engl.*, vol. 139, no. 4, pp. 685–695, Apr. 2010, doi: 10.1530/REP-09-0345.
[48] R. B. Gilchrist, M. Lane, and J. G. Thompson, ‘Oocyte-secreted factors: regulators of cumulus cell function and oocyte quality’, *Hum. Reprod. Update*, vol. 14, no. 2, pp. 159–177, 2008, doi: 10.1093/humupd/dmm040.
[49] T. S. Hussein, D. A. Froiland, F. Amato, J. G. Thompson, and R. B. Gilchrist, ‘Oocytes prevent cumulus cell apoptosis by maintaining a morphogenic paracrine gradient of bone morphogenetic proteins’, *J. Cell Sci.*, vol. 118, no. Pt 22, pp. 5257–5268, Nov. 2005, doi: 10.1242/jcs.02644.
[50] D. F. Albertini, C. M. Combelles, E. Benecchi, and M. J. Carabatsos, ‘Cellular basis for paracrine regulation of ovarian follicle development’, *Reprod. Camb. Engl.*, vol. 121, no. 5, pp. 647–653, May 2001, doi: 10.1530/rep.0.1210647.
[51] R. B. Gilchrist and J. G. Thompson, ‘Oocyte maturation: emerging concepts and technologies to improve developmental potential in vitro’, *Theriogenology*, vol. 67, no. 1, pp. 6–15, Jan. 2007, doi: 10.1016/j.theriogenology.2006.09.027.
[52] F. Matsuda, N. Inoue, N. Manabe, and S. Ohkura, ‘Follicular growth and atresia in mammalian ovaries: regulation by survival and death of granulosa cells’, *J. Reprod. Dev.*, vol. 58, no. 1, pp. 44–50, 2012, doi: 10.1262/jrd.2011-012.

[53] S. Franks, J. Stark, and K. Hardy, ‘Follicle dynamics and anovulation in polycystic ovary syndrome’, *Hum. Reprod. Update*, vol. 14, no. 4, pp. 367–378, 2008, doi: 10.1093/humupd/dmn015.
[54] J. J. Eppig, ‘Oocyte control of ovarian follicular development and function in mammals’, *Reprod. Camb. Engl.*, vol. 122, no. 6, pp. 829–838, Dec. 2001, doi: 10.1530/rep.0.1220829.
[55] D. Dewailly *et al.*, ‘The physiology and clinical utility of anti-Mullerian hormone in women’, *Hum. Reprod. Update*, vol. 20, no. 3, pp. 370–385, 2014, doi: 10.1093/humupd/dmt062.
[56] S. C. Juneja, K. J. Barr, G. C. Enders, and G. M. Kidder, ‘Defects in the germ line and gonads of mice lacking connexin43’, *Biol. Reprod.*, vol. 60, no. 5, pp. 1263–1270, May 1999, doi: 10.1095/biolreprod60.5.1263.
[57] W. H. B. Wallace, ‘Oncofertility and preservation of reproductive capacity in children and young adults’, *Cancer*, vol. 117, no. 10 Suppl, pp. 2301–2310, May 2011, doi: 10.1002/cncr.26045.
[58] M. De Vos, J. Smitz, and T. K. Woodruff, ‘Fertility preservation in women with cancer’, *Lancet Lond. Engl.*, vol. 384, no. 9950, pp. 1302–1310, Oct. 2014, doi: 10.1016/S0140-6736(14)60834-5.
[59] E. Reiser *et al.*, ‘Unlaid Eggs: Ovarian Damage after Low-Dose Radiation’, *Cells*, vol. 11, no. 7, p. 1219, Apr. 2022, doi: 10.3390/cells11071219.
[60] P. J. Devine, S. D. Perreault, and U. Luderer, ‘Roles of reactive oxygen species and antioxidants in ovarian toxicity’, *Biol. Reprod.*, vol. 86, no. 2, p. 27, Feb. 2012, doi: 10.1095/biolreprod.111.095224.
[61] W. H. B. Wallace, A. B. Thomson, F. Saran, and T. W. Kelsey, ‘Predicting age of ovarian failure after radiation to a field that includes the ovaries’, *Int. J. Radiat. Oncol. Biol. Phys.*, vol. 62, no. 3, pp. 738–744, Jul. 2005, doi: 10.1016/j.ijrobp.2004.11.038.
[62] W. H. B. Wallace, A. B. Thomson, and T. W. Kelsey, ‘The radiosensitivity of the human oocyte’, *Hum. Reprod. Oxf. Engl.*, vol. 18, no. 1, pp. 117–121, Jan. 2003, doi: 10.1093/humrep/deg016.
[63] L. T. Shuster, D. J. Rhodes, B. S. Gostout, B. R. Grossardt, and W. A. Rocca, ‘Premature menopause or early menopause: long-term health consequences’, *Maturitas*, vol. 65, no. 2, pp. 161–166, Feb. 2010, doi: 10.1016/j.maturitas.2009.08.003.
[64] E. J. Chow *et al.*, ‘Pregnancy after chemotherapy in male and female survivors of childhood cancer treated between 1970 and 1999: a report from the Childhood Cancer Survivor Study cohort’, *Lancet Oncol.*, vol. 17, no. 5, pp. 567–576, May 2016, doi: 10.1016/S1470-2045(16)00086-3.
[65] D. Meirow and D. Nugent, ‘The effects of radiotherapy and chemotherapy on female reproduction’, *Hum. Reprod. Update*, vol. 7, no. 6, pp. 535–543, 2001, doi: 10.1093/humupd/7.6.535.
[66] R. O. Bahado-Singh *et al.*, ‘Fetal male gender and the benefits of treatment of mild gestational diabetes mellitus’, *Am. J. Obstet. Gynecol.*, vol. 206, no. 5, p. 422.e1–5, May 2012, doi: 10.1016/j.ajog.2012.03.015.
[67] S. Franks, J. Stark, and K. Hardy, ‘Follicle dynamics and anovulation in polycystic ovary syndrome’, *Hum. Reprod. Update*, vol. 14, no. 4, pp. 367–378, 2008, doi: 10.1093/humupd/dmn015.
[68] C. C. S. Chini, J. D. Zeidler, S. Kashyap, G. Warner, and E. N. Chini, ‘Evolving concepts in NAD+ metabolism’, *Cell Metab.*, vol. 33, no. 6, pp. 1076–1087, Jun. 2021, doi: 10.1016/j.cmet.2021.04.003.
[69] S. Imai, ‘Dissecting systemic control of metabolism and aging in the NAD World: the importance of SIRT1 and NAMPT-mediated NAD biosynthesis’, *FEBS Lett.*, vol. 585, no. 11, pp. 1657–1662, Jun. 2011, doi: 10.1016/j.febslet.2011.04.060.
[70] K. F. Mills *et al.*, ‘Long-Term Administration of Nicotinamide Mononucleotide Mitigates Age-Associated Physiological Decline in Mice’, *Cell Metab.*, vol. 24, no. 6, pp. 795–806, Dec. 2016, doi: 10.1016/j.cmet.2016.09.013.
[71] Z. Tan *et al.*, ‘Biosynthesis of β-nicotinamide mononucleotide from glucose via a new pathway in Bacillus subtilis’, *Front. Microbiol.*, vol. 15, p. 1405736, 2024, doi: 10.3389/fmicb.2024.1405736.

[72] X. Tian *et al.*, 'Microbial creation of β-Nicotinamide mononucleotide and its regulation of lipid metabolism in the liver of high-fat diet mice', *Cell Biochem. Funct.*, vol. 42, no. 5, p. e4087, Jul. 2024, doi: 10.1002/cbf.4087.
[73] M. Soma and S. K. Lalam, 'The role of nicotinamide mononucleotide (NMN) in anti-aging, longevity, and its potential for treating chronic conditions', *Mol. Biol. Rep.*, vol. 49, no. 10, pp. 9737–9748, Oct. 2022, doi: 10.1007/s11033-022-07459-1.
[74] W. Hong, F. Mo, Z. Zhang, M. Huang, and X. Wei, 'Nicotinamide Mononucleotide: A Promising Molecule for Therapy of Diverse Diseases by Targeting NAD+ Metabolism', *Front. Cell Dev. Biol.*, vol. 8, p. 246, 2020, doi: 10.3389/fcell.2020.00246.
[75] J. Yoshino, J. A. Baur, and S.-I. Imai, 'NAD+ Intermediates: The Biology and Therapeutic Potential of NMN and NR', *Cell Metab.*, vol. 27, no. 3, pp. 513–528, Mar. 2018, doi: 10.1016/j.cmet.2017.11.002.
[76] J. A. Peters, 'Relaxivity of manganese ferrite nanoparticles', *Prog. Nucl. Magn. Reson. Spectrosc.*, vol. 120–121, pp. 72–94, 2020, doi: 10.1016/j.pnmrs.2020.07.002.
[77] M. Yoshino *et al.*, 'Nicotinamide mononucleotide increases muscle insulin sensitivity in prediabetic women', *Science*, vol. 372, no. 6547, pp. 1224–1229, Jun. 2021, doi: 10.1126/science.abe9985.
[78] X. Xie *et al.*, 'Nicotinamide mononucleotide ameliorates the depression-like behaviors and is associated with attenuating the disruption of mitochondrial bioenergetics in depressed mice', *J. Affect. Disord.*, vol. 263, pp. 166–174, Feb. 2020, doi: 10.1016/j.jad.2019.11.147.
[79] C. Dai *et al.*, 'Increased NAD+ levels protect female mouse reproductive system against zearalenone-impaired glycolysis, lipid metabolism, antioxidant capacity and inflammation', *Reprod. Toxicol. Elmsford N*, vol. 124, p. 108530, Mar. 2024, doi: 10.1016/j.reprotox.2023.108530.
[80] S. Wang *et al.*, 'Glycolysis-Mediated Activation of v-ATPase by Nicotinamide Mononucleotide Ameliorates Lipid-Induced Cardiomyopathy by Repressing the CD36-TLR4 Axis', *Circ. Res.*, vol. 134, no. 5, pp. 505–525, Mar. 2024, doi: 10.1161/CIRCRESAHA.123.322910.
[81] S. M. Nadtochiy, Y. T. Wang, K. Nehrke, J. Munger, and P. S. Brookes, 'Cardioprotection by nicotinamide mononucleotide (NMN): Involvement of glycolysis and acidic pH', *J. Mol. Cell. Cardiol.*, vol. 121, pp. 155–162, Aug. 2018, doi: 10.1016/j.yjmcc.2018.06.007.
[82] K. Yusri, S. Jose, K. S. Vermeulen, T. C. M. Tan, and V. Sorrentino, 'The role of NAD+ metabolism and its modulation of mitochondria in aging and disease', *Npj Metab. Health Dis.*, vol. 3, no. 1, p. 26, Jun. 2025, doi: 10.1038/s44324-025-00067-0.
[83] L. Yi *et al.*, 'The efficacy and safety of β-nicotinamide mononucleotide (NMN) supplementation in healthy middle-aged adults: a randomized, multicenter, double-blind, placebo-controlled, parallel-group, dose-dependent clinical trial', *GeroScience*, vol. 45, no. 1, pp. 29–43, Feb. 2023, doi: 10.1007/s11357-022-00705-1.
[84] J. Liang, F. Huang, Z. Song, R. Tang, P. Zhang, and R. Chen, 'Impact of NAD+ metabolism on ovarian aging', *Immun. Ageing A*, vol. 20, no. 1, p. 70, Dec. 2023, doi: 10.1186/s12979-023-00398-w.
[85] C. Ren *et al.*, 'Exploring nicotinamide adenine dinucleotide precursors across biosynthesis pathways: Unraveling their role in the ovary', *FASEB J. Off. Publ. Fed. Am. Soc. Exp. Biol.*, vol. 38, no. 14, p. e23804, Jul. 2024, doi: 10.1096/fj.202400453R.
[86] A. J. Covarrubias, R. Perrone, A. Grozio, and E. Verdin, 'NAD+ metabolism and its roles in cellular processes during ageing', *Nat. Rev. Mol. Cell Biol.*, vol. 22, no. 2, pp. 119–141, Feb. 2021, doi: 10.1038/s41580-020-00313-x.
[87] E. Verdin, 'NAD^+ in aging, metabolism, and neurodegeneration', *Science*, vol. 350, no. 6265, pp. 1208–1213, Dec. 2015, doi: 10.1126/science.aac4854.
[88] X. A. Cambronne *et al.*, 'Biosensor reveals multiple sources for mitochondrial NAD^+', *Science*, vol. 352, no. 6292, pp. 1474–1477, Jun. 2016, doi: 10.1126/science.aad5168.
[89] T. S. Luongo *et al.*, 'SLC25A51 is a mammalian mitochondrial NAD+ transporter', *Nature*, vol. 588, no. 7836, pp. 174–179, Dec. 2020, doi: 10.1038/s41586-020-2741-7.

[90] N. A. Kolotyeva *et al.*, ‘Pathobiochemistry of Aging and Neurodegeneration: Deregulation of NAD+ Metabolism in Brain Cells’, *Biomolecules*, vol. 14, no. 12, p. 1556, Dec. 2024, doi: 10.3390/biom14121556.
[91] D. C. Levine, K. M. Ramsey, and J. Bass, ‘Circadian NAD(P)(H) cycles in cell metabolism’, *Semin. Cell Dev. Biol.*, vol. 126, pp. 15–26, Jun. 2022, doi: 10.1016/j.semcdb.2021.07.008.
[92] A. Ray Chaudhuri and A. Nussenzweig, ‘The multifaceted roles of PARP1 in DNA repair and chromatin remodelling’, *Nat. Rev. Mol. Cell Biol.*, vol. 18, no. 10, pp. 610–621, Oct. 2017, doi: 10.1038/nrm.2017.53.
[93] M. M. Murata *et al.*, ‘NAD+ consumption by PARP1 in response to DNA damage triggers metabolic shift critical for damaged cell survival’, *Mol. Biol. Cell*, vol. 30, no. 20, pp. 2584–2597, Sep. 2019, doi: 10.1091/mbc.E18-10-0650.
[94] A. Galione, ‘NAADP receptors’, *Cold Spring Harb. Perspect. Biol.*, vol. 3, no. 1, p. a004036, Jan. 2011, doi: 10.1101/cshperspect.a004036.
[95] W. K. Lin *et al.*, ‘Synthesis of the Ca2+-mobilizing messengers NAADP and cADPR by intracellular CD38 enzyme in the mouse heart: Role in β-adrenoceptor signaling’, *J. Biol. Chem.*, vol. 292, no. 32, pp. 13243–13257, Aug. 2017, doi: 10.1074/jbc.M117.789347.
[96] J. Camacho-Pereira *et al.*, ‘CD38 Dictates Age-Related NAD Decline and Mitochondrial Dysfunction through an SIRT3-Dependent Mechanism’, *Cell Metab.*, vol. 23, no. 6, pp. 1127–1139, Jun. 2016, doi: 10.1016/j.cmet.2016.05.006.
[97] X. Gu *et al.*, ‘Nicotinamide Mononucleotide Adenylyl Transferase 2 Inhibition Aggravates Neurological Damage after Traumatic Brain Injury in a Rat Model’, *J. Korean Neurosurg. Soc.*, vol. 66, no. 4, pp. 400–408, Jul. 2023, doi: 10.3340/jkns.2022.0115.
[98] L. Jia, X. An, Y. Liu, and X. Meng, ‘Unveiling the anti-aging of radix saposhnikoviae: A metabolomic study in Drosophila’, *PloS One*, vol. 20, no. 8, p. e0330274, 2025, doi: 10.1371/journal.pone.0330274.
[99] S. Yang, J. H. Park, and H.-C. Lu, ‘Axonal energy metabolism, and the effects in aging and neurodegenerative diseases’, *Mol. Neurodegener.*, vol. 18, no. 1, p. 49, Jul. 2023, doi: 10.1186/s13024-023-00634-3.
[100] A. Kropotov *et al.*, ‘Purine nucleoside phosphorylase controls nicotinamide riboside metabolism in mammalian cells’, *J. Biol. Chem.*, vol. 298, no. 12, p. 102615, Dec. 2022, doi: 10.1016/j.jbc.2022.102615.
[101] J. Dhuguru, R. W. Dellinger, and M. E. Migaud, ‘Defining NAD(P)(H) Catabolism’, *Nutrients*, vol. 15, no. 13, p. 3064, Jul. 2023, doi: 10.3390/nu15133064.
[102] D. Damschroder, R. Zapata-Pérez, K. Richardson, F. M. Vaz, R. H. Houtkooper, and R. Wessells, ‘Stimulating the sir2-spargel axis rescues exercise capacity and mitochondrial respiration in a Drosophila model of Barth syndrome’, *Dis. Model. Mech.*, vol. 15, no. 10, p. dmm049279, Oct. 2022, doi: 10.1242/dmm.049279.
[103] K. M. Pencina *et al.*, ‘Oral MIB-626 (β Nicotinamide Mononucleotide) Safely Raises Blood Nicotinamide Adenine Dinucleotide Levels in Hospitalized Patients With COVID-19 and Acute Kidney Injury: A Randomized Controlled Trial’, *FASEB BioAdvances*, vol. 7, no. 8, p. e70011, Aug. 2025, doi: 10.1096/fba.2025-00014.
[104] J. Unno, K. F. Mills, T. Ogura, M. Nishimura, and S.-I. Imai, ‘Absolute quantification of nicotinamide mononucleotide in biological samples by double isotope-mediated liquid chromatography-tandem mass spectrometry (dimeLC-MS/MS)’, *Npj Aging*, vol. 10, no. 1, p. 2, Jan. 2024, doi: 10.1038/s41514-023-00133-1.
[105] H.-J. Park, S.-G. Yang, J.-H. Shin, S.-B. Yoon, J.-S. Kim, and D.-B. Koo, ‘Nicotinamide mononucleotide biosynthesis and the F-actin cytoskeleton regulate spindle assembly and oocyte maturation quality in post-ovulatory aged porcine oocytes’, *Cell Commun. Signal. CCS*, vol. 23, no. 1, p. 186, Apr. 2025, doi: 10.1186/s12964-025-02200-4.
[106] B. J. Kasperova, A. Cinkajzlova, L. Horvath, P. Svoboda, M. Haluzik, and S. Stemberkova Hubackova, ‘Coming of age: could obesity-related metabolic complications be treated by targeting senescent cells?’, *Front. Cell Dev. Biol.*, vol. 13, p. 1622107, 2025, doi: 10.3389/fcell.2025.1622107.

[107] L. Yi *et al.*, ‘The efficacy and safety of β-nicotinamide mononucleotide (NMN) supplementation in healthy middle-aged adults: a randomized, multicenter, double-blind, placebo-controlled, parallel-group, dose-dependent clinical trial’, *GeroScience*, vol. 45, no. 1, pp. 29–43, Feb. 2023, doi: 10.1007/s11357-022-00705-1.
[108] M. Morifuji, S. Higashi, S. Ebihara, and M. Nagata, ‘Ingestion of β-nicotinamide mononucleotide increased blood NAD levels, maintained walking speed, and improved sleep quality in older adults in a double-blind randomized, placebo-controlled study’, *GeroScience*, vol. 46, no. 5, pp. 4671–4688, Oct. 2024, doi: 10.1007/s11357-024-01204-1.
[109] M. Yoshino *et al.*, ‘Nicotinamide mononucleotide increases muscle insulin sensitivity in prediabetic women’, *Science*, vol. 372, no. 6547, pp. 1224–1229, Jun. 2021, doi: 10.1126/science.abe9985.
[110] B. Liao, Y. Zhao, D. Wang, X. Zhang, X. Hao, and M. Hu, ‘Nicotinamide mononucleotide supplementation enhances aerobic capacity in amateur runners: a randomized, double-blind study’, *J. Int. Soc. Sports Nutr.*, vol. 18, no. 1, p. 54, Jul. 2021, doi: 10.1186/s12970-021-00442-4.
[111] M. Igarashi *et al.*, ‘Chronic nicotinamide mononucleotide supplementation elevates blood nicotinamide adenine dinucleotide levels and alters muscle function in healthy older men’, *Npj Aging*, vol. 8, no. 1, p. 5, May 2022, doi: 10.1038/s41514-022-00084-z.
[112] K. Okabe *et al.*, ‘Oral Administration of Nicotinamide Mononucleotide Is Safe and Efficiently Increases Blood Nicotinamide Adenine Dinucleotide Levels in Healthy Subjects’, *Front. Nutr.*, vol. 9, p. 868640, 2022, doi: 10.3389/fnut.2022.868640.
[113] T. Katayoshi *et al.*, ‘Nicotinamide adenine dinucleotide metabolism and arterial stiffness after long-term nicotinamide mononucleotide supplementation: a randomized, double-blind, placebo-controlled trial’, *Sci. Rep.*, vol. 13, no. 1, p. 2786, Feb. 2023, doi: 10.1038/s41598-023-29787-3.
[114] M. Morifuji, S. Higashi, S. Ebihara, and M. Nagata, ‘Ingestion of β-nicotinamide mononucleotide increased blood NAD levels, maintained walking speed, and improved sleep quality in older adults in a double-blind randomized, placebo-controlled study’, *GeroScience*, vol. 46, no. 5, pp. 4671–4688, Oct. 2024, doi: 10.1007/s11357-024-01204-1.
[115] T. Yamamoto, J. Byun, P. Zhai, Y. Ikeda, S. Oka, and J. Sadoshima, ‘Nicotinamide mononucleotide, an intermediate of NAD+ synthesis, protects the heart from ischemia and reperfusion’, *PloS One*, vol. 9, no. 6, p. e98972, 2014, doi: 10.1371/journal.pone.0098972.
[116] E. F. Fang *et al.*, ‘NAD+ augmentation restores mitophagy and limits accelerated aging in Werner syndrome’, *Nat. Commun.*, vol. 10, no. 1, p. 5284, Nov. 2019, doi: 10.1038/s41467-019-13172-8.
[117] K. Prokopidis, F. Moriarty, G. Bahat, J. McLean, D. D. Church, and H. P. Patel, ‘The Effect of Nicotinamide Mononucleotide and Riboside on Skeletal Muscle Mass and Function: A Systematic Review and Meta-Analysis’, *J. Cachexia Sarcopenia Muscle*, vol. 16, no. 3, p. e13799, Jun. 2025, doi: 10.1002/jcsm.13799.
[118] X. Tu *et al.*, ‘Sarcopenia in systemic sclerosis: prevalence and impact-a systematic review and meta-analysis’, *BMJ Open*, vol. 14, no. 3, p. e078034, Mar. 2024, doi: 10.1136/bmjopen-2023-078034.
[119] K. M. Pencina *et al.*, ‘Oral MIB-626 (β Nicotinamide Mononucleotide) Safely Raises Blood Nicotinamide Adenine Dinucleotide Levels in Hospitalized Patients With COVID-19 and Acute Kidney Injury: A Randomized Controlled Trial’, *FASEB BioAdvances*, vol. 7, no. 8, p. e70011, Aug. 2025, doi: 10.1096/fba.2025-00014.
[120] M. Ahmed, U. Riaz, H. Lv, and L. Yang, ‘A Molecular Perspective and Role of NAD+ in Ovarian Aging’, *Int. J. Mol. Sci.*, vol. 25, no. 9, p. 4680, Apr. 2024, doi: 10.3390/ijms25094680.
[121] M. J. Bertoldo *et al.*, ‘NAD+ Repletion Rescues Female Fertility during Reproductive Aging’, *Cell Rep.*, vol. 30, no. 6, pp. 1670-1681.e7, Feb. 2020, doi: 10.1016/j.celrep.2020.01.058.

[122] Y. Wang *et al.*, ‘β-Nicotinamide Mononucleotide Alleviates Hydrogen Peroxide-Induced Cell Cycle Arrest and Death in Ovarian Granulosa Cells’, *Int. J. Mol. Sci.*, vol. 24, no. 21, p. 15666, Oct. 2023, doi: 10.3390/ijms242115666.
[123] Y. Cai *et al.*, ‘β-Nicotinamide Mononucleotide Reduces Oxidative Stress and Improves Steroidogenesis in Granulosa Cells Associated with Sheep Prolificacy via Activating AMPK Pathway’, *Antioxid. Basel Switz.*, vol. 14, no. 1, p. 34, Dec. 2024, doi: 10.3390/antiox14010034.
[124] Y. Ma *et al.*, ‘Nicotinamide mononucleotide improves the ovarian reserve of POI by inhibiting NLRP3-mediated pyroptosis of ovarian granulosa cells’, *J. Ovarian Res.*, vol. 17, no. 1, p. 236, Nov. 2024, doi: 10.1186/s13048-024-01534-w.
[125] F. Guo, L. Wang, Y. Chen, H. Zhu, X. Dai, and X. Zhang, ‘Nicotinamide Mononucleotide improves oocyte maturation of mice with type 1 diabetes’, *Nutr. Diabetes*, vol. 14, no. 1, p. 23, Apr. 2024, doi: 10.1038/s41387-024-00280-8.
[126] H.-J. Park, S.-G. Yang, J.-H. Shin, S.-B. Yoon, J.-S. Kim, and D.-B. Koo, ‘Nicotinamide mononucleotide biosynthesis and the F-actin cytoskeleton regulate spindle assembly and oocyte maturation quality in post-ovulatory aged porcine oocytes’, *Cell Commun. Signal. CCS*, vol. 23, no. 1, p. 186, Apr. 2025, doi: 10.1186/s12964-025-02200-4.
[127] L. Yi *et al.*, ‘The efficacy and safety of β-nicotinamide mononucleotide (NMN) supplementation in healthy middle-aged adults: a randomized, multicenter, double-blind, placebo-controlled, parallel-group, dose-dependent clinical trial’, *GeroScience*, vol. 45, no. 1, pp. 29–43, Feb. 2023, doi: 10.1007/s11357-022-00705-1.
[128] M. Yoshino *et al.*, ‘Nicotinamide mononucleotide increases muscle insulin sensitivity in prediabetic women’, *Science*, vol. 372, no. 6547, pp. 1224–1229, Jun. 2021, doi: 10.1126/science.abe9985.
[129] G. Sheikhansari, L. Aghebati-Maleki, M. Nouri, F. Jadidi-Niaragh, and M. Yousefi, ‘Current approaches for the treatment of premature ovarian failure with stem cell therapy’, *Biomed. Pharmacother. Biomedecine Pharmacother.*, vol. 102, pp. 254–262, Jun. 2018, doi: 10.1016/j.biopha.2018.03.056.
[130] J. L. Tilly, ‘Ovarian follicle counts--not as simple as 1, 2, 3’, *Reprod. Biol. Endocrinol. RBE*, vol. 1, p. 11, Feb. 2003, doi: 10.1186/1477-7827-1-11.
[131] A. N. Hirshfield and A. R. Midgley, ‘Morphometric analysis of follicular development in the rat’, *Biol. Reprod.*, vol. 19, no. 3, pp. 597–605, Oct. 1978, doi: 10.1095/biolreprod19.3.597.
[132] H. Peters, A. G. Byskov, and J. Grinsted, ‘Follicular growth in fetal and prepubertal ovaries of humans and other primates’, *Clin. Endocrinol. Metab.*, vol. 7, no. 3, pp. 469–485, Nov. 1978, doi: 10.1016/s0300-595x(78)80005-x.
[133] C. Yao *et al.*, ‘Hypo-Hydroxymethylation of Nobox is Associated with Ovarian Dysfunction in Rat Offspring Exposed to Prenatal Hypoxia’, *Reprod. Sci. Thousand Oaks Calif*, vol. 29, no. 5, pp. 1424–1436, May 2022, doi: 10.1007/s43032-022-00866-6.
[134] U. S. Srinivas, B. W. Q. Tan, B. A. Vellayappan, and A. D. Jeyasekharan, ‘ROS and the DNA damage response in cancer’, *Redox Biol.*, vol. 25, p. 101084, Jul. 2019, doi: 10.1016/j.redox.2018.101084.
[135] I. Szumiel, ‘Ionizing radiation-induced oxidative stress, epigenetic changes and genomic instability: the pivotal role of mitochondria’, *Int. J. Radiat. Biol.*, vol. 91, no. 1, pp. 1–12, Jan. 2015, doi: 10.3109/09553002.2014.934929.
[136] S. Banerjee, S. Banerjee, G. Saraswat, S. A. Bandyopadhyay, and S. N. Kabir, ‘Female reproductive aging is master-planned at the level of ovary’, *PloS One*, vol. 9, no. 5, p. e96210, 2014, doi: 10.1371/journal.pone.0096210.
[137] W. H. B. Wallace, A. B. Thomson, and T. W. Kelsey, ‘The radiosensitivity of the human oocyte’, *Hum. Reprod. Oxf. Engl.*, vol. 18, no. 1, pp. 117–121, Jan. 2003, doi: 10.1093/humrep/deg016.
[138] B. F. Kimler, S. M. Briley, B. W. Johnson, A. G. Armstrong, S. Jasti, and F. E. Duncan, ‘Radiation-induced ovarian follicle loss occurs without overt stromal changes’, *Reprod. Camb. Engl.*, vol. 155, no. 6, pp. 553–562, Jun. 2018, doi: 10.1530/REP-18-0089.

[139] Y. Ahmed *et al.*, 'Fertility preservation is an imperative goal in the clinical practice of radiation oncology: a narrative review', *Ecancermedicalscience*, vol. 16, p. 1461, 2022, doi: 10.3332/ecancer.2022.1461.
[140] ESHRE, ASRM, CREWHIRL and IMS Guideline Group on POI *et al.*, 'Evidence-based guideline: Premature Ovarian Insufficiency', *Fertil. Steril.*, vol. 123, no. 2, pp. 221–236, Feb. 2025, doi: 10.1016/j.fertnstert.2024.11.007.
[141] M. J. Bertoldo *et al.*, 'NAD+ Repletion Rescues Female Fertility during Reproductive Aging', *Cell Rep.*, vol. 30, no. 6, pp. 1670-1681.e7, Feb. 2020, doi: 10.1016/j.celrep.2020.01.058.
[142] Y. Ma *et al.*, 'Nicotinamide mononucleotide improves the ovarian reserve of POI by inhibiting NLRP3-mediated pyroptosis of ovarian granulosa cells', *J. Ovarian Res.*, vol. 17, no. 1, p. 236, Nov. 2024, doi: 10.1186/s13048-024-01534-w.
[143] F. Guo, L. Wang, Y. Chen, H. Zhu, X. Dai, and X. Zhang, 'Nicotinamide Mononucleotide improves oocyte maturation of mice with type 1 diabetes', *Nutr. Diabetes*, vol. 14, no. 1, p. 23, Apr. 2024, doi: 10.1038/s41387-024-00280-8.
[144] W.-H. J. Ho *et al.*, 'Fertility protection during chemotherapy treatment by boosting the NAD(P)+ metabolome', *EMBO Mol. Med.*, vol. 16, no. 10, pp. 2583–2618, Oct. 2024, doi: 10.1038/s44321-024-00119-w.
[145] K. C. Kim, D. Kim, S. C. Kim, E. Jung, D. Park, and J. W. Hyun, 'Empetrum nigrum var. japonicum Extract Suppresses Ultraviolet B-Induced Cell Damage via Absorption of Radiation and Inhibition of Oxidative Stress', *Evid.-Based Complement. Altern. Med. ECAM*, vol. 2013, p. 983609, 2013, doi: 10.1155/2013/983609.
[146] A. H. Harrath *et al.*, 'Autophagy and Female Fertility: Mechanisms, Clinical Implications, and Emerging Therapies', *Cells*, vol. 13, no. 16, p. 1354, Aug. 2024, doi: 10.3390/cells13161354.
[147] M. Wu *et al.*, 'Biomaterials and advanced technologies for the evaluation and treatment of ovarian aging', *J. Nanobiotechnology*, vol. 20, no. 1, p. 374, Aug. 2022, doi: 10.1186/s12951-022-01566-8.
[148] M. Banasik, T. Stedeford, R. P. Strosznajder, M. Takehashi, S. Tanaka, and K. Ueda, 'Inhibition of poly(ADP-ribose) polymerase-1 attenuates the toxicity of carbon tetrachloride', *J. Enzyme Inhib. Med. Chem.*, vol. 26, no. 6, pp. 883–889, Dec. 2011, doi: 10.3109/14756366.2011.557315.
[149] A. Maniaci *et al.*, 'Hearing Loss and Oxidative Stress: A Comprehensive Review', *Antioxid. Basel Switz.*, vol. 13, no. 7, p. 842, Jul. 2024, doi: 10.3390/antiox13070842.
[150] Z. Cao, Q. Zhou, J. An, X. Guo, X. Jia, and Y. Qiu, 'Glycolytic Dysfunction in Granulosa Cells and Its Contribution to Metabolic Dysfunction in Polycystic Ovary Syndrome', *Drug Des. Devel. Ther.*, vol. 19, pp. 5255–5270, 2025, doi: 10.2147/DDDT.S525651.
[151] T. Fang, J. Yang, L. Liu, H. Xiao, and X. Wei, 'Nicotinamide mononucleotide ameliorates senescence in alveolar epithelial cells', *MedComm*, vol. 2, no. 2, pp. 279–287, Jun. 2021, doi: 10.1002/mco2.62.
[152] S. Ramesh *et al.*, 'SIRT3 activator Honokiol attenuates β-Amyloid by modulating amyloidogenic pathway', *PloS One*, vol. 13, no. 1, p. e0190350, 2018, doi: 10.1371/journal.pone.0190350.
[153] O. Oktem and K. Oktay, 'A novel ovarian xenografting model to characterize the impact of chemotherapy agents on human primordial follicle reserve', *Cancer Res.*, vol. 67, no. 21, pp. 10159–10162, Nov. 2007, doi: 10.1158/0008-5472.CAN-07-2042.
[154] A. L. Winship, J. M. Stringer, S. H. Liew, and K. J. Hutt, 'The importance of DNA repair for maintaining oocyte quality in response to anti-cancer treatments, environmental toxins and maternal ageing', *Hum. Reprod. Update*, vol. 24, no. 2, pp. 119–134, Mar. 2018, doi: 10.1093/humupd/dmy002.
[155] M. Ahmed, U. Riaz, H. Lv, and L. Yang, 'A Molecular Perspective and Role of NAD+ in Ovarian Aging', *Int. J. Mol. Sci.*, vol. 25, no. 9, p. 4680, Apr. 2024, doi: 10.3390/ijms25094680.
[156] S. J. Kierans and C. T. Taylor, 'Regulation of glycolysis by the hypoxia-inducible factor (HIF): implications for cellular physiology', *J. Physiol.*, vol. 599, no. 1, pp. 23–37, Jan. 2021, doi: 10.1113/JP280572.

[157] L. Li, X. Zhou, W. Liu, Z. Chen, X. Xiao, and G. Deng, ‘Supplementation with NAD+ and its precursors: A rescue of female reproductive diseases’, *Biochem. Biophys. Rep.*, vol. 38, p. 101715, Jul. 2024, doi: 10.1016/j.bbrep.2024.101715.
[158] J. Liang, F. Huang, Z. Song, R. Tang, P. Zhang, and R. Chen, ‘Impact of NAD+ metabolism on ovarian aging’, *Immun. Ageing A*, vol. 20, no. 1, p. 70, Dec. 2023, doi: 10.1186/s12979-023-00398-w.
[159] Y. Wang *et al.*, ‘β-Nicotinamide Mononucleotide Alleviates Hydrogen Peroxide-Induced Cell Cycle Arrest and Death in Ovarian Granulosa Cells’, *Int. J. Mol. Sci.*, vol. 24, no. 21, p. 15666, Oct. 2023, doi: 10.3390/ijms242115666.
[160] Y. Song *et al.*, ‘Oocyte transcriptomes and follicular fluid proteomics of ovine atretic follicles reveal the underlying mechanisms of oocyte degeneration’, *BMC Genomics*, vol. 26, no. 1, p. 97, Feb. 2025, doi: 10.1186/s12864-025-11291-9.
[161] K. Liu *et al.*, ‘Nampt/SIRT2/LDHA pathway-mediated lactate production regulates follicular dysplasia in polycystic ovary syndrome’, *Free Radic. Biol. Med.*, vol. 225, pp. 776–793, Nov. 2024, doi: 10.1016/j.freeradbiomed.2024.10.312.
[162] X. Xu, Y. Pang, and X. Fan, ‘Mitochondria in oxidative stress, inflammation and aging: from mechanisms to therapeutic advances’, *Signal Transduct. Target. Ther.*, vol. 10, no. 1, p. 190, Jun. 2025, doi: 10.1038/s41392-025-02253-4.
[163] J. Song *et al.*, ‘Effects of reactive oxygen species and mitochondrial dysfunction on reproductive aging’, *Front. Cell Dev. Biol.*, vol. 12, p. 1347286, 2024, doi: 10.3389/fcell.2024.1347286.
[164] T. Wang *et al.*, ‘From mitochondrial dysregulation to ferroptosis: Exploring new strategies and challenges in radioimmunotherapy (Review)’, *Int. J. Oncol.*, vol. 67, no. 3, p. 76, Sep. 2025, doi: 10.3892/ijo.2025.5781.
[165] D. Wu, C. Liu, and L. Ding, ‘Follicular metabolic dysfunction, oocyte aneuploidy and ovarian aging: a review’, *J. Ovarian Res.*, vol. 18, no. 1, p. 53, Mar. 2025, doi: 10.1186/s13048-025-01633-2.
[166] P. Yu *et al.*, ‘Enhanced prevention on postoperative atrial fibrillation by using anti-inflammatory biodegradable drug patch’, *Regen. Biomater.*, vol. 12, p. rbaf040, 2025, doi: 10.1093/rb/rbaf040.
[167] Y. Cai *et al.*, ‘β-Nicotinamide Mononucleotide Reduces Oxidative Stress and Improves Steroidogenesis in Granulosa Cells Associated with Sheep Prolificacy via Activating AMPK Pathway’, *Antioxid. Basel Switz.*, vol. 14, no. 1, p. 34, Dec. 2024, doi: 10.3390/antiox14010034.
[168] Y. Fan *et al.*, ‘Reverse Effects of Nicotinamide Mononucleotide Supplementation on Declining Quality of Oocytes With Polycystic Ovary Syndrome’, *FASEB J. Off. Publ. Fed. Am. Soc. Exp. Biol.*, vol. 39, no. 14, p. e70846, Jul. 2025, doi: 10.1096/fj.202500921R.
[169] H. Liang *et al.*, ‘Establishment of a mouse model of ovarian oxidative stress induced by hydrogen peroxide’, *Front. Vet. Sci.*, vol. 11, p. 1484388, 2024, doi: 10.3389/fvets.2024.1484388.
[170] X. Xu, Y. Pang, and X. Fan, ‘Mitochondria in oxidative stress, inflammation and aging: from mechanisms to therapeutic advances’, *Signal Transduct. Target. Ther.*, vol. 10, no. 1, p. 190, Jun. 2025, doi: 10.1038/s41392-025-02253-4.
[171] E. I. Azzam, J.-P. Jay-Gerin, and D. Pain, ‘Ionizing radiation-induced metabolic oxidative stress and prolonged cell injury’, *Cancer Lett.*, vol. 327, no. 1–2, pp. 48–60, Dec. 2012, doi: 10.1016/j.canlet.2011.12.012.
[172] D. R. Green and J. C. Reed, ‘Mitochondria and apoptosis’, *Science*, vol. 281, no. 5381, pp. 1309–1312, Aug. 1998, doi: 10.1126/science.281.5381.1309.
[173] H. J. Leese, R. G. Sturmey, C. G. Baumann, and T. G. McEvoy, ‘Embryo viability and metabolism: obeying the quiet rules’, *Hum. Reprod. Oxf. Engl.*, vol. 22, no. 12, pp. 3047–3050, Dec. 2007, doi: 10.1093/humrep/dem253.
[174] H. J. Leese, R. G. Sturmey, C. G. Baumann, and T. G. McEvoy, ‘Embryo viability and metabolism: obeying the quiet rules’, *Hum. Reprod. Oxf. Engl.*, vol. 22, no. 12, pp. 3047–3050, Dec. 2007, doi: 10.1093/humrep/dem253.

[175] S. Someya *et al.*, ‘Sirt3 mediates reduction of oxidative damage and prevention of age-related hearing loss under caloric restriction’, *Cell*, vol. 143, no. 5, pp. 802–812, Nov. 2010, doi: 10.1016/j.cell.2010.10.002.
[176] X. Deng *et al.*, ‘Nicotinamide mononucleotide (NMN) protects bEnd.3 cells against H2 O2 -induced damage via NAMPT and the NF-κB p65 signalling pathway’, *FEBS Open Bio*, vol. 11, no. 3, pp. 866–879, Mar. 2021, doi: 10.1002/2211-5463.13067.
[177] Y. He *et al.*, ‘Targeting PI3K/Akt signal transduction for cancer therapy’, *Signal Transduct. Target. Ther.*, vol. 6, no. 1, p. 425, Dec. 2021, doi: 10.1038/s41392-021-00828-5.
[178] K. Wu *et al.*, ‘Nicotinamide mononucleotide attenuates HIF-1α activation and fibrosis in hypoxic adipose tissue via NAD+/SIRT1 axis’, *Front. Endocrinol.*, vol. 14, p. 1099134, 2023, doi: 10.3389/fendo.2023.1099134.
[179] J. Chen, C. Lin, X. Huang, and W. Bian, ‘Baicalin enhances proliferation and reduces inflammatory-oxidative stress effect in H2O2-induced granulosa cells apoptosis via USP48 protein regulation’, *BMC Complement. Med. Ther.*, vol. 24, no. 1, p. 42, Jan. 2024, doi: 10.1186/s12906-024-04346-z.
[180] F. Fontana, G. Giannitti, S. Marchesi, and P. Limonta, ‘The PI3K/Akt Pathway and Glucose Metabolism: A Dangerous Liaison in Cancer’, *Int. J. Biol. Sci.*, vol. 20, no. 8, pp. 3113–3125, 2024, doi: 10.7150/ijbs.89942.
[181] K. M. Holmström and T. Finkel, ‘Cellular mechanisms and physiological consequences of redox-dependent signalling’, *Nat. Rev. Mol. Cell Biol.*, vol. 15, no. 6, pp. 411–421, Jun. 2014, doi: 10.1038/nrm3801.
[182] J. Lin, C. Handschin, and B. M. Spiegelman, ‘Metabolic control through the PGC-1 family of transcription coactivators’, *Cell Metab.*, vol. 1, no. 6, pp. 361–370, Jun. 2005, doi: 10.1016/j.cmet.2005.05.004.
[183] L. Yang *et al.*, ‘The Role of Oxidative Stress and Natural Antioxidants in Ovarian Aging’, *Front. Pharmacol.*, vol. 11, p. 617843, 2020, doi: 10.3389/fphar.2020.617843.
[184] L. Rajman, K. Chwalek, and D. A. Sinclair, ‘Therapeutic Potential of NAD-Boosting Molecules: The In Vivo Evidence’, *Cell Metab.*, vol. 27, no. 3, pp. 529–547, Mar. 2018, doi: 10.1016/j.cmet.2018.02.011.

Publications

1. Zhang W, Zhang J, Xue H, Chen X, Li M, Chen S, Li Z, Sechi LA, **Wang Q**, Capobianco G, Lei X. Nicotinamide Mononucleotide Improves Endometrial Homeostasis in a Rat Model of Polycystic Ovary Syndrome by Decreasing Insulin Resistance and Regulating the Glylytic Pathway. Mol Nutr Food Res. 2024 Nov;68(21):e2400340. doi: 10.1002/mnfr.202400340. Epub 2024 Oct 17. PMID: 39420767.
2. Hou L, Liang X, Zeng L, **Wang Q**, Chen Z. Conventional and modern markers of pregnancy of unknown location: Update and narrative review. Int J Gynaecol Obstet. 2024 Dec;167(3):957-967. doi: 10.1002/ijgo.15807. Epub 2024 Jul 18. PMID: 39022869.
3. Hu R, Long S, Luo M, Tang B, Tan T, Dong W, **Wang Q**, Zhang J. Hyperglycemia Inhibits Hepatic SHBG Synthesis Through the NGBR-AMPK-HNF4 Pathway in Rats with Polycystic Ovary Syndrome Induced by Letrozole in Combination with a High-Fat Diet. Mol Nutr Food Res. 2024 Jul;68(14):e2300915. doi: 10.1002/mnfr.202300915. Epub 2024 Jun 11. PMID: 38862276.
4. Li T, Liu J, Liu K, **Wang Q**, Cao J, Xiao P, Yang W, Li X, Li J, Li M, Tang X, Li M, Zhang S, Lei X. Alpha-ketoglutarate ameliorates induced premature ovarian insufficiency in rats by inhibiting apoptosis and upregulating glycolysis. Reprod Biomed Online. 2023 Apr;46(4):673-685. doi: 10.1016/j.rbmo.2023.01.005. Epub 2023 Jan 26. PMID: 36894359.
5. Hu Y, Li G, Ma Y, Luo G, **Wang Q**, Zhang S. Effect of Exosomal lncRNA MALAT1/miR-370-3p/STAT3 Positive Feedback Loop on PI3K/Akt Pathway Mediating Cisplatin Resistance in Cervical Cancer Cells. J Oncol. 2023 Feb 6;2023:6341011. doi: 10.1155/2023/6341011. PMID: 36793374; PMCID: PMC9925267.
6. Liang A, Zhang W, **Wang Q**, Huang L, Zhang J, Ma D, Liu K, Li S, Chen X, Li S, Lei X. Resveratrol regulates insulin resistance to improve the glycolytic pathway by activating SIRT2 in PCOS granulosa cells. Front Nutr. 2023 Jan 18;9:1019562. doi: 10.3389/fnut.2022.1019562. PMID: 36742000; PMCID: PMC9889872.

Acknowledgements

I would like to say ‘Grazie mille’ to my dear supervisors: Prof.Giampiero Capobianco, Prof.ssa Marilena Formato, and Prof.Antonio Cigliano, for their invaluable guidance, encouragement, and patience during my PhD journey. Their continuous support and insightful mentorship have been fundamental to both my academic development and personal growth. I feel truly fortunate to have had such inspiring mentors during my doctoral studies.

I am also sincerely grateful to Prof.ssa Sanna and Prof. Sechi, who served as my PhD coordinators in Italy, for their constant assistance and constructive advice.

My appreciation further extends to all collaborators and participants in the project, whose cooperation and contributions have greatly enriched this research.

Finally, I owe my great thanks to my family and colleagues for their unwavering support, encouragement, and understanding, which sustained me both academically and personally throughout the course of my PhD.